GaN- and VO_2-Based Nanostructures: Physics and Photonic Applications

Dissertation

zur Erlangung des Doktorgrades der Naturwissenschaften
der Fakultät Physik der Technischen Universität Dortmund

vorgelegt von

Thorben Jostmeier

2016

Erster Gutachter: Prof. Dr. Markus Betz (Technische Universität Dortmund)
Zweiter Gutachter: Prof. Dr. Hubert J. Krenner (Universität Augsburg)

Datum der Einreichung: 20. September 2016
Datum der Disputation: 16. November 2016

Contents

Chapter 1

Introduction and Overview of the Thesis

The United Nations Educational, Scientific and Cultural Organisation (UNESCO) proclaimed 2015 to be "The International Year of Light and Light-Based Technologies" in order to "highlight to the citizens of the world the importance of light and optical technologies in their lives, for their futures and for the development of society" [1].

Light-emitting devices and their capabilities experienced a radical change in the course of the last five decades. The invention of the laser (light amplification by stimulated emission of radiation) and LEDs (light emitting diodes), beginning in the early 1960s, has triggered a technological revolution that impacts modern society equally strong as the rise of electronics in the twentieth century [2; 3]. Light emitted by lasers offers high intensity, spectral brilliance and long coherence. It enables novel applications and it can be manipulated in ways that are not possible for incoherent light emitted by classical light sources. These light sources, such as bulbs or halogen lamps, undergo a similarly fundamental change. Semiconducor-based LEDs are rapidly developing into the most important source of illumination. Different forms of light are nowadays utilized in a multitude of personal, technological and industrial applications [2; 3]:

In industrial settings, such as manufacturing and production, lasers are used to cut, weld and melt. Furthermore, they are employed for alignment, metrology and analysis. Semiconductor microchips are fabricated using ultra violet radiation during the photolithography. In medicine and biotechnology, lasers and optics are applied in many ways ranging from surgeries, to diagnostics and bio-sensing. The storage and readout of data in optical discs (CD, DVD, Blu-ray) using low-cost diode lasers is part of the everyday life. LEDs are used for small- and large-scale illumination indoors, outdoors, in cars, and LED-based displays set the standard in most modern (mobile) computing and entertainment technologies. The utilization of near infrared light for the transfer of information in optical fibers is crucial for the highspeed transmission of information on a global scale, as pointed out below.

The methods and physical phenomena that lay the foundation for all the above-mentioned technologies are summarized as 'photonics' [3]. This term reflects the fact that photons are the smallest unit of light, in the fashion of electrons in electric currents. Photonics comprises the physics and applications of interactions between light and matter, which includes industrial and commercial applications, sophisticated quantum physics as well as classical ray optics.

Photonics is gaining attention and importance in fundamental research and industrial applications alike. In 2014, the Nobel prices in physics and chemistry were awarded to groundbreaking, application-driven research on photonic topics [4; 5]. The photonic industry in Germany is growing steadily and reached a production volume worth €30 billion in 2015, and the worldwide production is expected to be worth €615 billion by the year 2020 [6].

The subjects of the examinations carried out in thesis are mainly connected to an area of photonic research that aims to create components for the generation, modulation or sensing of (electro-)optical signals. These 'photonic elements' are structures or devices that alter the propagation of light in, e.g., intensity, direction of propagation, spectral composition or phase. Optoelectronic devices like light sources, lasers, detectors, sensors or photodiodes are also assigned to this category.

Photonics is furthermore envisioned to revolutionize the processing and transport of information in the future. The on-chip processing of data is present in every aspect of modern life, such as personal computers, mobile communication devices, multimedia electronics, large mainframe computer clusters, cars, public transport systems, home appliances and many more. State-of-the-art microprocessors utilize the charge of electrons as the carrier of digital information. While the speed of devices is still increasing, the eventual breakdown of the famous Moore's law [7] seems to be inevitable [8; 9], considering the size of transistors is already in the 10 nm regime and scheduled to shrink further [10]. Since more than a decade, the computer industry has begun to account for this issue by introducing parallel processing and multi-core technologies. New ways of processing and transferring digital information on-chip and chip-to-chip are needed in the long run [8; 11].

Closely connected to the rising capabilities and shrinking structures of processing units, the demands for speed and downscaling of pathways that transfer data between microprocessors over distances of $\geq$ mm are growing. The bottleneck for the speed of modern computing actually are the chip-to-chip and board-to-board connections, called interconnects. Copper-based solutions suffer from heat dissipation, cross-talk between channels and a limited ability for parallelization of channels due to size restrictions [8; 12; 13] .

To overcome the 'interconnect bottleneck', the optical transfer of data is envisioned to replace the established all-electrical solutions [11; 12]. In this context, using light as the carrier of information has many intrinsic benefits: weak light-light interaction, speed-of-light transfer velocity, low power losses and the simultaneous, parallel transfer of multiple signals.

Optical fibers have been used since the 1980s for transferring digital information over global distances and with superior speed compared to electronics [14; 15]. Lately, space-division wavelength multiplexing has enabled data transfer rates of 10^{15} bits per second

(1000 Tbit/s). Optical fiber network cables operate at smaller length scales, for example within computing clusters or to provide high bandwidth internet connection within cities. The range of wavelengths at which optical fibers operate is called the 'telecom wavelengths'. They span from 800 nm to 1650 nm, with the most widely used band located around 1550 nm [14]. In order to use optical interconnects between modern processing units, the modulation of optical signals and the conversion between electrical and optical signals at high speeds are crucial prerequisites [11].

Overview of the Thesis

The fundamental research presented in this thesis studies potential materials and concepts for the utilization as photonic elements operating in the telecom wavelength regime. It is analyzed how the characteristics of the structures and the implementation of the proposed concepts could be applied in photonic research or devices. Even though the physical background of the structures utilized in this thesis are distinctly different, they have common aspects. For one, the light-matter interaction is determined by effects that stem from the nanoscale dimensions of the structures. In addition, the decisive optical or electronic properties can be tailored during the fabrication of the structures to suit the intended applications at telecom wavelengths.

The first part of this thesis is devoted to the investigation of GaN/AlN superlattices. These structures belong to the group of semiconductor heterostructures, i.e. planar layered nanoscale sheets of different semiconductors. As will be discussed in Chapter 2, the quantum confinement of electrons within the layers results in the emergence of additional energy levels [16], which can be designed for fundamental light-matter interactions at telecom wavelengths. The Chapters 3 and 4 characterize the GaN/AlN superlattice in terms of its linear and ultrafast nonlinear optical properties [17].

In the second part of this thesis, vanadium dioxide nanocrystals (VO_2-NCs) and their potential applications for photonic elements are studied. VO_2 is a phase change material, which features a most appealing property, namely the transition from an insulating to a metallic solid state phase [18]. During this phase transition, the optical properties of VO_2 change markedly, such that the light-matter interaction is strongly altered [19]. Phase change materials offer great prospect for utilization in advanced photonic applications [20]. VO_2 is an especially suited as a candidate, since its phase transition happens near ambient temperatures. The nanocrystals (NCs) of VO_2 studied in this thesis are specifically designed for the telecom wavelength regime. Chapter 6 introduces this material, the unique properties of the nanocomposite used in this thesis and shows how they may be tailored.

Chapter 7 demonstrates the creation of reconfigurable photonic elements for telecom wavelengths based on VO_2-NCs [21]. This nanocomposite allows for the optical preparation of a long-term stable, persistent metallic phase in spatial sub-ensembles of NCs. The different optical properties of the insulating and metallic phase of VO_2 are utilized to generate photonic functionalities in otherwise unstructured samples. Diffraction-based fundamental photonic elements are inscripted into VO_2 nanocomposites and can be readily erased in a non-destructive fashion.

The VO_2-related investigations moreover address the utilization of VO_2-NCs in a field of research called plasmonics, which has emerged as a major subcategory of nanophotonics over the last decade [22; 23]. Plasmonic research treats the interactions of light with electrons in nanoscale metallic structures. All-optical designs suffer from an intrinsic limitation to the size and scalability, namely the optical diffraction limit [24]. Plasmonic excitations at metal surfaces, surface plasmon polaritons (SPPs), are able to confine light to dimensions far below this limit. They enable the coupling of electronic and optical signals and offer ways to guide information along metal-dielectric interfaces. An extensive introduction to plasmonics and the physics of surface plasmon polaritons is given in Chapter 8.

The fast and deterministic modulation of the conversion between light and SPPs is key to use plasmonics for data processing and interconnects. In the Chapters 9 and 10, the ability of VO_2 to change the properties of light is combined with two proposed designs of plasmonic couplers. Novel routes for the creation of active plasmonic elements are demonstrated, based on the grating-assisted light-SPP coupling and the Kretschmann configuration. The concepts utilize the phase transition in VO_2-NCs to offer new ways of modulating the light-SPP coupling in nanostructures composed of dielectrics, VO_2 and metals [25].

Part I

Ultrafast Carrier Dynamics and Resonant Inter-Miniband Nonlinearity in Cubic GaN/AlN Superlattices

Chapter 2

Introduction to Cubic GaN/AlN Heterostructures

Semiconductors are one of the most important classes of materials for the everyday technology used in modern society. Computers, mobile phones, and the transistors on microchips in general are based on silicon and its oxides. Semiconductors also play a key role in optoelectronic applications for the back-and-forth conversion of light and electricity. The group III-V nitride compounds AlN,GaN and InN (and their alloys) dominate applications such as detectors for the ultraviolet (UV) spectrum, high-efficiency solar cells and LEDs emitting blue and UV light. For example, GaN-based laser diodes emitting at 405 nm are used to read out Blu-ray discs. The spectral range in which these devices operate is determined by the band gap of the semiconductor. In a simplified picture, the interaction of photons with a two-level system made up of states in the valence and conduction bands is utilized: photodiodes use the electrical current created by the absorption of photons, LEDs emit light due to spontaneous emission, and in semiconductor lasers, the stimulated emission is the basis for the generation of coherent light beams. An outstanding example of the impact of group III-V nitrides are "Efficient blue light-emitting diodes leading to bright and energy-saving white light sources" [5], that were awarded the Nobel prize in physics in 2014.

The principles of quantum mechanics give rise to novel phenomena if the size of a material approaches the nanoscale in one or more dimensions. In this thesis, planar heterostructures made of nanometer thin layers of cubic GaN and AlN are investigated. More specifically, the potential landscape that is formed by the heterojunction AlN/GaN/AlN confines electrons in the spatial dimension given by the growth direction of the layers. This type of structure is called quantum well (QW). The resulting energy levels become quantized and electronic subbands emerge, which serve as a multi-level system for electronic and optical interactions [26].

Most importantly, many properties of the inter-subband (ISB) transitions, such as central energy and width, can be tailored during the fabrication process, with central wavelengths spanning $\sim 1\,\mu\text{m}$ to several tens of μm [27]. Because of this tunability, the spectral range which devices could cover is larger compared to inter-band transitions. Owing to the huge conduction band offsets between the different III-V nitrides, the ISB energies in thin QWs based on these materials can be tuned to the telecom wavelength window [27; 28].

Another appealing feature of these structures is the ultrafast electron relaxation between the subbands, which opens up a route towards devices operating at a speed of several GHz to THz [27; 28]. Different kinds of photonic applications based on the light-matter interaction in such nitride-based ISB systems have been demonstrated, comprising quantum cascade lasers [29; 30], photo detectors [27; 31] or optical modulators [27]. Reviews including basic physics, material parameters and applications can be found in Refs. [27; 32; 33].

There is ongoing effort to utilize ISB transitions in nitride-based heterostructures for photonic and electro-optic devices. Consequently, a number of studies have elucidated the dynamical optical response of such structures, which determines the speed or efficiency of potential devices [34–38]. So far, these experiments have focused on the hexagonal phase, which is widely used for nitride-based devices. However, it is characterized by the presence of strong piezoelectric polarization. The resulting internal electric fields complicate the designs of heterostructures and lower their efficiency as they, e.g., separate electrons and holes. Much less effort has been devoted to zincblende GaN and AlN. While this cubic phase is more challenging to grow, the detrimental piezoelectric fields are intrinsically removed.

Recently, ISB transitions in the near-infrared regime have been achieved in thin n-doped GaN/AlN multi-QWs [39–41]. The samples examined in this thesis extend these studies and aim for broad transitions covering the telecom wavelength regime. They are composed of 80 quantum well layers forming a cubic GaN/AlN superlattice. The electronic subbands in these structures are energetically broadened and called minibands. What is new about these structures are the ultranarrow AlN barriers of only 1 nm thickness. They are expected to increase the coupling between adjacent wells and broaden the inter-miniband transition, see Section 3.2. Many applications, e.g. photodetectors, would benefit from a broad transition, since they could cover a large spectral regime in one device.

Two major tasks are addressed in the two ensuing chapters:

First, the inter-miniband (IMB) transition is characterized with respect to its strength as well as central energy and width in Chapter 3. Basic material properties and the physics of the minibands in superlattices are discussed as a basis for understanding the experimental methods and results.

Second, the electron dynamics and the nonlinear optical response of the IMB transition are investigated in Chapter 4. More specifically, IMB electron relaxation times are measured using resonant pump-probe spectroscopy. The third-order nonlinearity associated with this transition is then extracted from the data. Studies of the ultrafast dynamics or the nonlinear optical properties of cubic GaN/AlN heterostructures have not been reported so far. Since the speed and efficiency of potential devices is determined by these quantities, there is a need to close this gap, which is done in this thesis.

Chapter 3

Fundamentals and Linear Optical Characterization

The goal of GaN/AlN superlattice structures investigated in this thesis is to create an engineered two-level system based on electronic subbands with transition energies in the telecom wavelength regime. Many properties of the transition such as central energy and width can be tailored during the fabrication process, which is addressed in the following section. In Section 3.2, the fundamental physics of carriers in quantum wells and superlattices is discussed. Furthermore, simulations of the energy levels in the cubic GaN/AlN superlattice are compared to results of photoluminescence measurements. The central results of this chapter are presented in Section 3.3, where the inter-miniband (IMB) absorption in the cubic GaN/AlN superlattice is analyzed.

Parts of the results of this chapter have already been published in Ref. [17]. The simulations and photoluminescense measurements, presented at the end of Section 3.2, were performed by Tobias Wecker from the University of Paderborn.

3.1 Material Properties and Layer Sequence of the Cubic GaN/AlN Superlattice

The constituents of the investigated superlattice are the group III-V nitrides GaN and AlN in the cubic phase, referred to as c-GaN and c-AlN below. Both are direct semiconductors with rather large Γ-point band gap energies, corresponding to wavelength in the UV regime (see Table 3.1). The samples were grown by Tobias Wecker from the group of Prof. Dr. Donat As at the University of Paderborn using plasma-assisted molecular beam epitaxy (MBE). During this process, crystalline layers are grown on suitable substrates using gas phase deposition of evaporated source elements. The crystal structure of the deposited layer adapts to the substrate, whereby the lattice structure and orientation can be controlled. The fabrication of heterostructures composed of c-GaN and c-AlN is achieved by using cubic SiC as a substrate layer. This substrate is chosen because its lattice constant is close

Table 3.1: Parameters of cubic GaN and AlN at 300 K. The lattice constant of the 3C-SiC substrate is 4.3596 Å. The data is taken from Ref. [45] and references therein. The quantity m_0 is the electron rest mass.

	c-GaN	c-AlN
lattice constant (Å)	4.503	4.373
band gap at Γ-point (eV)	3.23	5.93
effective electron mass (m_0)	0.19	0.3
effective light hole mass (m_0)	0.28	0.44
effective heavy hole mass (m_0)	0.83	1.32

to c-GaN and c-AlN (see Table 3.1). More details about the fabrication process can be found in Refs. [42–45].

As opposed to the stable hexagonal structure, the nitrides crystallize in a metastable cubic zincblende lattice structure. GaN and AlN in the hexagonal phase are characterized by the presence of spontaneous and piezo-electric polarizations along the c-axis. If heterostructures are grown from these materials, internal electric fields are generated along the growth directions [46; 47]. Such internal electric fields complicate the prediction of the electronic levels, thus they are detrimental for the design of such structures. Furthermore, the efficiency of potential devices is reduced due to carrier localization in triangular potentials and the resulting separations of electron and hole wave functions. These detrimental effects are avoided in heterostructures composed of cubic GaN and AlN, which are intrinsically devoid of internal polarization fields along the growth direction. This property is beneficial for the design and efficiency of electro-optic devices based on cubic GaN/AlN heterostructures. Some important structural and electronic parameters of c-GaN and c-AlN are summarized in Table 3.1.

The layer structure of the samples used for the examinations carried out within thesis is depicted in Fig. 3.1(a). A 10.4 µm thick epilayer of 3C-SiC (001), grown on a 548 µm thick layer of Si, serves as substrate for the epitaxial growth of cubic GaN/AlN heterostructures. First, a 100 nm thick c-GaN buffer layer is grown, followed by the superlattice. It consists of 80 periods of nominally 1 nm thick c-AlN barriers and nominally 1.8 nm thick n-doped c-GaN QWs. The doping is done by incorporating Si with a concentration of $\sim 10^{19}\text{cm}^{-3}$ as a n-type dopant in the c-GaN layers. Finally, a capping layer of 1 nm c-AlN is deposited on top.

For understanding some of the results presented in this part of the thesis, it is instructive to comment on the structural quality of the layer sequence. Atomic force micrographs of the sample surface reveal a roughness of ≈ 6 nm (rms) in a 10 µm × 10 µm sample area (measurement performed by Tobias Wecker). These rather large undulations arise from stacking faults in the SiC substrate which extend throughout the buffer layer and the superlattice layer sequence (see Ref. [48] for details and STEM images). Note that the layer

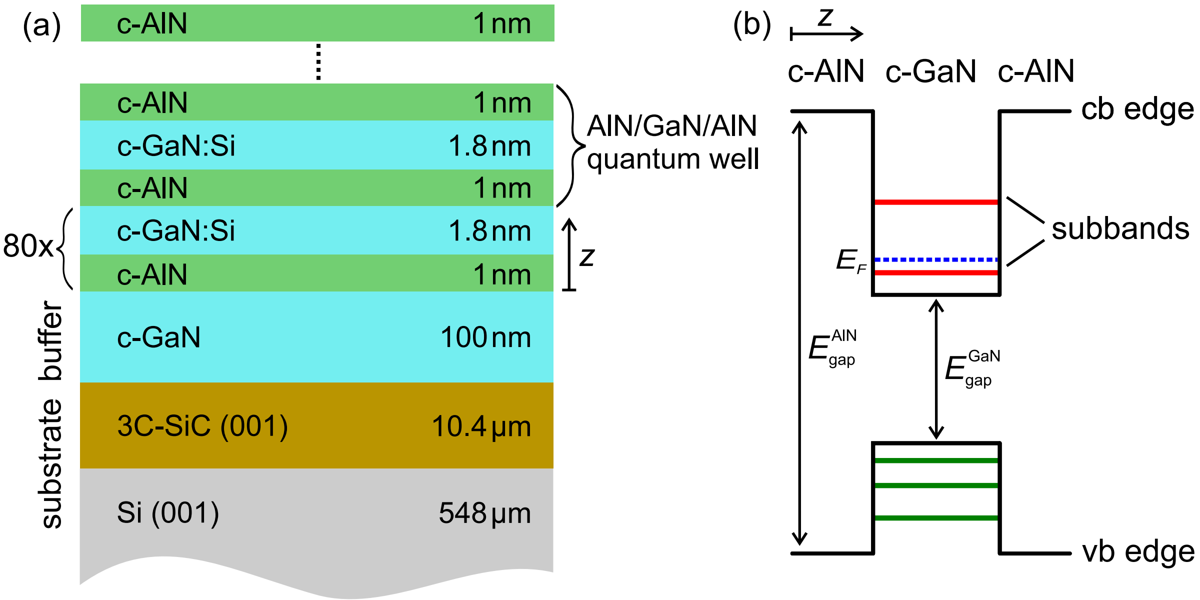

Fig. 3.1: (a) Layer sequence of th cubic GaN/AlN superlattice. (b) Sketch of the alignment of conduction (cb) and valence (vb) band in the AlN/GaN/AlN heterojunction. The potential landscape equals a quantum well, in which electronic subbands emerge due to the confinement in *z*-direction.

sequence is not interrupted in lateral dimensions, but just experiences an undulation. An important implication of the stacking faults are monolayer fluctuation of the layer thicknesses across the superlattice [48]. These variations alter the energies of the transitions and, furthermore, affect their width (see the discussion of the IMB absorption in Section 3.3).

Fig. 3.1(b) displays a sketch of the potential landscape of a single AlN/GaN/AlN QW, which is now used to give a brief outlook to the electronic properties of the superlattice heterostructure. The physical backgrounds are discussed in the next section in detail. The figure shows the relative positions of the conduction and valence band edges versus the growth coordinate z. Due to the type I band alignment, potential barriers form and carriers are trapped in the GaN layer. The confinement in z-direction leads to the quantization of energy levels and two so-called subbands emerge in the QW. Due to the strong n-type doping of the GaN layers, the Fermi level is raised above the energetically lowest subband such that it is strongly populated. Taken together, a two-level system consisting of a filled lower-energy and an empty upper-energy level emerges, which offers inter-miniband transitions in the telecom wavelength regime.

3.2 Energy Levels of the Cubic GaN/AlN Superlattice

In this section of the text, the physics of electrons in quantum wells and superlattices that lead to the formation of a two-level miniband system is discussed in detail. This topic is covered by many textbooks (for example Ref. [16], chapter 4, or Ref. [49], chapter 12). The following discussion is based on potential landscapes that represent the conduction band edges in the AlN/GaN/AlN heterojunction. However, all conclusions also apply to the valence band edges, with minor corrections. At the end of this section, simulations of the energy levels of a single quantum well are presented that allow a more precise prediction of the transition energies in the actual superlattice sample.

In the most simple picture, a quantum well is treated as an one-dimensional, infinitely high potential square well, also known as the particle-in-a-box problem. For a well of width w, the potential landscape reads $V(z) = 0$ for $0 < z < w$, and $V(z) = \infty$ elsewhere, see Fig. 3.2(a). The coordinate z is equal to the growth direction of the heterostructure. Solving the stationary Schrödinger equation $E\varphi(z) = H\varphi(z)$, one finds that the resulting wave functions correspond to localized states with discrete wave vectors in z-direction and quantized energy levels. The wavefunctions and eigenenergies of these states are given by

$$\varphi_n(z) = A\sin(k_z z) = A\sin\left(\frac{n\pi}{w}z\right) \tag{3.1}$$

$$\text{and} \quad E_n = \frac{\hbar^2 k_z^2}{2m^*} = \frac{\hbar^2}{2m^*}\frac{\pi^2}{w^2}n^2 \ . \tag{3.2}$$

Here, A is a complex normalization constant and m^* is the effective electron mass. The wave number k_z is equal to the results for a standing wave, cf. the illustration of the wave functions and eigenenergies in Fig. 3.2(a). The quantum number $n = 1, 2, 3, ...$ labels the first, seconds, third, etc. electronic subband en. From Eq. (3.2), one can already see how the transition energies between the subbands can be tailored via the width w.

The equations given above only describe the wave functions in z-direction and the corresponding eigenenergies. Since the electrons are confined in z, but free to move in the two in-plane directions x and y, the respective in-plane part of the wave function is given by a two-dimensional plane wave. The corresponding contribution to the total energy $E(\mathbf{k}) = E_n(k_z) + E(k_\perp)$ is the well-known parabolic dispersion of plane waves $E(k_\perp) = \hbar^2 k_\perp^2/2m^*$, with the in-plane wave vector $k_\perp^2 = k_x^2 + k_y^2$.

The approximation of a single quantum well with infinitely high potential barriers allows to understand the most basic properties of electrons in a two-dimensional heterostructure with type I band alignment. In the next step towards the description of the cubic GaN/AlN superlattice, a double quantum well with finite barrier height V_0 is discussed. The first thing to notice is that the electronic levels are not localized anymore if $E_n > V_0$.

As can be seen from Fig. 3.2(b), a finite potential barrier results in an exponential decay of the wave functions to areas outside of the quantum well. When the separation barrier

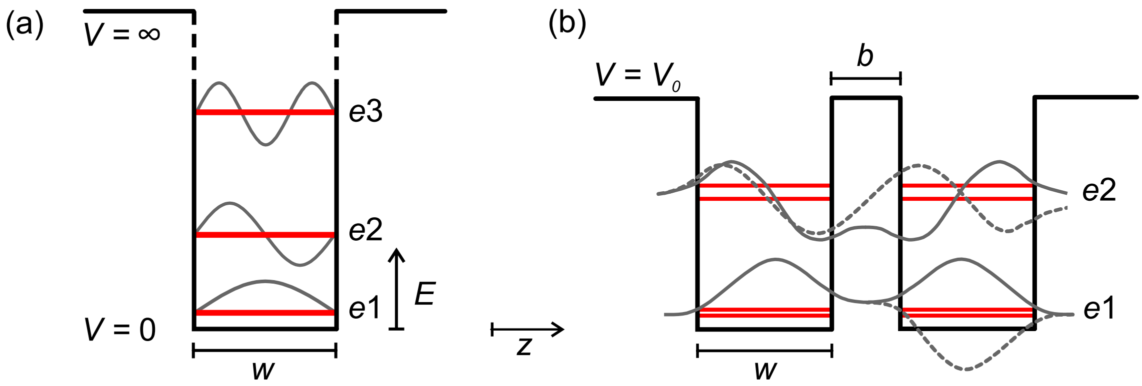

Fig. 3.2: Potential landscapes $V(z)$ of (a) a single quantum well with infinitely high potential barriers (particle-in-a-box) and (b) a double quantum well with finite barrier height. The energy levels E_n of the electronic subbands *en* are depicted by red lines. Gray lines illustrate the corresponding wave functions φ_n. (b) In the case of a double quantum well, two solutions for the wave functions exist (symmetric and antisymmetric), such that the two energy levels of each subband split.

b between two neighboring wells is sufficiently small, the wave functions are present in both quantum wells and tunnel coupling sets in such that the wavefunctions overlap. In this case, the solutions for the individual wells no longer hold and an analytical solution of the coupled system gets quite complicated. The subbands split into two energetically nondegenerate states, since two wave functions with different symmetry and eigenenergies solve this modified problem. Due to this energetic splitting, the ISB transitions cover a broader range of energies. The splitting gets larger for decreasing width of the barriers which results in stronger tunnel coupling.

When the number of coupled wells N is increased, a multi-quantum well (MQW) is formed where each subband splits in to N energy levels. The splitting between the lowest and highest level of each subband increases with N, whereby the range of possible transition energies further broadens. In the next paragraph, the formation of minibands in a structure with high N is discussed.

The focus of the discussion is now laid on a MQW structure resembling the cubic GaN/AlN superlattice. A superlattice is essentially composed of a one-dimensional array of N quantum wells, as depicted in Fig 3.3(a). The name stems from the second level of periodicity in the structure, with the first level being the lattice of the materials. Note that there is no clear distinction between MQWs and superlattices based on the number N. In the case of the superlattice studied here, $N = 80$ and $w/b \approx 2$. Because of the large number of coupled quantum wells and the supposedly strong tunnel coupling, the broadened subbands are called minibands in superlattice structures. They can be seen as continuous energy bands as opposed to 80 discrete levels, since each level is broadened due to its natural line width and, in the case of an actual heterostructure, thermal broadening and scattering processes. Because of the coupling-induced level splitting and broadening of

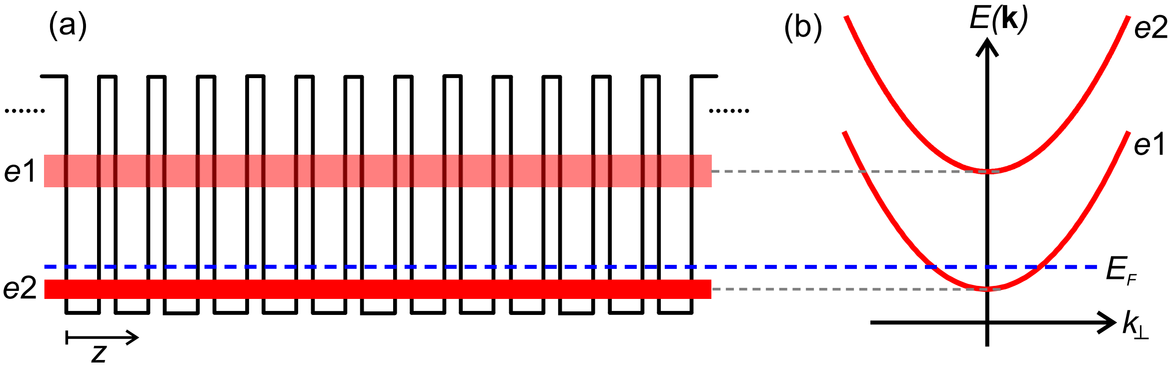

Fig. 3.3: (a) Schematic potential landscape of a superlattice heterostructure where broadened minibands are generated by strong interwell coupling. (b) Schematic plot of the k-dependence of the central energies of the electronic subbands. The offset is generated by the quantization of the energies due to the confinement in z-direction, cf. Eq. (3.2). The parabolic contribution $E(k_\perp)$ reflects the fact that electrons are free to move in-plane. The blue dashed line indicates the Fermi energy in the n-doped GaN/AlN superlattice studied in this thesis.

the minibands, the energetic width of the inter-miniband (IMB) transition is expected to be enlarged in structures with narrow barriers.

The formation of energy bands in an infinite superlattice can also be derived from the Kronig-Penney model, which treats electrons in a one-dimensional periodic square-well potential. The resulting electron wave functions $\psi(z) = u(z) \cdot \exp(ikz)$ are composed of a plane wave in growth direction z and a periodic Bloch function $u(z+w) = u(z)$ that incorporates the second-level periodicity of the superlattice. Similar to the formation of bands in crystals due to the lattice, this periodicity leads to the formation of gaps in the $E(k_z)$ diagram (see Ref. [50], pp.487ff, or Ref. [16], pp.177ff).

Due to the strong doping of the GaN regions with Si ($\sim 10^{19}\text{cm}^{-3}$), the Fermi level is lifted above the energy of the first subband $e1$, whereby it is strongly populated with electrons. The resulting situation is close to a two-level system with a populated ground state ($e1$) and an empty upper state ($e2$). Both levels resemble conduction bands of semiconductors, in the sense that they show a parabolic dispersion $E(k_\perp)$, with an offset E_n generated by the confinement in z-direction. The dispersions $E(\mathbf{k})$ of the minibands are shown in Fig. 3.3(b).

The IMB system offers the possibility to be used in photonic applications based on fundamental light-matter interactions, such as absorption, and spontaneous or simulated emission. It is evident from the underlying model of a single quantum well, that the transition energy can be tailored during fabrication of the heterostructure. In the following step, a characterization of the samples used in this thesis is presented.

Simulation of Energy Levels of the GaN/AlN Superlattice

In the final part of this section, the energy levels of the actual GaN/AlN superlattice sample studied in this thesis are discussed. The electron subbands in this structure are designed to show IMB transition energies in the telecom wavelength regime. In order to get a qualitative understanding of the experimental data, which is presented in the following, the energy levels of a single finite QW composed of cubic AlN/GaN/AlN are simulated. A successful prediction of the experimentally found transition energies would help to design the layer structure of future samples, in order to achieve a desired inter-band or IMB transition energy.

Even though the numerical calculations do not treat a superlattice structure, the energy levels of the QW indicate the central energies of the minibands. The results are compared with data of the inter-band transition of the superlattice sample to validate the congruence of simulations and the actual energy levels of the sample. In the next section, the IMB transition is analyzed experimentally and compared to the simulations.

The expression Eq. (3.2) for the energy levels in a single QW with infinitely high barriers does not hold for the heterostructure investigated here. One obvious reason for this is the finite barrier heigth. Further complications arise from the band alignment at the interface of atomically thin semiconductor layers. This effect is non-trivial because of the strain induced by lattice mismatch, which results in band bending and uncertainty in the band offsets [51]. Hence, the height of the potential well cannot be computed by simply considering the band offsets, band gaps and electron affinities of bulk c-GaN and c-AlN.

In order to get a qualitative understanding of the energy levels in the GaN/AlN superlattice sample, Tobias Wecker from the University of Paderborn performed simulations of a single cubic GaN/AlN quantum well using the commercial Schrödinger-Poisson solver nextnano^3 [52]. Most employed material parameters are given in Ref. [45] and references therein, and the deformation potential was taken from Ref. [51]. As a lookahead to some of the data presented in the following, it must be stated that the best match of the experimentally observed transition energies with the simulations is achieved if a 2.025 nm wide QW is assumed. This width equals 9 monolayers instead of 8 (total width 1.8 nm), that were nominally intended in the growth process.

The simulated energy level scheme of a single QW with 2.025 nm GaN well width and 1 nm AlN barrier width at 300 K is shown in Fig. 3.4(a). Here the conduction (cb) and valence band edges (vb) of the two congruents are shown versus the growth coordinate z. Two bound valence subbands $e1$ and $e2$ are found, which are separated by 715 meV. Thus, from the simulations, the IMB transition is expected to be centered at an energy of 715 meV. In the potential composed of the valance band edges, two bound light hole (lh) and three heavy hole (hh) sublevels are found. The energetically lowest inter-band transition from $hh1$ to $e1$ is found at $E_{\text{inter}}^{theory} = 3.591\,\text{eV}$.

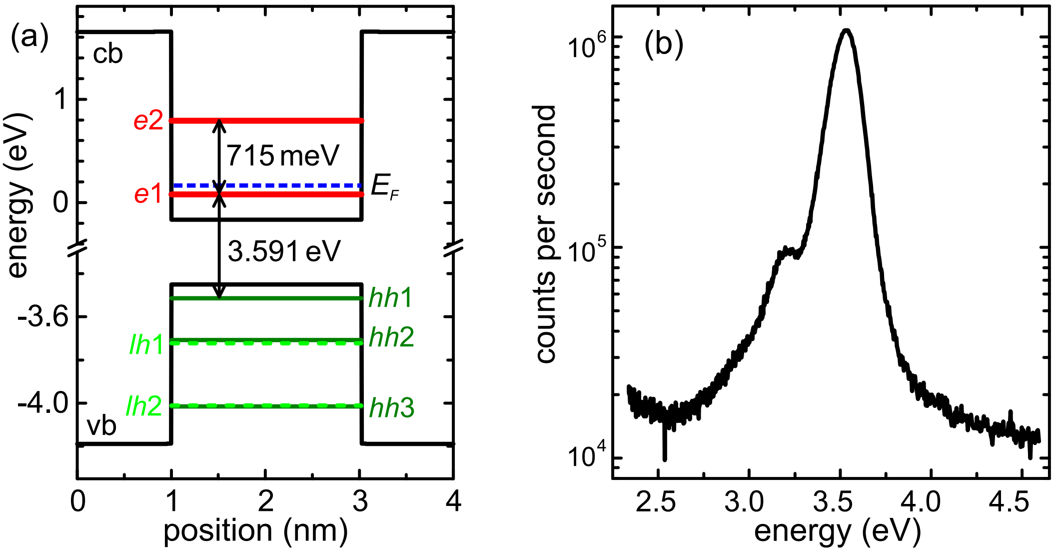

Fig. 3.4: (a) Simulation of the energy levels of a single cubic GaN/AlN QW. The energies of the inter-subband and the interband transition are visualized by vertical arrows. e: conduction sub-bands, hh: heavy hole, lh: light hole. The blue dotted line shows the Fermi level E_F. (b) Room temperature photoluminescence (PL) measurement of the GaN/AlN superlattice at 300 K showing the inter-band transition at 3.532 eV. The smaller peak at ≈ 3.2 eV is most likely caused by the PL arising from the inter-band transition in the GaN buffer layer $E_{\text{gap}} = 3.23$ eV.

In order to characterize the optical properties of the superlattice sample and validate the results of the simulation, Tobias Wecker performed photoluminescence (PL) measuremente at room temperature. Electrons are optically excited into the conduction bands by a cw (continuous wave) laser with 4.66 eV photon energy (266 nm wavelength). During the subsequent recombination of electron-hole pairs, photons are emitted and recorded with a CCD line array. The energy of the photons reveals the energy difference between the involved levels. The spectrally resolved intensity of the recorded PL is presented in Fig. 3.4(b). The maximum of the PL is observed at $E_{\text{PL}}^{\text{exp}} = 3.532$ eV, which is close the value of $E_{\text{inter}}^{\text{theory}} = 3.591$ eV. Considering the exciton binding energy, which is not accounted for in the simulations and estimated to be ~ 48 meV in a ~ 2 nm wide QW [53; 54], both values match very well.

To sum up, the central energy of the first electron and hole sub-levels of the superlattice are successfully reproduced by the simulation of a single constituent quantum well. This result points towards a successful incorporation of material parameters and strain-induced effects into the simulation, which allows to estimate the energy levels of the heterostructure prior to the fabrication. In the next section, the IMB transition is characterized and compared to the results of the simulations.

3.3 Characterization of the Inter-Miniband Absorption

A central goal of the investigation of the cubic GaN/AlN superlattice in this thesis is to analyze the inter-miniband (IMB) transition between the mini-bands $e1$ and $e2$. In the first step of the characterization, the linear optical properties of the two-level IMB system are addressed, i.e. the central energy and width of the transition is quantified. For this purpose, the transmission of a broadband near infrared light source through the superlattice is analyzed. The samples are processed into a waveguide geometry, which enhances the light-IMB interaction by generating multiple passes of the incident light through the superlattice, cf. Fig. 3.5(a). The experimental setup is described in more detail below.

The experimental procedure makes use of the polarization selectivity of the light-IMB interaction. Specifically, inter-subband absorption is driven by electric field components E_z along the growth direction of the superlattice z, which is equal to the direction of the inter-miniband dipole moment (see Ref. [16], p.316ff). The components E_x and E_y (in-plane of the layers) do not interact with the IMB transition. Mathematically, the transition matrix element $\langle\varphi_{\mathrm{e2}}|\mathbf{e}\cdot\hat{\mathbf{p}}|\varphi_{\mathrm{e1}}\rangle$ vanishes, unless the polarization vector of light $\mathbf{e}$ has a z-component. In this case, the momentum operator $e_z \cdot \hat{\mathbf{p}} = -i\hbar\partial/\partial z$ affects the z-component of the electron wave function, i.e. the bound states. In an illustrative point of view, this behavior can be understood considering that in-plane components cannot 'see' the superlattice structure and only interact with the plane wave part of the electron's wave function. The ideal situation leading to maximum light-IMB interaction, therefore, corresponds to TM (transverse magnetic) polarized light propagation parallel to the superlattice layers. In the opposite case, namely if light propagates normal to the layers, no electric field component is parallel to z. TE (transverse electric) polarized light generally results in no IMB absorption, since the electric field vector is always normal to the growth direction, in this case. See Fig. 3.5(b) for an illustration of the different configurations.

In order to maximize the light-IMB interaction, multiple total internal reflections reflections in the waveguide geometry are utilized. Light is coupled into the sample by illuminating one of the side facets of the waveguide, which are tilted by 30° with respect to the surface. Total internal reflection at the bottom Si→air interface and the top superlattice→air interface confines the light to the sample and ensures multiple passes through the superlattice layer. After the light has undergone refraction at the Si→SiC and SiC→GaN interfaces, the angle of interaction in the superlattice is $\theta \approx 43^\circ$, assuming normal incidence at the side facet. Consequently, the electric field component of TM polarized light $E_z = \sin(\theta)E$ addresses the IMB transition.

The IMB absorption is quantified by spectrally resolving the transmissions of TM and TE polarized light through the waveguide sample. Fig. 3.5 shows a sketch of the experimental method. The emission of stable tungsten light source is focused onto the side facet of the sample using a parabolic mirror of 50 mm focal length. The bottom Si substrate of

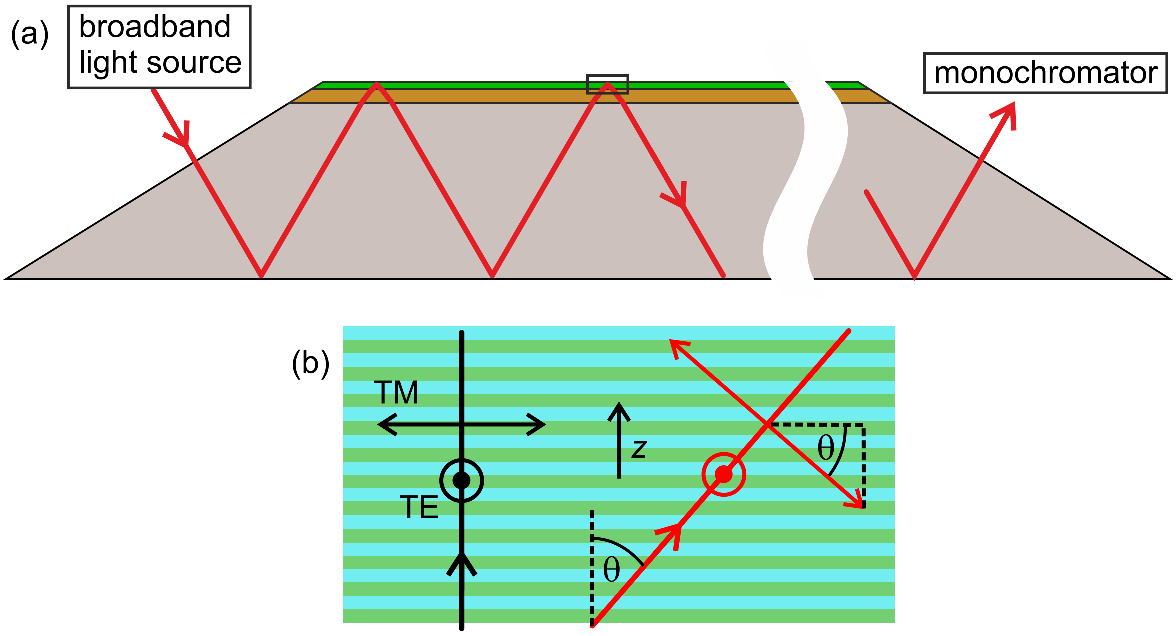

Fig. 3.5: (a) Illustration of the sample geometry of the waveguide configuration used to analyze the IMB absorption. Light originating from a broadband lightsource is confied in the sample due to total internal reflection and passes the superlattice layer $\approx$ 20 times. The absorption is spectrally resolved in a monochromator. (b) Close-up to the black box seen in (a) showing a scheme of the interaction of TM or TE polarized light with the superlattice. The electric field component $E_z||z$ parallel to the growth direction z, which is necessary for the light-IMB interaction, can only be attained using TM polarization and an interaction angle $\theta > 0$.

the waveguide is 8 mm in length. This geometry corresponds to ≈ 10 reflections at the superlattice-air interface, i.e. light passes trough the superlattice layer ≈ 20 times. The uncertainty in this number arises from the angular distribution of the incident light ($\approx \pm 10^\circ$). Light leaving the sample at the opposite side facet is collected with an optical fiber. It is then analyzed in a monochromator together with an extended-range InGaAs photodiode and lock-in detection (Stanford Research 830).

Since light-IMB interaction is expected only for TM polarization, the difference of TM and TE signals reveals the contributions of the IMB transition to the transmission. For the purpose of eliminating other effects that introduce a difference in the transmissivity of the two polarization states, such as reflection at the various surfaces, a reference sample is analyzed. It contains a 600 nm epilayer of c-GaN instead of the superlattice. All experiments are performed at room temperature.

Experimental Results for the IMB Absorption

Fig. 3.6(a) displays the results for the IMB absorption spectrum normalized to number of passes through the superlattice. The absorption per pass is calculated from the raw transmission data as the relative difference of TM and TE transmissions through the superlattice

(SL), normalized to the respective transmission through the reference sample (Ref), i.e.

$$\left(\frac{\mathrm{QW_{TE}}}{\mathrm{Ref_{TE}}}-\frac{\mathrm{QW_{TM}}}{\mathrm{Ref_{TM}}}\right)\cdot\left(\frac{\mathrm{QW_{TE}}}{\mathrm{Ref_{TE}}}\right)^{-1} \quad . \tag{3.3}$$

The accessible photon energy range is limited by the experimental detection limit at 0.5 eV and the absorption in the Si substrate for energies above 1.1 eV. Most strikingly, the results show a broad absorption centered centered at ~ 0.7 eV that corresponds to the IMB transition. The additional spectral oscillations can be attributed to Fabry-Perot interference in the 10.4 µm SiC layer. Remarkably, the width of the IMB transition, determined by extracting the FWHM of a Gaussian fit to the data, is as large as ~ 370 meV. As opposed to this, in previous studies on cubic [40; 41] or hexagonal [39; 55–58] GaN/Al(Ga)N superlattices, transition widths in the range of 100 meV-200 meV were found. The maximum reported value is 240 meV [56]. The strongly increased width in the present superlattice can be attributed to two mechanisms:

(i) The first reason is related to the fundamental physics of multi quantum wells. The ultranarrow barriers enhance the overlap of the wave functions localized in the quantum wells. In turn, tunnel coupling between adjacent wells is enhanced and, consequently, the level splitting is increased. The resulting minibands are substantially broadened.

(ii) As has been stated before, the structure exhibits fluctuations of the quantum well width by ± 1 monolayer leading to interface and surface roughness. The implications of this variation are twofold: Firstly, there is theoretical evidence that the increased scattering at interface and surface roughnesses causes broadening of the IMB transitions [59; 60]. Secondly, spatial inhomogeinities across the macroscopic waveguide may further increase the linewidth [48]. The thickness of the quantum well layer may vary by one monolayer and, accordingly, the central IMB transition energy changes. Since the employed method of measuring the IMB absorption intrinsically involves averaging the optical response of different areas of the sample, this effect would lead to an inhomogeneously broadened absorption spectrum.

Fig. 3.6(b) offers a direct comparison with the IMB absorption of cubic GaN/AlN superlattices with different quantum well and barrier thicknesses (data taken from Ref. [41]). These samples were grown with the same MBE unit at the University of Paderborn that was used for the fabrication of the samples investigated in this thesis. The FWHM of the IMB transition in the samples A,B and C are 170 meV, 180 meV and 200 meV, respectively. Special consideration should be given to the IMB absorption of sample A, since it features a similar quantum well thickness and doping concentration as the sample in panel (a). In contrast to the sample investigated here, the barriers are 3 nm wide (instead of 1 nm) and the number of quantum wells is 40 (instead of 80). The structural quality can be considered to be similar.

From the comparison of the two superlattices, it can be concluded that the narrow AlN

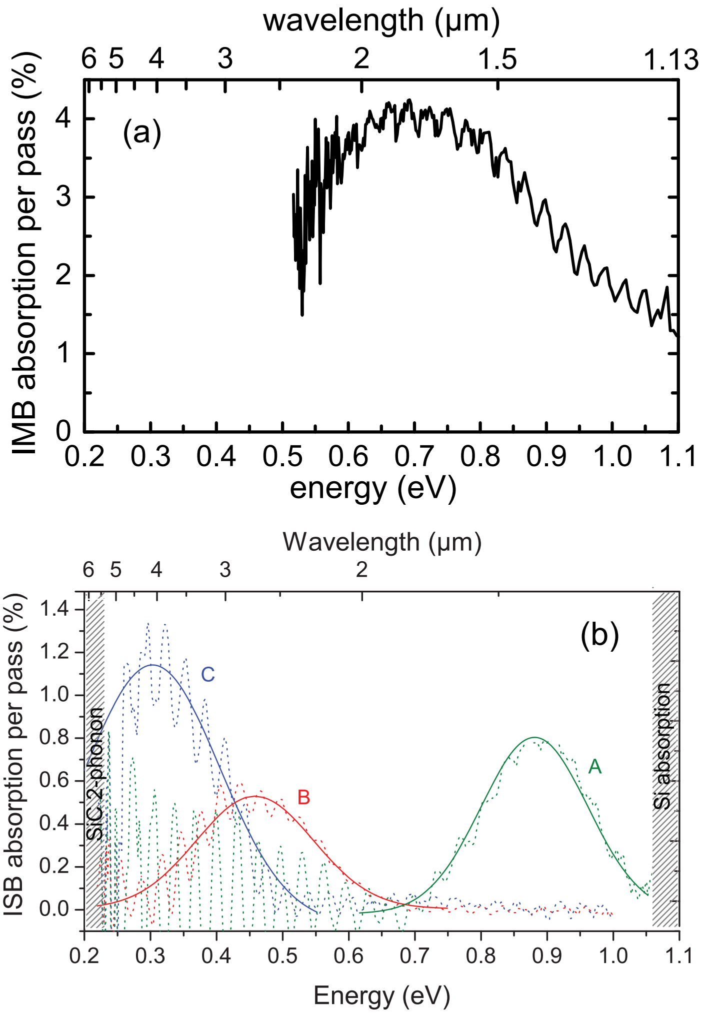

Fig. 3.6: (a) Spectrally resolved IMB absorption sample per pass trough the cubic GaN/AlN superlattice with nominally 1.8 nm wide wells and 1 nm wide barriers. (b) IMB absorption of cubic GaN/AlN superlattices with 3 nm AlN barrier widths and 2 nm (A), 3 nm (B) and 5 nm (C) GaN quantum well width (taken from Machhadani et al. [41]).

barriers have a substantial effect on the width of the IMB transition, as expected from the physics of superlattices discussed above. In addition, the doubled number of quantum wells in the 2nm/1nm superlattice presumably leads to further broadening.

The IMB absorption is now compared to the energy level simulations presented in the previous section. The quantum well thickness is assumed to be one monolayer thicker than intended, i.e. 2.025 nm, as has been pointed out above. Using this parameter, the central energy of the IMB absorption in Fig. 3.6(a) of ~0.7 eV is in good agreement with the predicted energy level splitting between the subbands $e1$ and $e2$ of 715 meV. However, the simulations cannot give any information about the width of the transition, as they do not tread the superlattice but only a single quantum well. In combination with the satisfying congruence of the inter-band energies seen in the simulations and the PL data, the match of the IMB energy further confirms the validity of the simulations.

Chapter 4

Ultrafast Carrier Dynamics and Resonant Inter-Miniband Nonlinearity

The design of electro-optical or all-optical applications of intersubband transitions in heterostructures requires the knowledge of the ultrafast nonlinear optical behavior of the involved transitions. In addition, the time scales of the electron dynamics often give insight to different scattering processes in the structure and, thereby, reveal details about microscopic interactions, which are not readily observable. In order to classify the cubic GaN/AlN superlattice in these respects, the ultrafast and nonlinear dynamical response of the inter-miniband (IMB) transition is analyzed in this chapter. The principles of time-resolved pump-probe measurements are discussed along with the experimental setup in the following section. More specifically, a degenerate femtosecond pump-probe setup is utilized to determine the lifetime of electrons in the upper subband $e2$, that are optically excited from the lower subband $e1$ (see Section 4.2). Afterwards, the third-order optical nonlinearity $\chi^{(3)}$ associated with the IMB transition is extracted in Section 4.3. This quantity is a measure for the efficiency of potential optical and optoelectronic devices.

Parts of the results of this chapter have already been published in Ref. [17].

4.1 Experimental Method: Pump-Probe Spectroscopy

Carrier dynamics in semiconductors happen on timescales of $\leq 100\,\mathrm{fs}$ (carrier-phonon and carrier-carrier scattering, see Ref. [61], p.11 and pp.135ff) to several ns (radiative interband recombination, see Ref. [62], pp.639ff). Detecting the signatures of transient changes in the electronic system, e.g. in the occupation of levels, in a time-resolved manner is key to the characterization of semiconductor heterostructures. The question of interest is often connected to the lifetime of electrons, e.g. 'How fast do electrons relax from higher energy level A to a lower energy level B?'. The answer to these problems not only yield the searched-for time-scales, but also allows one to draw conclusions about the underlying physical processes.

In the context of this thesis, the quasi two-level system composed of the electronic minibands $e1$ and $e2$ is under investigation, and the specific question is about the lifetime of electrons in the upper miniband $e2$. The dynamics of the electrons in the IMB system determine the speed and efficiency of potential applications based on nonlinear optical interactions in this structure.

A common way to get insight into electron dynamics in solids is to analyze the change of light-matter interaction arising from a change in the electronic system. This change might be induced by electronic or optical means. For example, the strength of the absorption in a two-level system, that resonantly interacts with photons, is determined by the occupation of the levels. In this case, insight to the temporal dynamics of the (excitation-induced) occupation can be gained by performing a time-resolved measurement of the optical transmission. Since the temporal resolution of electronic and optoelectronic devices, such as photodiodes or oscilloscopes, is limited to a few ps at best, more advanced tools are needed to study ultrafast electron dynamics. The invention of mode-locked laser sources gave rise to a novel method of monitoring temporal dynamics of electrons, called time-resolved pump-probe spectroscopy [61]. Using laser pulses with a temporal duration in the order of 10 fs-100 fs, it is feasible to detect electron dynamics in the sub-ps regime. In the following, the principles of time-resolved pump-probe measurements are presented by the example of the experimental setup used for studying the electron dynamics in the cubic GaN/AlN superlattice.

The essential idea behind the time-resolved pump-probe technique is the following: First, a non-equilibrium state is generated in the system using a pulsed optical excitation, called pump pulse. Then, the pump-induced changes to the electronic system alter the optical properties of the material in a way that affects the light-matter interaction with a second pulse, called probe. Probing might be done in transmission or reflection geometry via changes in the intensity, phase or spectrum of the probe pulse. Details on how pump and probe pulses interact via the cubic GaN/AlN superlattice structure will be given below, when the results are discussed.

It is now assumed that pump and probe pulses arrive at the sample with a time delay $\Delta\tau$. The algebraic sign of $\Delta\tau$ is defined such that the pump pulse precedes the probe pulse for $\Delta\tau > 0$. By varying $\Delta\tau$, the temporal dynamics of the pump-induced effect that follow the pump-matter interaction are resolved. The alteration of the probe signal with varying $\Delta\tau$ reflects the temporal evolution of the pump-induced effect, i.e. how the electronic system relaxes back to the equilibrium state.

A major advantage of this method is the unmatched temporal resolution, which is limited only by the duration of the pulses. Assuming both pulses have an equal duration t (FWHM), and they are Gaussian in the time domain, the temporal resolution is determined by the width of the convolution of the pulses $\sqrt{2}t$ (FWHM). Pulsed lasers emit a pulse train with a temporal distance of $1/f_{\text{rep}}$ between consecutive pulses, where f_{rep} is the repetition rate.

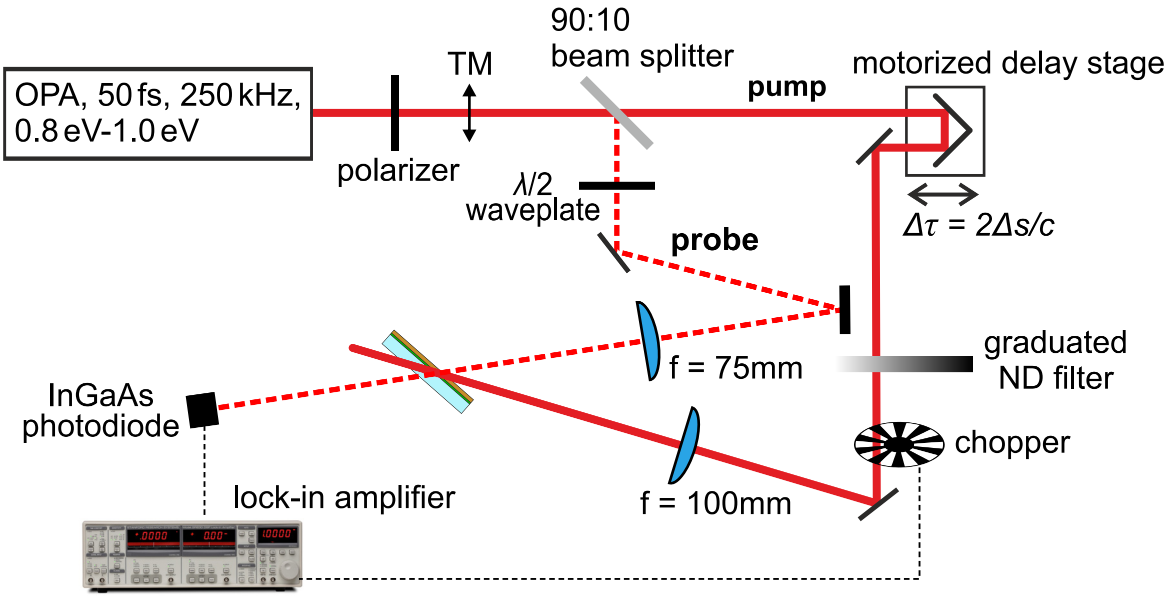

Fig. 4.1: Sketch of the experimental pump-probe setup. The pulsed output of an optical parametric amplifier (OPA) is split into pump and probe pulse trains. Polarization optics controls the polarization state of both beams. A motorized delay stage allows to tune the time delay $\Delta\tau$ between the pulses. The sample is tilted to ensure a light-IMB interaction angle $\theta > 0$, cf. Fig. 3.5(b). The single-pass probe transmission is recorded using a lock-in amplifier (Stanford Research 830) referenced to the pump excitation.

The maximum useful time delay $\Delta\tau$ is therefore limited by $1/f_{\text{rep}}$.

In addition to the temporal resolution, a distinct benefit of the pump-probe scheme is the lack of any necessity to temporally resolve the time scales of the pulses duration or the repetition rate. For every time delay $\Delta\tau$, the probe signal can be averaged over time scales that ensure good signal-to-noise ratios (usually ms-s). A fast temporally resolved measurement of electronic signals is circumvented.

Fig. 4.1 shows a simplified scheme of the utilized pump-probe setup. The light source is an optical parametric amplifier (OPA) emitting a train of ≈ 50 fs (FWHM) pulses at 250 kHz repetition rate[1]. The central wavelength is tunable from 1200 nm (1 eV) to 1600 nm (0.8 eV), which is close to the center of the IMB resonance. After the correct polarization (TM, parallel to the plane of the optical table) is ensured by a sheet polarizer, the laser output is divided into a high-power pump and a low-power probe beam. The polarization state of the probe beam is set by a $\lambda/2$ waveplate.

A crucial element of the time-resolved pump-probe scheme is the introduction of the

---

[1] Coherent OPA 9850 in combination with an external pulse compressor. This laser is pumped by a RegA 9040 (regenerative amplifier), seeded by a titanium:sapphire oscillator (Micra-18) in combination with a Verdi V-18 532 nm pump light source. The laser system is also used for some of the experiments presented in Chapters 9 and 10. For details on the laser system see Refs. [63] and [64].

time delay $\Delta\tau$ using a motorized mechanical delay stage. Assume that pump and probe pulses travel the same distance s from the beam splitter to the sample when the delay stage is at a corresponding position. In this case, the pulses arrive at the sample simultaneously and $\Delta\tau = 0$. When the stage now moves by Δs to the right side in Fig. 4.1, the distance that the pump pulses travel increases. Since the speed of light c is not infinite, this increment Δs translates into a time delay $\Delta\tau = 2\Delta s/c$. The stage utilized in the actual setup offers a travel range of 25 mm and sub-micron accuracy.

Both pulse trains are focused onto the sample with a relative angle of $\approx 10°$ between the beams. Using a rotating slit beam profiler, it is made sure that both beams spatially overlap in the sample plane, which is equal to the focal plane of the probe beam. In order to ensure a nearly homogeneous pump irradiance across the probed area, the probe spot diameter of $\approx$30 µm (FWHM) is smaller than the pump spot diameter of $\approx$50 µm (FWHM). The transmission of the probe pulse train through the sample T is measured with an InGaAs photodiode connected to a lock-in amplifier, which is referenced to the pump excitation using a mechanical chopper wheel. By this means, the principles of lock-in detection offer superior accuracy and make sure that the measured signal only shows pump-induced changes ΔT to T. In order to determine the normalized change $\Delta T/T$, the absolute probe transmission T is taken beforehand by placing the chopper in the probe beam.

Sample Geometry

The sample geometry has to be adapted to this two-beam pump-probe experiment. A waveguide configuration is excluded since the spatial and temporal overlap of the focused beams during the propagation through the waveguide cannot be maintained. Instead, a single pass through the superlattice far away from normal incidence is investigated. The volume of the superlattice layer is small, and signal contributions from the Si and SiC substrate could potentially disturb or even surpass the signatures of the IMB electron dynamic. In preliminary studies of the substrate Si+SiC layers, the effect of the two-photon absorption

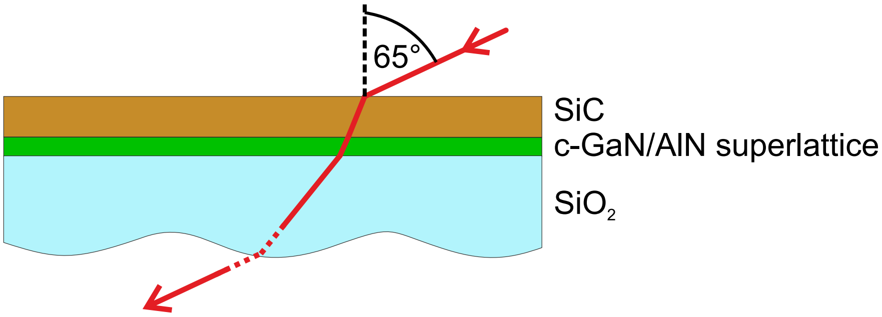

Fig. 4.2: Sample geometry in the pump-probe experiments where the single-pass transmission is measured. The superlattice layer is sandwiched between SiC and SiO2 layers.

of pump photons in Si on the probe transmission is found to be as strong as 30 %[2]. Isolating the superlattice from all substrate layers would be most desirable. To tackle this issue, the sample is glued onto a fused silica window and the Si is then removed mechanically (it is ground off). As a result, the cubic GaN/AlN superlattice is effectively sandwiched between the SiC layer and the fused silica substrate (cf. Fig. 4.2), i.e. dielectrics with rather small nonlinear optical response.

A second sample based on a bare SiC+Si wafer is processed in the same way. This sample is used as a reference in order to single out effects caused by the SiC and SiO_2 layers. In the pump-probe data presented below, the signals of the reference sample are subtracted from the transients obtained in the superlattice sample. Furthermore, the data is averaged over several scans.

Sufficient light-IMB interaction is achieved by tilting the sample. The angle of incidence (AOI) of the pump beam is $\approx 65°$, which is close to the Brewster angle where the reflection of TM polarized light is minimized. Note that the angle of interaction in the superlattice (see Fig. 3.5(b)) is reduced to $\theta \approx 24°$ due to strong refraction at the air-SiC interface. A variation of the AOI or the polarizations provide additional means to validate the IMB transition in the superlattice as the source of the transient optical response.

4.2 Ultrafast Inter-Miniband Carrier Dynamics

One of the major questions in the investigation of the superlattice is tackled in this section, namely the time scales of the IMB electron dynamics. The experimental setup, the methodology of pump-probe experiments and the sample geometry have been presented in the previous section. In a first step, the strength of the pump-induced alteration of the IMB electronic system is analyzed and compared to literature data. Next, the temporal dynamics are presented and assigned to the movement of carriers in the $E(\mathbf{k})$-system of the IMB levels.

The pump-probe transients are shown for different optical configurations in Fig. 4.3. The central photon energy of pump and probe pulses is 0.82 eV ($\lambda = 1.52\,\mu$m). In a first step, the configuration where the IMB transition is expected to be addressed most is discussed (cf. red curve, 65° AOI, TM polarization). At $\Delta\tau \approx -100$ fs, the pump-induced transmission change begins to increase. It peaks at zero time delay, followed by an exponential decay until the signal has nearly vanished for $\Delta\tau > 500$ fs. A maximum relative transmission increase of $\Delta T/T = 3.2 \cdot 10^{-3}$ is seen, which can be assigned to a substantial Pauli blocking of the probe transmission in the two-level system. The sign of $\Delta T/T$, the

---

[2] This signal most likely stems from the free carrier absorption at pump-induced carriers. This process occurs when a photon is absorbed from a free carrier in an excited state to an unoccupied state in the same band (cf. Ref. [50], pp.306ff). In the present experiment, carriers are excited by two-photon absorption of pump photons across the indirect band gap of silicon ($\approx$ 1.1 eV) into the conduction band.

fast electron relaxation times and the experimental checks discussed below confirm this proposition.

Pump-Induced Saturation of the Probe Absorption

Pauli blocking, which is often also referred to as transmission bleaching or saturation of absorption, results in a decreasing absorption coefficient for increasing light intensities (see Ref. [3], p.514). In the present case of a resonant interaction of pump and probe pulses with an effective two-level system, the physical reason for the pump-induced transmission increase is as follows: The absorption of pump photons from states the subband $e1$ creates a strong population in the upper subband $e2$. Consequently, the absorption of probe photons is decreased because of the reduced number of occupied initial states (in subband $e1$) and free final states (in subband $e2$). The name 'Pauli blocking' stems from the Pauli exclusion principle, which states that two electrons cannot occupy identical quantum states. In semiconductors the relevant quantities are energy, wave vector and spin. In Fermi's golden rule, the transition rate from initial states i to final states f is given by $\Gamma_{i\to f} \propto \sum_i |\langle f|H'|i\rangle|^2 \rho_f$. It linearly depends on the density of final states ρ_f (free states in subband $e2$), which is reduced by the pump-excitation. In addition, the absorption of pump photons reduces the number of initial states (electrons in subband $e1$), whereby the total transition rate is decreased further.

It is instructive to set the pump-induced transmission change in relation to the total strength of the IMB absorption in the pump-probe sample geometry. The optical density

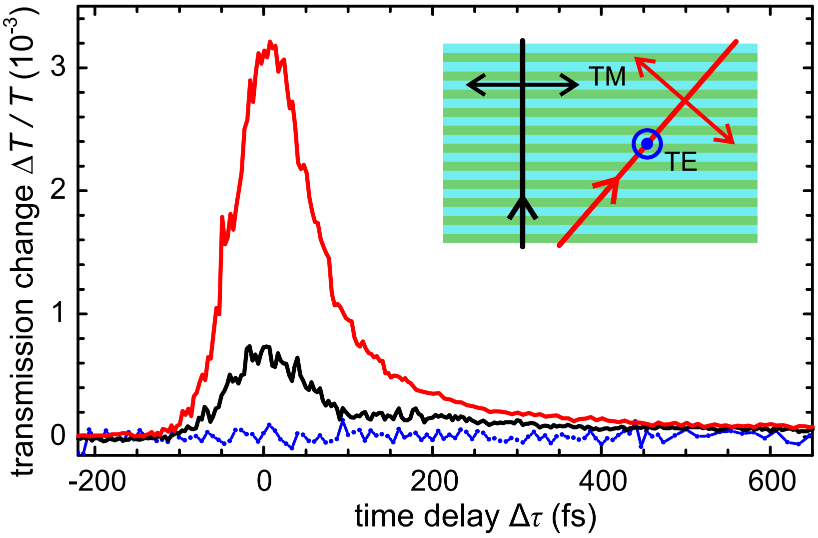

Fig. 4.3: Pump-induced change of the optical transmission through the superlattice for a central photon energy of 0.82 eV and a pump irradiance of 36 GW/cm^2 for different configurations. Red: TM, angle of incidence 65°, TM. Black: TM, normal incidence. Blue: TE, angle of incidence 65°. The inset illustrates the different configurations.

of the single-pass IMB absorption can be estimated based on the data obtained for the waveguide geometry, which gives $\alpha_{\mathrm{w}} L_{\mathrm{w}} \approx 0.036$ (see Fig. 3.6). Here, α is the absorption coefficient and L is the length of interaction, as used in the Lambert-Beer law $I(L)/I_0 = \exp(-\alpha L)$. To account for the reduced angle of interaction θ in the pump-probe geometry (pp), compared to the waveguide (w), two effects have to be considered: First of all, the effective interaction length $L_{\mathrm{pp}} = L/\cos(\theta)$ shortens, with $L = 80\cdot(1+2.025)\,\mathrm{nm} = 242\,\mathrm{nm}$ being the thickness of the superlattice. Secondly, $\alpha_{\mathrm{pp}} = \alpha \sin(\theta)$ is reduced, because a smaller fraction of the electric field is parallel to the IMB dipole moment (α is the maximum absorption coefficient for $\theta = 0$). When taking both effects into consideration, the absorption strength in the pump-probe geometry can be estimated to be

$$\alpha_{\mathrm{pp}} L_{\mathrm{pp}} = \alpha_{\mathrm{w}} \frac{\sin 24^\circ}{\sin 43^\circ} \cdot L_{\mathrm{w}} \frac{\cos 43^\circ}{\cos 24^\circ} \approx 0.017\ . \tag{4.1}$$

The maximum change to this absorption of $3.2\cdot 10^{-3}$, seen in Fig. 4.3, points to a remarkably strong pump-induced reduction of the IMB absorption strength of nearly 20 %. Apparently, the upper subband is massively populated by the pump excitation.

Before moving on to an analysis of the temporal dynamics of the signal, the above results are compared to two configurations where the IMB transition is not expected to affect the optical transmission. Firstly, close-to-normal incidence of pump and probe beams is analyzed, cf. black line in Fig. 4.3. To compensate for the smaller spotsize on the sample surface, the pump power is lowered such that the irradiance is kept constant. This configuration results in a marked decrease of the pump-induced transmission change. The remaining signal strength can be also attributed to Pauli blocking. Surface roughness and light scattering at surface roughness cause a fraction of the incident light fields to interact with the IMB transition. On the one hand, roughness is known to partially allow for otherwise forbidden transitions because the optical selection rules are party relaxed [48]. On the other hand, undulations of the surface layer and the superlattice interfaces cause part of the electric field to be oriented along the IMB dipole moment. Refraction at interface roughness further adds to this effect.

In a second set of control experiments, the AOI is again set to 65° but probe beam is changed to TE polarization, cf. blue dotted line in Fig. 4.3. As expected, no pump-induced changes are found in this configuration. The probe radiation cannot interact with the IMB transition regardless of the aforementioned detrimental sample properties. Taken together, these checks confirm the pump-probe signals to originate from the IMB transitions.

Electron Relaxation Times

The temporal evolution of the transmission change gives insight into the timescales of the inter-miniband electron dynamics. The signal reduction following the overlap peak at

$\Delta\tau = 0$ is governed by an exponential decay with a time constant of $\sim$80 fs, reflecting the relaxation of electrons into the lower subband. This time scale is in fair agreement with theoretical predictions for the inter-subband electron relaxation times, which calculate electron-LO phonon scattering times to be $\sim$100 fs [34–36]. Reports on hexagonal GaN/Al(Ga)N multi-quantumwell structures with ISB transition energies from 0.7 eV-0.8 eV found time scales ranging from 130 fs to 370 fs [35–38; 65]. The fast relaxation times measured here in the cubic superlattices are in part related to the improved temporal resolution of the setup. Furthermore, scattering at surface and inter-layer roughness may enhance the carrier relaxation.

The ultrafast electron relaxation approaches the limit of the time resolution of the setup which is $\approx$70 fs. Furthermore, the employed pump-probe scheme necessarily is degenerate in energy and polarization, which favors potential light-light interaction to show up in the signals[3] To clearly distinguish pump-induced changes in the band population from nonlinear interactions of pump and probe pulses during the time overlap, a benchmark for the time resolution of the setup is obtained. For this purpose, intensity autocorrelations in a 400 nm thin intrinsic GaAs wafer are performed. They are based on two-photon absorption generated by the combination of one pump photon and one probe photon, hence this kind of signal can only be seen during the temporal overlap of both pulses (see Ref. [62], pp.710-711).

---

[3] The signals are strongy disturbed by interferences of probe light with pump light that is, presumably, scattered into co-propagation by surface roughnesses. To get rid of this influence, one of the mirrors in the probe arm is attached to a piezo acuator, which periodically moves back and forth. The lock-in time-averages the resulting alteration of the interference and, thereby, cancels it out of the actual probe transmission signal.

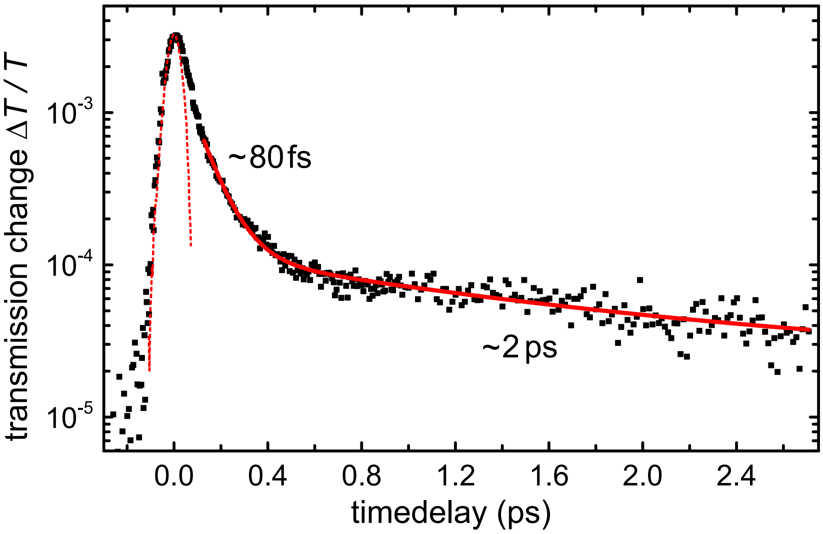

Fig. 4.4: Pump-probe transients for a central photon energy of 0.82 eV, a pump irradiance of 36 GW/cm^2, an angle of incidence of 65° and TM polarization (black dots). The solid red line a bi-exponential fit to the data. An intensity autocorrelation as measured from two-photon absorption in GaAs (red dashed line) indicates the temporal overlap of the pulses.

Fig. 4.4 displays the autocorrelation (red dashed line, ≈70 fs FWHM) together with the above-presented transient data recorded with the cubic superlattice (65° ,TM, black squares) in a semi-logarithmic scale. It is evident from the data for $\Delta\tau > 100\,\mathrm{fs}$ that a significant pump-induced change is present after the temporal overlap. Thus, it is ensured that this signal is indeed caused by changes in the band occupation.

The semi-logarithmic representation of the data reveals further details of the IMB electron dynamics. If the data is fitted with a double exponential decay (red line), a residual signal decaying with a time-scale of $\sim 2\,\mathrm{ps}$ is seen, which has been attributed to the thermalization of the excited electron ensemble in previous studies [35; 36]. Similar time-scales and conclusions have been reported using a GaN/AlN quantum dot superlattice [65]. In this picture, the initial fast signal decay represents IMB transitions, in which states with the same $k_\perp$ are involved (vertical transitions in **k**-space). The slow contribution reflects the relaxation of carriers to the Γ-point at $k_\perp = 0$ (sliding down the dispersion to the minimum of the parabola). It should be noted, however, that the time constant of the slow decay varies from 1 ps to 5 ps when comparing the results obtained with different photon energies (see next paragraph) or samples. Furthermore, the transients recorded with the reference sample show similar slow signatures. Hence, it cannot be excluded that the slow contribution originates from multi-photon absorption in the SiC layer.

In the final step, the spectral dependence of the pump-probe dynamics associated with the IMB transition are analyzed. This is done in order to see if the electron dynamics change for different energies within the IMB transition. The design of potential applications and devices requires the knowledge of the electron dynamics across the entire spectral range of the utilized transition. The degenerate pump-probe measurements presented above are repeated for different photon energies of TM polarized light at an AOI of 65°, which is the geometry of maximized light-IMB interaction. Since the pulse length slightly changes when tuning the output energy of the laser, intensity autocorrelations are recorded for the different energies. Note that the spectral tuning range of the OPA system admittedly does not permit to cover the broad IMB absorption resonance depicted in Fig. 3.6.

Exemplary pump-probe transients are displayed in Fig. 4.5. From the top to the bottom panel, the photon energies move closer to the peak of the IMB resonance. The electron relaxation times are again extracted by fitting an exponential decay to the data after the overlap peak. No significant deviation from a $\sim 80\,\mathrm{fs}$ decay time is found, which indicates rather universal electron dynamics in the investigated spectral range. The maximum amplitudes of the pump-induced change do not strictly follow the spectral dependence of the IMB absorption strength, even when taking the different pump irradiances into consideration. This finding may be explained by the spatial inhomogeneities of the samples and different illuminated spots during the measurements for different photon energies.

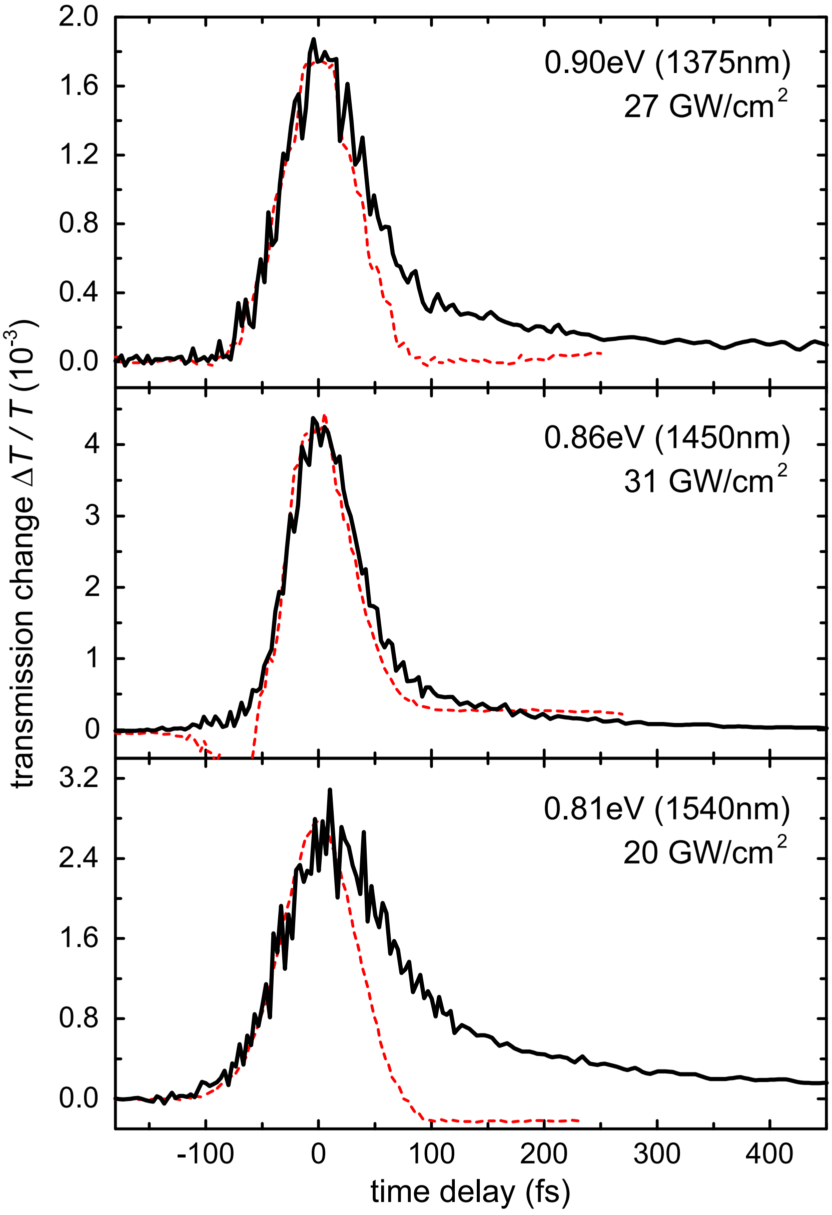

Fig. 4.5: Pump-probe transients for a different central photon energies stated in the panels together with the respective pump irradiance. The angle of incidence is 65° and the pulses are TM polarized. The red dashed lines are intensity autocorrelations of the pump and probe pulses as measured as measured from two-photon absorption in GaAs.

4.3 Estimation of the Third-Order Nonlinearity of the Inter-Miniband Transition

In the final part of the study of the cubic GaN/AlN superlattice, the optical nonlinearity $\chi^{(3)}$ associated with the IMB transition is estimated. This quantity is used to characterize the strength of light-matter interaction in the nonlinear optical regime and helps to compare materials for electro-optical or ultrafast all-optical applications. Before moving on to the extraction of $\chi^{(3)}$ from pump-probe data sets, a brief introduction to nonlinear optics is given.

Introduction to Nonlinear Optics

The field of nonlinear optics studies effects that arise from the modification of the optical properties of a material due to the presence of a strong light field [66]. Sufficiently high light intensities became available with the invention of the laser in the early 1960s. Shortly after, the second-harmonic generation was discovered, which is still one of the most prominent examples of nonlinear optical effects (e.g. most 532 nm (green) lasers, even low power laser pointers, rely on it). Nowadays, effects like sum- or difference frequency generation, saturable absorption or self-focusing effects are present in various photonic devices. It is obvious that the pump-probe measurements presented above must belong to the area of nonlinear light matter interaction, since pump radiation changes the properties of the material which, in turn, alters the probe-matter interaction.

In linear optics, the optical response of a material is characterized by the light-induced polarization in the material $\mathbf{P} = \epsilon_0 \chi \mathbf{E}$, where the susceptibility χ describes the strength of interaction. This expression can be used as an approximation as long as the properties of matter are not changed by the light itself. More specifically, the linear proportionality holds as long as the atomic Coulomb potentials can be assumed to be parabolic. In this case, light-matter interaction depends on frequency and polarization of light, but not on its field strength. Everyday phenomena like the reflection or transmission of light are independent of the light's power. For example, the color of an object does not change when the strength of illumination is changed.

At high field strengths, a more general description is necessary and the susceptibility (or polarization) is written as a power series

$$\mathbf{P}(\mathbf{E}) = \epsilon_0[\chi^{(1)} + \chi^{(2)}\mathbf{E} + \chi^{(3)}\mathbf{E}^2 + ...]\mathbf{E} \ , \tag{4.2}$$

where $\chi^{(1)} = \chi = \epsilon - 1$ and ϵ is the dielectric function. The n-th order nonlinear susceptibilities $\chi^{(n)}$ are complex tensors of $(n + 1)$-th rank.

In the language of nonlinear optics, different processes are referred to as a '$\chi^{(n)}$ effect' depending on their power dependence. The generation of the second harmonic, for example, is related to the second order nonlinearity $\chi^{(2)}$, since the power of the second harmonic depends quadratically on the input power. For further characterization, the frequency components of the participating incoming and outgoing electric fields or polarizations are often denoted as an argument of the susceptibility. Effects of arbitrary order in different materials are classified by this macroscopic description, irrespective of microscopic electronic or structural details.

The pump-probe measurements presented above rely on the mechanism called Pauli blocking or saturation of absorption. Although this experimental technique requires two beams, the saturation of absorption can also be observed in one-beam experiments where the relative transmission of a beam ($I_{\text{out}}/I_{\text{in}}$) is not constant but increases with the beam's power. In the pump-probe measurements, the probe pulses merely detect the strength of the pump-induced change to the optical system. Optical elements such as saturable absorbers or all-optical switches are based on this effect. It is related to the imaginary part of the third-order nonlinearity $\text{Im}\chi^{(3)}$, since the deviation from linear optical behavior is caused by the light-induced filling of the upper energy level, and the amount of carriers generated by the absorption of pump photons increases linearly with the intensity of light $I \propto \mathbf{E}^2$.

Resonant Inter-Miniband Optical Nonlinearity $\chi^{(3)}$

For the purpose of estimating the third-order nonlinearity of the cubic GaN/AlN superlattice, a set of pump-probe measurements with varying pump irradiance is performed. In Fig. 4.6, the maximum transmission change at nominally zero time delay is plotted versus the irradiance of pump pulses of 0.81 eV photon energy. The data points nicely follow a linear fit to the data, which indicates that the absorption of the pump pulse does not generate any detectable self-saturation and the experiment is restricted to the $\chi^{(3)}$ regime[4]. Note that the pump power has no significant influence on the electron relaxation times or the overall temporal shape of the transients.

The magnitude of the third-order nonlinear susceptibility $\text{Im}\chi^{(3)}$ is now estimated following a procedure done by Hamazaki et al. [38]. In order to extract $\chi^{(3)}$, a relation between the third-order and the linear susceptibility of a two-level system is used. It reads

$$\text{Im}\chi^{(3)} = \frac{-\text{Im}\chi^{(1)}}{3|E_S|^2} \tag{4.3}$$

where E_S is the field strength related to the saturation irradiance I_S (see Ref. [66], p.205). This quantity corresponds to the irradiance that is needed to generate a complete pump-induced blocking of absorption in the two-level system composed of the subbands $e1$ and $e2$. It is given by $I_S m = \alpha L$, where $m = 1.25 \times 10^{-4}\text{cm}^2/\text{GW}$ is the slope of the line fit

---

[4] A self-saturation of the pump pulse could happen due to Pauli blocking of the absorption of the temporally trailing part of the pulse, caused by the occupation in the upper level that is generated by the temporally leading part of the pulse. This behavior would shift the pump-probe process to the $\chi^{(5)}$ regime.

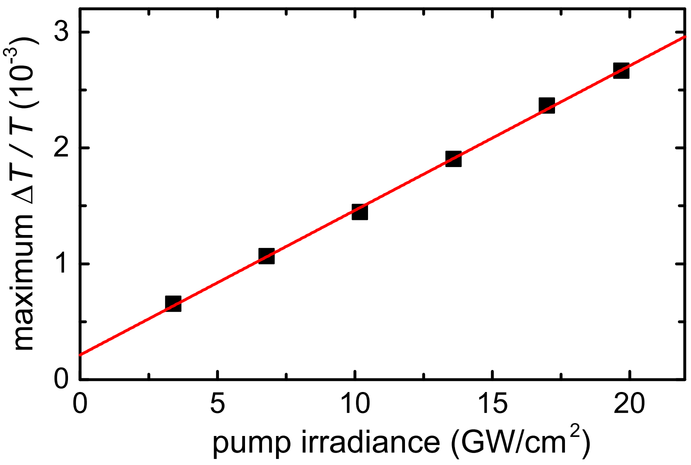

Fig. 4.6: Dependence of the peak pump-probe signals on the pump irradiance (central photon energy 0.81 eV, TM polarization, 65° angle of incidence). The red line is a linear fit.

in Fig. 4.6. In a more illustrative picture, I_S is the irradiance at which the extrapolation of the data given by the line fit reaches the total absorption strength. The optical density of the pump-geometry is calculated in Eq. (4.1) to $\alpha_{\rm pp} L_{\rm pp} = 0.017$. Using these numbers, the saturation irradiance is estimated to be $I_S = 136\,\mathrm{GW/cm^2}$ for the given experimental parameters .

In the next step, $\mathrm{Im}\chi^{(1)}$ is calculated from the linear optical properties of the superlattice using $\mathrm{Im}\chi^{(1)} = \mathrm{Im}\,\epsilon$, $\epsilon = (n + ik)^2$ and $k = \lambda\alpha/4\pi$, which gives $\mathrm{Im}\chi^{(1)} = 2kn \approx 0.42$. Here, α is extracted from the strength of the IMB absorption presented in Fig. 3.6 and corrected for the reduced angle in the pump probe geometry. The refractive index of the superlattice is $n \approx 2.3$. The resulting third-order susceptibility is

$$\mathrm{Im}\chi^{(3)} \sim 1.1 \cdot 10^{-20}\mathrm{m}^2/\mathrm{V}^2\ . \tag{4.4}$$

This value is 1-2 orders of magnitude smaller than previously reported estimations based on hexagonal GaN/AlN multi-quantum wells (see Refs. [38; 67] and references therein). When comparing the heterostructures used in these studies with the present superlattice, the reduction can be attributed to two presumable reasons:

(i) The doping concentration in the cubic superlattice is at least one order of magnitude smaller. Less states are available for the IMB transition, which is why the total strength of the transition is reduced.

(ii) The strongly broadened transition and the sub-100 fs electron relaxation time point towards strong dephasing caused by surface and inter-layer roughness (see the discussion of the width of the IMB absorption in Section 3.3). Due to the broad transition, the effective nonlinearity is reduced, since less oscillator strength contributes to the optical response at a given photon energy.

Note that the estimate for $\chi^{(3)}$ only yields an effective value for the present geometry with a small interaction angle. When the pulses propagate parallel to the superlattice layers, the effective interaction strength with the IMB dipole moment is expected to rise by a factor of $1/\sin(24^\circ) \approx 2.5$. Since the third-order nonlinearity is proportional to the fourth power of the dipole moment (see Ref. [66], p. 205), the tensor element $\chi^{(3)}$ is expected to be a factor of ≈ 39 larger in this configuration.

Chapter 5

Conclusions and Outlook Part I

The spatial confinement of carriers in semiconductor superlattices leads to the generation of a two-level miniband system with fabrication-tailored transition energies in the telecom wavelength regime. Utilizing multiple reflections in a waveguide geometry, the interminiband (IMB) transition in a cubic GaN/AlN superlattice is characterized in Section 3.3. The resonance is found to be centered at ~ 0.7 eV with an energetic width of ≈ 370 meV (FWHM). It is strongly broadened due to (i) the tunneling-induced coupling of wavefunctions across the narrow 1 nm AlN barriers, and (ii) scattering processes at surface roughness and inter-layer roughness as well as monolayer fluctuations of the QW thickness. In the context of potential applications, a broad transition is beneficial for detectors spanning a large wavelength range with a single device.

Simulations of the inter-band and inter-subband transition energies agree well with the experimental data, if the GaN quantum well thickness is assumed to be 2.025 nm instead of the nominally intended 1.8 nm. There is strong evidence that the predictions of the energy levels attained by the simulations are sufficiently precise to design the transition energies of cubic GaN/AlN heterostructures.

The ultrafast electron dynamics in the cubic GaN/AlN superlattice are studied employing resonant time-resolved pump-probe spectroscopy in Section 4.2. Several checks based on different configurations confirm the nonlinear optical response to originate from the saturation of the IMB absorption. The IMB relaxation times are found to be ~ 80 fs for photon energies in the range 0.8 eV-0.9 eV, which indicates a faster electron relaxation compared with GaN/AlN heterostructures used in previous studies. There is no apparent reason to expect a significant change of the relaxation times for other photon energies within the broad IMB resonance.

In a second set of experiments, the third-order nonlinearity $\mathrm{Im}\chi^{(3)}$ is extracted from the dependence of the maximum pump-induced change on the pump irradiance, cf. Section 4.3. This quantity is a benchmark for the potential efficiency of applications based on nonlinear optical interactions in the IMB system. The estimation yields $\mathrm{Im}\chi^{(3)} \sim 1.1 \cdot 10^{-20} \mathrm{m}^2/\mathrm{V}^2$.

This value is smaller than previously published results based on hexagonal GaN/AlN superlattices, but there are routes for an enhancement. First of all, there is some room for improvement by stronger doping. Secondly, engineering narrower IMB resonances for specific energy ranges and an overall improvement of the layer quality would enhance the nonlinearity.

Ongoing studies aim to elucidate the effects of tunnel coupling and scattering processes. A series of superlattice samples with varying AlN barrier thickness (1 nm, 3 nm, 5 nm) is currently under investigation. The results are expected to give insight into the respective roles of tunnel- and scattering-induces broadening, since the barrier thickness determines the magnitude of the coupling between the wells. The width of the transition is expected to be reduced for wider barriers and the IMB nonlinearity of these samples is potentially larger. Furthermore, the effects of δ-doping and barrier doping on the IMB transition and the nonlinear properties of the sample will be studied.

Resently, is has been shown that combining ISB transitions with plasmonic metasurfaces drastically boosts the efficiency of nonlinear optical processes [68; 69]. Light is confined to the near field of metallic nano-antennas and normal-incidence light is converted into field components that interact with the ISB transition. Thereby, geometrical and polarization restrictions are circumvent and the local light intensity is enhanced. Using InGaAs/AlInAs MQWs an gold nano-antenas, the efficiency of second harmonic generation at 8 µm was shown to be enhanced by up to 8 orders of magnitude [68]. This concept is currently being applied to the cubic GaN/AlN superlattices studied in this thesis, which operate in the telecom wavelength regime. In currently ongoing studies, arrays of gold nano-antennas are deposited on the superlattice and the potential enhancement of the second harmonic generation is investigated.

Part II

Photonic & Plasmonic Elements based on VO_2 Nanocomposites

Chapter 6

Vanadium Dioxide (VO_2) Nanocrystals

Vanadium dioxide (VO_2) has attracted the interest of researchers for decades since F. J. Morin first reported about the metal-to-insulator phase transition (MIT) occuring in certain transition metal oxides [18]. There are several vanadium oxides such as VO_2, V_2O_3 or V_2O_5 that show a MIT [18]. Vanadium dioxide (VO_2) is the technologically most relevant one, because the critical temperature of the phase transition is near ambient temperatures. The fascinating feature of VO_2 is the existence of different solid state phases that can be observed at easily accessible temperatures, which opens up the possibility for room-temperature operation of potential devices. Below the critical temperature $T_C \approx 68°\mathrm{C}$ (for bulk crystals), VO_2 is characterized by an insulating behavior while the high temperature phase is metal-like. During this reversible first-order phase transition, the lattice structure and the electronic band structure are strongly altered. The material properties of VO_2 and the physics of the MIT are outlined in Section 6.1.

What makes VO_2 so appealing for modern photonic applications is the marked change of the electrical conductivity by 4-5 orders of magnitude and, more importantly, the substantial modification of the dielectric function during the MIT [19; 70]. Closely related, the metallic phase features decreased transmission and an altered refractive index for near-infrared radiation in the telecom wavelength regime. In combination with the ability to induce the MIT thermally [18], via external stress [71], electronically [72] or optically [21] on time-scales of 100 fs to ns, this change of the light-matter interaction opens up a multitude of possible utilizations of VO_2 in photonics (see Chapter 7) and plasmonics (see Chapter 8). Apart from the applications in the broad field of photonics, VO_2 is also used in many areas of research such as solar cells and smart window coatings [73; 74], sensors [75; 76], actuators [77; 78] or transistors [79; 80].

Another advantage of nanoscale VO_2 systems is that they tend to endure mechanical stress generated by the MIT better than bulk crystals. Applications and devices would naturally profit from durable VO_2. The capability of the VO_2-NCs to withstand highly repetitive switching is addressed with all optical means in Section 7.1.

Similar to many areas of solid state physics, shrinking the size of VO_2-systems to the nanoscale in one or more dimensions gives access to novel properties and effects. In this thesis, VO_2 nanocrystals (NCs) embedded in a fused silica host are used for the demonstration of photonic and plasmonic elements. The optical response of the NCs is different from bulk samples in a way that boosts the performance of potential applications in the telecom wavelength regime. Owing to the special geometry of the NCs, a broad absorptive resonance is present, which results in a stronger change of the refractive index compared to thin-films or bulk crystals. Specifically, the MIT-induced change of the complex refractive index of the VO_2-NCs is examined in this thesis, see Section 6.2. In addition, the MIT-induced increase of the absorption in the VO_2-NC layer is spectrally resolved in a sufficiently wide spectral range that reveals the entire resonance.

For nanoscopic VO_2, the MIT shows a thermal hysteresis such that a supercooled metallic state can persist to temperatures somewhat below T_C when the material is cooled down from the high temperature phase. This phenomenon has gained much attention lately and is utilized for the demonstration of memristors or memory devices based on VO_2 [81–86]. A hysteresis is inherent to first-order phase transitions. While the width of the thermal hysteresis is small in bulk VO_2 crystals [18], it increases when the volume of the VO_2 is restricted to nanoscale dimension. The VO_2-NCs investigated in this thesis show a uniquely broad thermal hysteresis that is unmatched by other nanoscale VO_2 systems reported so far [21; 87]. Thus, the NCs offer great potential for memory applications. In this thesis, the hysteresis is utilized for the demonstration of reconfigurable photonic and plasmonic elements. Section **??** provides an experimental analysis of the thermal hysteresis and discusses the physical background of the strongly increased width.

The critical temperatures of the MIT in VO_2 strongly depend on the domain size, crystal quality and the surroundings of the VO_2 crystal, layer or nanoscale specimen. This dependence was made use of by doping or manipulating the VO_2 lattice structure during or after the fabrication for the customization of the thermal properties of VO_2. Section 6.4 gives an analysis of the effect of argon ion bombardment on the properties of the thermally induced MIT and the hysteresis of the phase transistion in VO_2-NCs. It is shown how the MIT of such processed NCs can be completely inhibited for high argon doses. While this technique has been used before [87], the possibility to tune the influence of argon doping on VO_2-NCs with selected argon doses has not been investigated so far.

Parts of the results presented in this chapter have already been published in Ref. [21].

6.1 Fundamentals of VO_2 and the Metal-Insulator Phase Transition

The following text provides a brief introduction into the basic material properties of the different phases of VO_2 and the physics of the metal-insulator phase transition (MIT). Note that in the following, the phase transition from the low-temperature insulating to the high-temperature metallic phase will be referred to as MIT. Many details of the complex interplay of different degrees of freedom that determine the MIT are a topic of ongoing discussions. Most experiments conducted in the context of this thesis do not aim to contribute to this debate, since the most fundamental details of the MIT are not crucial for the application-related research presented in this thesis. Thus, the discussion presented in this section will be only brief. The interested reader may follow the references given in the text.

The chemical element vanadium (V) is a transition metal with the atomic number 23. Fig. 6.1 displays the unit cells and the electronic band structures of the two solid state phases of VO_2 that are relevant for this thesis [88]. The discription is based on the work of J.B. Goodenough who was the first one to develope a widely accepted model [89]. A detailed, more modern analysis can be found in Ref. [90]. In the insulating phase for $T < T_C$, VO_2 crystallizes in a monoclinic (M_1) lattice structure and shows a band structure resembling a semiconductor with a band gap of $\sim 0.6\,\text{eV}$-$0.7\,\text{eV}$, as shown in Fig. 6.1(a)-(b)[1]. This gap is due to the splitting of the isolated $3d_{||}$ electron levels into lower-energy bonding and higher-energy antibonding states caused by V-V dimerization, crystal field splitting and/or electron-electron repulsion. The exact mechanism behind the formation of this band gap and the respective role of the before-metioned effects are still under debate, as will be discussed later in the text. Six oxygen atoms form an octaeder surrounding the body-centered V atom (not shown, for an illustration see Ref. [90]).

During the phase transition to the high-temperature metallic phase for $T > T_C$, the positions of the vanadium atoms change while the oxygen octaeder remains nearly unchanged. More specifially, the V-V pairs elongate and tilt towards the rutile c_R-axis, as shown in Fig. 6.1(b) [91]. The unit cell dimensions change by up to 1 % [90; 92]. The metallic phase features a rutile (R) (tetragonal body-centered) unit cell of V atoms, in which the V-V pairing is lifted. The $3d_{||}$ levels become degenerate and the energy of the $3d_{\pi^*}$ level shifts, such that the Fermi level now lies within these bands, cf. Fig. 6.1(d). Consequently, the partial filling of bands gives rise to a metallic character of the high temperature VO_2.

Note that more insulating phases and potential mixtures of those phases during the phase transition were discovered [93], which are only accessible when the VO_2 lattice is subject to substantial mechanical stress [71; 94; 95] or doping [96]. These phases may show up as a

---

[1] Historically, the term insulator has been established for the low-temperature phase since the phase transition was first observed based on the giant change in conductivity. Because of the small band gap, the low-T phase is often referred to as semiconducting or semi-insulating in modern literature.

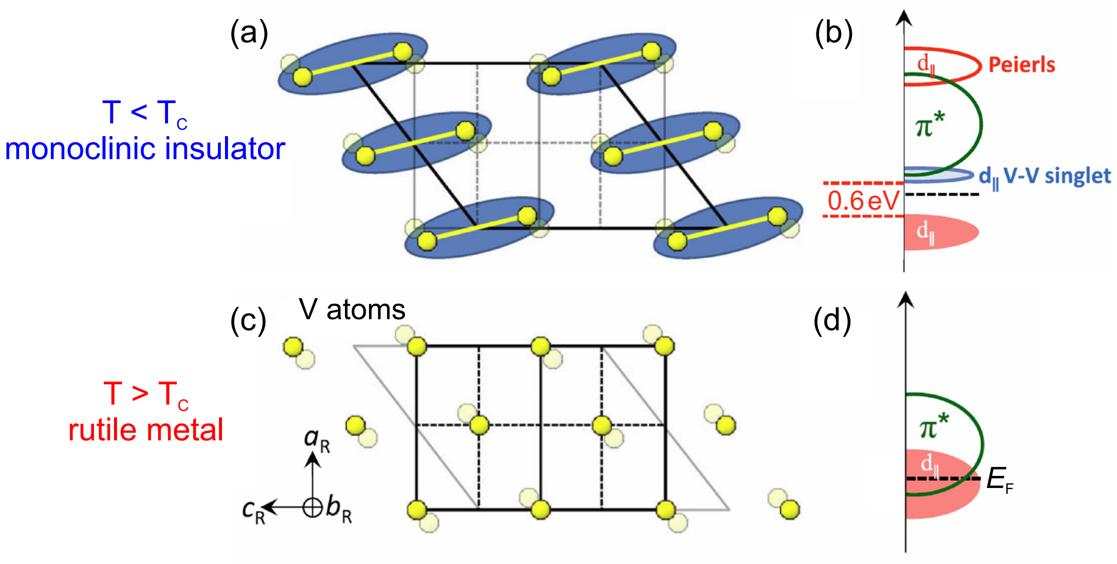

Fig. 6.1: Illustration of the insulating and metallic phases of VO_2 on the basis of the lattice structure and the density of states. Adapted from Gray et al. [88]. (a) In the low-temperature ($T < T_C$) insulating phase the lattice structure of VO_2 is monoclinic (M1) and neighboring V atoms (yellow) dimerize (O atoms not shown). Each V-V atomic pair shares a singlet electronic state composed of two strongly correlated V 3d electrons (blue). (b) Schematic densitiy of states and state occupation near the fermi energy E_F (dashed black line) for low-temperature ($T < T_C$) VO_2. The V-V paring in the insulating phase causes a splitting of the $3d_{||}$ orbitals along the c_R axis and the tilting of the V-V pairs shifts the $3d_{\pi^*}$ band to higher energies. (c) Rutile (R) lattice structure of the high-temperature ($T > T_C$) metallic phase of VO_2. (d) The metallic behavior for high-temperature ($T > T_C$) VO_2 is caused by the non-zero density of states at the Fermi level, which results in a partly filled conduction band.

intermediate states during the MIT [93]. Furthermore, a "photoinduced metallic-like phase of monoclinic VO_2" was found [97], i.e. a metastable phase that shows optical properties of the metallic phase while the lattice retains the characteristics of the insulating phase.

VO_2 belongs to a class of materials with strongly correlated electrons. The electron-electron interactions in these materials are complex and can neither be treated in a Bloch-like picture with unbound and freely moving electrons, nor can they be described based on localized, tightly bound isolated electrons. Coulomb repulsion usually inhibits the conductivity from being as good as in metals like copper or gold [98]. In metallic VO_2, this behavior arises from the fact that oxygen atoms separate the valence electrons that are weakly bound to vanadium nuclei and, thus, the overlap integral of electron wave functions is rather small. Modulations to the electronic interactions introduced by external stimuli to the structural system or electronic occupation of bands can cause drastic effects, such as the phase transition of VO_2.

The cause of the MIT has been debated for five decades and still is a topic of ongoing discussion, fueled by theoretical studies and recent time-resolved measurements illucidating the sub-ps dynamics of the phase transition. In essence, the debate centers around the character of the insulating phase and the cause for the formation of a band gap, i.e. the spitting of the $3d_{||}$ bands. It is an unresolved issue, whether VO_2 is a Peierls insulator where the structural changes (tilting, dimerization) are solely responsible for the opening of the band gap or to what extend electron-electron interactions play a role. The latter case would point towards VO_2 being a Mott(-Hubbard) insulator. There is theoretical and experimental evidence for both the Peierls [89; 99–102] and the Mott picture [103–106] that, taken together, suggest a complex delicate interplay of structural and electronic degrees of freedom [85; 97; 107]. Many authors account for this complication and state that "nonlocal correlations effectively assist the Peierls-like transition" [101] or even call the MIT an "orbital-assisted 'collaborative' Mott-Peierls transition" [108]. An overview of very recent developements in this discussion can be found in Ref. [85].

Closely connected to the above-mentioned complications, researchers were able to separately observe electronic as well as structural (phononic) contributions to the phase transition and distinguish their respective time-scales. When the MIT is generated thermally, the elevated lattice temperature as well as the raised Fermi level, which is accompanied by an increased electron density in the upper bands, are responsible for the onset of the phase transition. Time-resolved pump-probe measurements show that the time needed to optically switch VO_2 from insulating to metallic using photo-induced carrier injection is in the range of 40 fs-200 fs [100; 102; 106; 109–111]. Considering this ultrafast effect, a purely structural transition is often ruled out. After this short period of time, the state of the strongly correlated electronic system is still in flux and the structual transition has not yet happened. The full transition to the metallic phase is presumably mediated by the cooling of the hot electron density via electron-phonon scattering whereby the lattice temperature is raised. This process finalizes after a time scale of $\sim$10 ps-100 ps resulting in the structural long-term phase transition [97; 107; 110].

With respect to the optical experiments conducted in the context of this thesis, the debatable details and the microscopic origin of the MIT are not crucial for understanding and discussing the results. As will be shown in Section 7.1, there is strong evidence that the laser-induced MIT utilized in this thesis is caused by a combination of an elevated nominal lattice temperatures and additional heating of the lattice by the relaxation of photo-excited carriers.

Moving on, the focus will be laid on how the electronic properties of the two phases manifest in the optical response of VO_2 nanocrystals. The special geometry of this kind of VO_2 system, fabricated by ion beam implantation, leads to a light-matter interaction that is highly advantageous for photonic research in the telecom wavelength regime.

6.2 Fabrication & Optical Properties of VO_2 Nanocrystals

There is a multitude of techniques to fabricate bulk crystals, thin films or differently shaped nanoscale VO_2, such as gas- or solution-based deposition, chemical vapor deposition, sol-gel methods, RF-sputtering, pulsed laser deposition. For more information on different methods of fabrication, see Ref. [74] and the details on the fabrication of the samples utilized in the literature referenced in this chapter. Nanostructured VO_2 systems often allow to tailor the characteristics of the light-matter interaction based on fabrication parameters. This benefit is especially pronounced in the VO_2 nanocrystals (NCs) used in this thesis.

The samples used in this thesis are fabricated using ion beam implantation in the group 'Nanoscale Functional Oxides' lead by Prof. Dr. Helmut Karl at the University of Augsburg. They consist of a dense layer of VO_2-NCs embedded just below the surface of a 500 µm thick fused silica (SiO_2) host with 10 mm × 10 mm lateral dimensions. As will be shown below, this kind of VO_2 nanocomposite features a strongly increased change of the optical properties during the MIT in the telecom wavelength regime, compared to thin films or bulk crystals. The thermal hysteresis of the phase transition will be discussed in the next section. In the following text, the fabrication and the optical properties of the VO_2-NCs are addressed.

The NCs are synthesized by sequential ion beam implantation of vanadium ($9 \cdot 10^{16}$ at/cm^2 at 100 keV implantation energy) and oxygen ($1.8 \cdot 10^{17}$ at/cm^2 at 36 keV). The doses result in a stoichiometric growth of VO_2 since the oxygen dose equals two times the vanadium dose. In the process, the implantation energies are chosen such that the V- and O-implant distribution into the substrate are both centered at ≈ 85 nm under the surface. The formation of nanocrystals happens during a 10 min rapid annealing step at 1000°C in a flowing argon atmosphere. The resulting VO_2-NCs are approximately spherical and are characterized by an average diameter of 90 nm and a similar lateral spacing (areal density $\sim 10^{10}$ cm^2). A typical transmission electron micrograph cross section of a VO_2-NC:SiO_2 sample fabricated by the group of Prof. Dr. Karl is shown in Fig. 6.2. Note the good crystallinity of the single NC shown in panel (b), which is visualized by the regular, stripe-patterend structure.

Lopez et al. first demonstrated this approach of fabricating VO_2-NCs and systematically studied how different implantation and annealing parameters affect the size and shape of the resulting nanocrystals [112]. This kind of VO_2 system offers a variety of advantages. For one, the NCs are protected from the environment so that they do not suffer from potential detriments like oxidation or hydrophilie. Furthermore, the size and shape of the NCs can be controlled during the fabrication, which offers the opportunity to tailor the optical and thermal properties. The NCs also show excellent durability and long-term stability, as will be demonstrated in Section 7.1.

In order to characterize the VO_2-NC layer in terms of optical properties, the group of

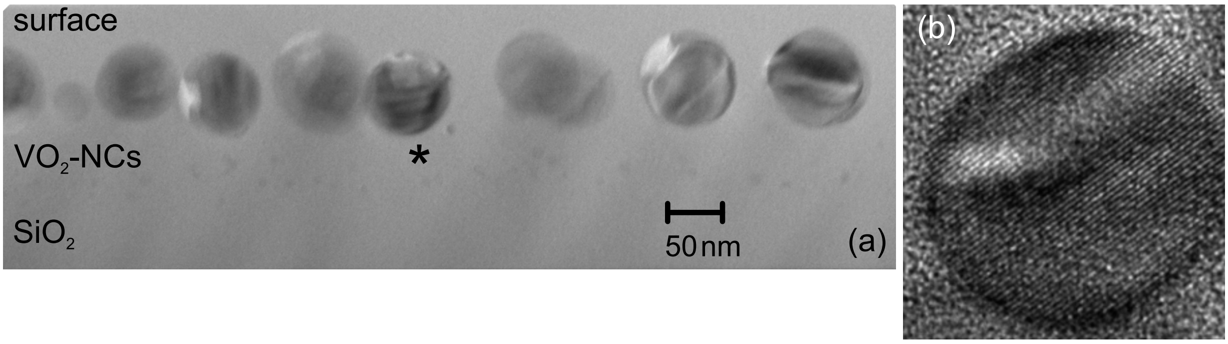

Fig. 6.2: (a) Cross-section transmission electron microscope image of ion beam sythesized VO$_2$ nanocrystals (NCs) embedded into a fused silica (SiO$_2$) matrix. Panel (b) shows a high resolution image of the NC labeled with a star in (a).

Prof. Dr. Helmut Karl performed spectral ellipsometry on a VO$_2$-NC:SiO$_2$ sample and analyzed the real and imaginary parts of the refractive index $\tilde{n} = n + ik$ of the VO$_2$-NC layer[2]. The phase of the NCs is controlled thermally. For this purpose, the samples are mounted on a temperature-controlled holder made of copper attached to Peltier elements. For fitting the measured raw data, the VO$_2$ layer was modeled using an effective medium approach (Bruggemann type, see Ref. [113]) with spherical NCs embedded into SiO$_2$, while the parameters of all other layers were determined beforehand. Note that the layer structure of the employed sample is different to the above-presented, since the SiO$_2$ host was only 200 nm thick and was deposited on a silicon substrate. To isolate the response of the VO$_2$-NC layer in the model fit, the parameters of the substrate layers (SiO$_2$+Si) were determined before the implantation. The dielectric function of VO$_2$ is included using an established model with three Lorentz oscillators [114].

The results of this procedure are depicted in Fig. 6.3(a)-(b). Close to room temperature, all VO$_2$-NCs are in the insulating phase and the spectral response is rather flat. In this state, the NC samples show optical characteristics resembling VO$_2$ films with a thickness similar to the diameter of the NCs [70]. At elevated temperatures above T_C, the MIT has been induced thermally and all NCs are in the metallic phase. The optical response is now governed by a Mie-type resonance within the metallic spherical VO$_2$-NCs. It is adequately described by Mie theory for the polarizability of spherical particles [109; 115]. Mie scattering theory is applied when electromagnetic radiation is scattered at spherical particles with a size d comparable to or smaller than the wavelength of light λ (see Ref. [3], p.145)[3].

The confined geometry of the metallic VO$_2$-NCs, wherein electrons are able to move, offers electromagnetic dipole resonances that are missing in bulk VO$_2$ specimen. Light can couple resonantly to the electron plasma within the NCs and is effectively scattered. This

---

[2] See Ref. [49], pp.155-159 for a introduction into ellipsometry. The employed unit is a Sentech SE 850 (FT-IR) together with the software Spectra-Ray3.

[3] In the present case, $d \approx 90\,\text{nm}$ and $0.5\,\mu\text{m} < \lambda < 3.5\,\mu\text{m}$. In the limits $\lambda \ll d$ or $\lambda \gg d$, the scattering is described by classical scattering (elastic collisions) or Rayleigh scattering theory, respectively.

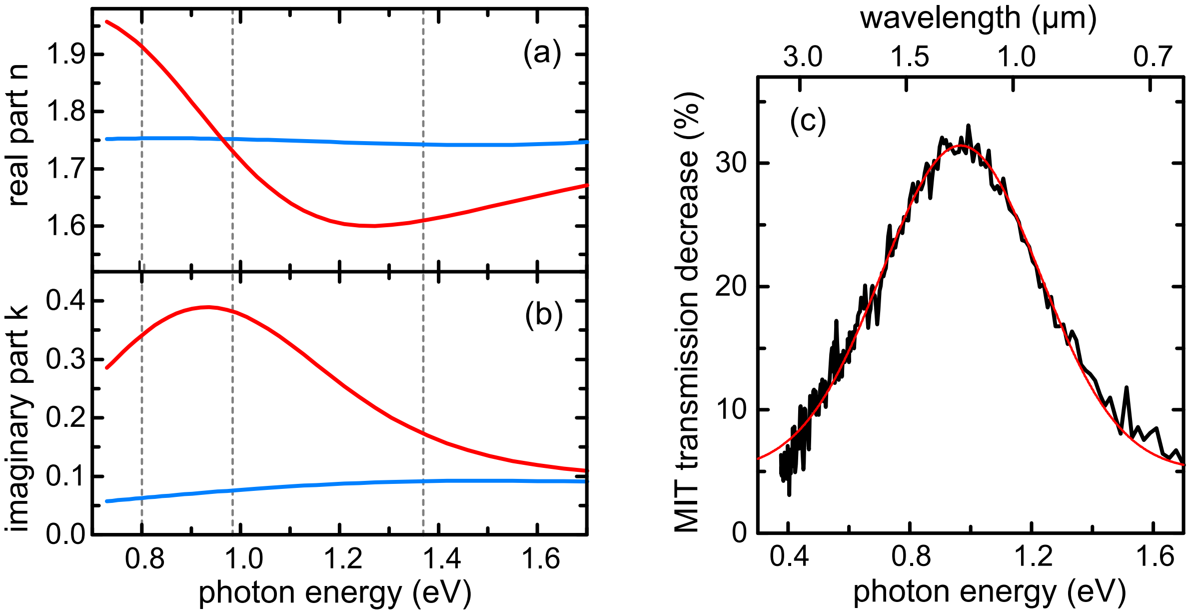

Fig. 6.3: (a) Real and (b) imaginary part of the refractive index of VO_2-NCs in SiO_2 as determined by spectral ellipsometry for different sample temperatures. Blue: 28°C (insulating). Red: 100°C (metallic). The vertical dashed lines indicate the photon energies used for the demonstration of photonic (0.8 eV) and plasmonic elements (0.8 eV, 0.98 eV and 1.37 eV). (c) Relative decrease of the optical transmissivity related to the phase transition from insulating to metallic VO_2-NCs. The red line is a Gaussian fit to the data.

resonance results in a strongly increased imaginary part k and a dispersive signature in the real part n, in agreement with the Kramers-Kronig-relation under the assumption of an absorptive resonance (see Ref. [3], p.88).

For further characterization, spectrally resolved normal incidence transmission measurements are performed by the author using an ellipsometer (VASE model by J.A. Woollam Co.). The strength of the transmitted signal S through the sample is recorded for temperatures of 15°C and 100°C, i.e. for insulating and metallic VO_2-NCs. Fig. 6.3(c) displays the results for the spectrally resolved relative change of the transmission during the MIT, which is calculated as $1 - S_{\mathrm{met}}/S_{\mathrm{iso}}$. Due to the increased imaginary part k, the transmission is reduced by $> 30\,\%$ during the MIT[4]. Considering an effective interaction length of $< 50\,\mathrm{nm}$ in the partly filled VO_2-NC layer, this MIT-induced change of the light-matter interaction is remarkably strong. The data in Fig. 6.3(c) points towards a MIT-induced increase of the absorption coefficient by $\sim 7 \cdot 10^4\,\mathrm{cm}^{-1}$ at the center of the resonance.

The spectrum of the transmission change is well described by a Gaussian centered at 0.97 eV, reflecting the Mie-type resonance in the NCs. A similar shape has been found before by a different group, also in ion-beam implanted VO_2-NCs [116]. Since the spectral position

---

[4] The signal reduction can mainly be attributed to the increased absorption. Considering the ellipsometry data, the change in the real part of the refractive index leads to $< 2\,\%$ change in the reflectivity of the VO_2-NC layer.

of the resonance in the metallic NCs depends on their diameter, it can be tailored during the implantation of the NCs using different annealing parameters. This way, the change of the complex refractive index of the VO_2-NC samples can be adapted to applications in the visible (Ref. [115]) or near-infrared (Ref. [116], this work) wavelength regime. As a general trend, the resonance shifts to short wavelength for smaller NC diameter. Note that in the experiments presented here, and in the remainder of the thesis, an ensemble of $\sim 10^4$ NCs is analyzed simultaneously. The optical signals, for example the data in Fig. 6.3(c), include the combined answer of NCs with different diameter. However, TEM images and the results presented in the next section point towards a rather uniform distribution of NC's diameters in the samples.

It should be noted that the samples investigated in the various subsections of this thesis slightly differ in processing parameters and the resulting average NC diameter. For example, the ellipsometry data was taken with a different sample than the data of the transmission decrease. However, the variations are minor, and the effect on any of the main conclusions drawn below is negligible. In numbers, the central position of the MIT-induced transmission decrease shifts by less than 50 meV when comparing different samples. This shift is $< 10\,\%$ of the width (FWHM) of the resonance shown in Fig. 6.3(c).

In the next section, the thermally induced MIT and the hysteresis in VO_2-NC samples will be analyzed.

6.3 Thermally Induced Phase Transition & Hysteresis in VO_2 Nanocrystals

Since its first discovery, it was known that the first order phase transition in VO_2 features a hysteresis. The term hysteresis refers to the fact that the critical temperature for the insulator-to-metal phase transition upon heating is higher compared to the backwards metal-to-insulator transition upon cooling. First utilizations of this effect were reported in the early 1970s in the context of optical or holographic storage [117; 118]. In bulk samples, the difference between the critial temperatures is in the order of 1 K [18]. As soon as the size of the VO_2 system is restricted to nanoscopic length scales in one or more dimensions, the width of the hysteresis approaches 10 K for thin films or even 30 K-50 K in stronger confined geometries [119]. This section provides a study of the critical temperatures of the MIT in the VO_2-NCs used in this thesis, which show a particularly large thermal hysteresis [87]. The reasons for this behavior are discussed below, but first, the physical background of this phenomenon is briefly outlined.

From a fundamental, thermodynamic point of view, the transition between two solid state phases of VO_2 is a first order phase transition. It may be triggered by a parameter, such as the lattice temperature, that changes the Gibbs free energy of both phases. The critical temperature T_C marks the temperature at which both phases feature the same minimal free energy. In the case of VO_2, the insulating phase has the lowest free energy for $T < T_C$. As the temperature is increased to $T > T_C$, the minimum is now in the metallic phase and the system becomes metallic.

The hysteresis arises because of an energy barrier between the two phases. Additional energy has to be added to (or substracted from) the system in order to move it to the neighboring potential minimum, i.e. to induce the phase transition. This energetic barrier can be overcome by either changing the energy of the system sufficiently (stronger heating/cooling) or by fluctuations which induce a nucleation. In real space, the phase transition starts at a point in the medium, where the barrier is somewhat smaller due to a modification of the potentials by impurities, roughness, grain boundaries or strain. These points are called nucleation sites. Everyday examples for this phenomenon are the boiling of liquid water that starts at dirt particles (e.g. salt) at the bottom of a pot, or a lake that begins to freeze at rocks or branches. When a parameter of the system is driven across the critical point, but the phase transition has not yet happened, the state of the system is called superheated or supercooled. Again, H_2O gives good examples: If water is boiled in a microwave in a cup with very smooth surfaces, it might be superheated and stay liquid at temperatures above 100°C (which is why one is supposed to put nucleation sites, e.g. the rough surface of a wooden spoon, into the cup). Likewise, supercooled water can rapidly be turned into ice by stirring or shaking it.

The focus of the characterization of the VO_2-NCs is now laid on the thermally induced phase transition and its hysteresis. In order to monitor the momentary phase of the NCs, the normal incidence transmission of a low-power cw (continuous wave) laser at 0.8 eV photon energy ($\lambda = 1.55\,\mu m$) through the sample is measured using an InGaAs photodiode and lock-in detection. Considering a laser spot diameter of $\approx 100\,\mu m$ on the sample surface, an ensemble of roughly 10^4 NCs is probed. For the purpose of defining the lattice temperature, the sample is mounted on a temperature-controlled holder made of copper attached to Peltier elements.

Fig. 6.4 displays the probe transmission for increasing and decreasing sample temperatures. All data is normalized to the signal strength at the start of the heating/cooling cycle at 5°C. Upon heating the sample, the optical transmission is nearly unchanged until a sharp drop occurs at a critical temperature of $T_C \approx 80°C$. This feature, which is indicative of the thermally induced transition from insulating to metallic VO_2, is followed by a plateau at a relative transmission of $\approx 78\,\%$ in agreement with the MIT-induced transmission change seen at 0.8 eV in Fig. 6.3(c). When the sample is subsequently cooled down, a pronounced thermal hysteresis with a supercooled metallic state persistent down to practically room temperature is seen. More specifically, the reverse phase transition from metallic to insulating VO_2 sets in at a temperature of $\approx 25°C$, leading to a width of the hysteresis of $\Delta T \approx 55°C$-$60°C$.

The width of the hysteresis clearly exceeds that of other nanoscale VO_2 systems reported so far [119–121]. This substantial bistability can mainly be attributed to two effects:

(i) The NCs have a small volume and good crystal quality which, in combination, leads to a small probability of finding a nucleation site (impurity, vacancy, grain boundary) in a

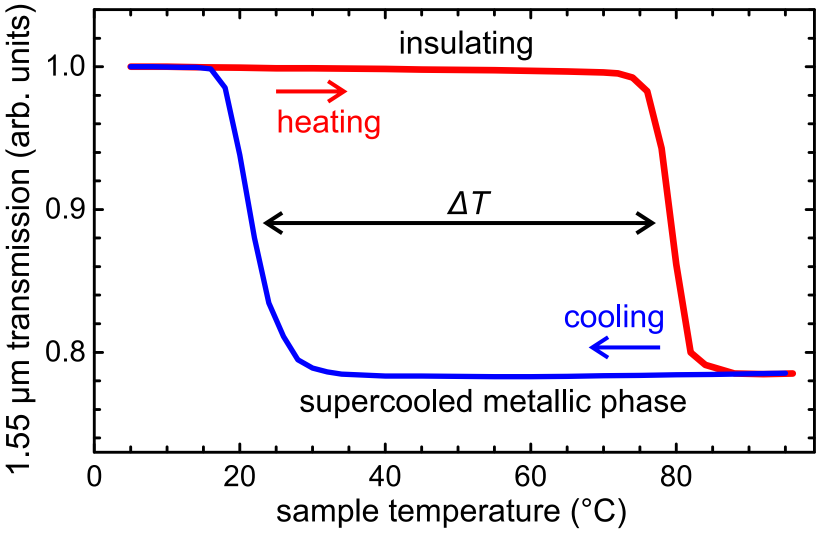

Fig. 6.4: Thermaly induced MIT and hysteresis recorded by tracking the $1.55\,\mu m$ probe transmission for increasing (red) and decreasing (blue) sample temperatures. The MIT from insulating to metallic VO_2 is triggered at a critical temperature of $T_C \approx 80°C$. Upon cooling, a supercooled metallic phase persists to room temperature.

NC. In other words, the NCs have a single-domain character and the related absence of nucleation sites hampers the structural phase transition. There are only few fluctuations in the potential energies that help to overcome the energetic barrier between the phases. As a results, the critical temperature of the transition from insulating to metallic VO_2 is raised. The back-switching temperature upon cooling the sample is lowered because of the same reasons. Studies of the dependence of the thermal hysteresis on size [115; 119; 121; 122] and crystallinity [120; 122] of nanoscale VO_2 support this interpretation. As a general trend summarizing these studies, it can be concluded that smaller and 'cleaner' VO_2 systems show an increased T_C and a broader hysteresis. In addition, the results of the influence of argon ion bombardment on the critical temperatures, presented in the next section, are successfully explained in this context and support this interpretation.

(ii) Embedding VO_2-NCs into a fused silica host induces local strain fields owing to the different thermal expansion coefficients of VO_2 and SiO_2. It has been shown that such a matrix - and internal or external stress in general - changes the critical temperatures significantly [93; 95; 123; 124]. This effect is mainly attributed to a modification of the unit cell dimensions and, consequently, the V-V dimerization along the rutile c_R-axis [93; 124]. Explicit connections between the length of this axis, which is modified by external stress, and the transition temperatures were found [125; 126]. In the context of the discussion of Gibbs free energy made above, stress increases the energetic barrier between the phases.

In the next step, the thermal hysteresis is verified for the entire spectral region shown in Fig. 6.3(c) by recording transmission spectra for increasing and decreasing temperatures (data not shown). It is found that the width ΔT does not vary for different probe photon energies, as expected.

The thermal hysteresis furthermore allows to qualitatively rate the distribution of NC sizes in the sample. A general trend observed in literature is that a smaller particle size leads to higher critical temperatures (and vice versa) for the reasons given above [115; 119; 121; 122]. Thus, the steep decline of the signal near 80°C points towards a rather uniform distribution of the diameters and crystallinity of the NCs.

The broad thermal hysteresis of the VO_2-NCs in SiO_2 is a crucial prerequisite for the demonstration of reconfigurable photonic elements discussed in Chapter 7. As will be shown, it allows to switch the NCs into a long-term stable supercooled metallic phase. In the next section, a second requirement for the creation of pre-defined photonic elements is introduced, namely the controlled modification or even deactivation of the phase transition.

6.4 Engineering of the Critical Temperatures Using Argon Ion Bombardment

One intriguing way to utilize the dielectric contrast between the two phases of the VO_2-NCs is the generation of spatial patterns of insulating and metallic NCs, which function as photonic elements. In the approach published by Zimmer et al. [87], the MIT is deactivated in pre-selected spatial areas of the sample by irradiating the NCs with argon ions. The aim of this section is to introduce this technique and clarify the mechanisms behind it. To this end, a series of samples with different argon doses ranging from zero to a dose at which the MIT is known to be deactivated is investigated. It was not investigated so far, how smaller argon allow for the tuning the critical temperatures.

The motivation behind this research is to be able to adapt the thermal properties of VO_2 specimen to certain applications. For example, smart thermochromic window coatings based on VO_2 woudl benefit from moving T_C even closer to ambient temperatures. A review of the efforts made in this direction can be found in Ref. [74].

The effects of nucleation sites and energetic barriers discussed above can be utilized to substantially change the critical temperatures and the hysteresis of the MIT. Different ways of achiving this have been demonstrated: For one, the external stress imposed on the VO_2 lattice can be tailored during the fabrication by choosing different substrates [125–127]. In a different approach, $V_{1-x}X_xO_2$ materials are fabricated, where the dopant X may be tungsten [70], chromium [96] or titanium [112], for example. Karl et al. demonstrated the doping of VO_2-NCs with tungsten and molybdenum [78; 128]. Furthermore, bombardment of as-grown VO_2 with ions such as protons [129], caesium [130] or, most prominently, argon ion was demonstrated and utilized for application-driven research [87; 127; 130].

The use of the nobel gas argon is favourable because it is not incorporated in the VO_2 lattice structure, thus the VO_2-NCs are not doped [130]. Argon ion bombardment of VO_2-NCs was employed by the group of Prof. Dr. Hubert J. Krenner from the University of Augsburg for the creation of thermochromic diffraction gratings (see Ref. [87] and Section 7.2). It was demonstrated that the phase transition of the NCs is inhibited by exposing them to a sufficiently high dose of Ar^+ ions ($7 \cdot 10^{14}$ cm^{-2}) [87]. The deactivation of the MIT is due to the introduction of site defects and vacancies, caused by displacement collissions of Ar ions with V and O atoms, which result in a massive deformation of the VO_2 lattice structure [78]. It was shown that amorphous VO_2 shows no MIT [127; 131]. All such processed NCs will remain insulating independent of any thermal or optical excitation. The demonstration of switchable plasmonic grating couplers, presented in Chapter 9, is also based on this deactivation of the MIT.

The purpose of the experiments presented in this section is an analysis of the effects of increasing doses of argon ion bombardment on the MIT in VO_2-NCs. The samples were processed by the groups of Helmut Karl and Hubert Krenner at the University of Augsburg.

Apart from the irradiation with different argon doses, which happens after the fabrication, the samples are fabricated with identical parameters. The experimental approach is similar to the one used to record the thermal hysteresis in Fig. 6.4: The transmission of a cw laser at 0.8 eV photon energy is measured while the sample temperature is varied. This way, any change to the optical properties of the VO_2-NCs, caused by a thermally induced phase transition of NCs, is monitored. Note that the sample area illuminated by the laser contains an ensemble of $\sim 10^4$ individual non-interacting NCs.

It is evident from the results of this examination, presented in Fig. 6.5, that the overall shape of the thermal hysteresis is strongly altered by the argon bombardment. The different samples will be referred to as 'Ar-*argon dose (in* 10^{14} cm^{-2})', cf. the legend in the figure.

The black line in Fig. 6.5 shows the thermal hysteresis of the as-grown VO_2-NC sample (Ar-0) that was not exposed to argon ions. A comparison with the data in Fig. 6.4 reveals an inferior NC quality in the sample Ar-0 compared to the sample studied above. The hysteresis is narrower, and the temperature range in which the phase transitions happen is broader, i.e. the slope of the transmission drop is smaller. The latter observation points towards a broader distribution of critical temperatures of the individual NCs in the probed ensemble, most likely due to a broader distribution of NC sizes or a larger number of somewhat 'dirty' NCs (lattice faults, defects). Furthermore, the mean size of the NCs is probably larger. However, since all samples in this series are fabricated identically, the slightly reduced NC quality does not impede the goal of the current examination.

The effects of argon ion bombardment are well elucidated by comparing the data for the samples Ar-0 , Ar-2 and Ar-6.5. In order to follow the analysis presented below, the reader may recall the discussion of the broad thermal hysteresis of VO_2-NCs given above.

(i) The distribution of critical temperatures smears out drastically if the argon dose is increased, up to a point where a steady almost linear transmission decrease with increasing temperature is seen. This behavior is explained by the increasing number of NCs that are affected by the argon ions and lose their good crystallinity and single-domain character. It is known that T_C in nanoscale VO_2 systems is strongly dependent on the lattice quality and shape of individual units. With increasing argon dose, more NCs are modified such that the critical temperature of those NCs is reduced, respectively increased for the backwards phase transition metal→insulator.

(ii) The maximum reduction of the transmission at high temperatures $T > 90°C$ decreases with increasing argon dose. A growing number of NCs is affected evermore strongly, up to a point where the MIT is deactivated. Consequently, there are less metallic NCs in the probed ensemble that reduce the transmission of the probe laser at high temperatures, regardless of the sample temperature.

The data for the samples Ar-11 and Ar-20 reveal an almost complete deactivation of the MIT of all probed NCs, cf. the upper panel in Fig. 6.5. In order to rule out the influence of laser power noise and thermal fluctuations, the data presented here is averaged over

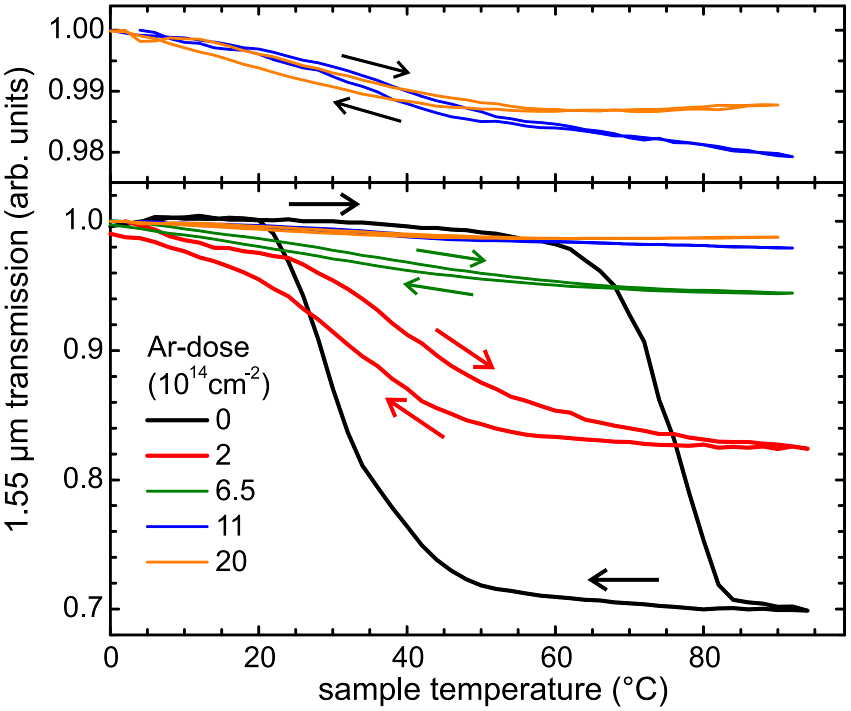

Fig. 6.5: Thermally induced MIT and hysteresis of VO_2-NC samples exposed to argon ion bombardment recorded by tracking the 1.55 µm probe transmission for increasing and decreasing sample temperature (indicated by arrows). All data is normalized to the transmission at the start of the heating/cooling cycle.

five runs trough the heating/cooling cycle. The remaining difference in the transmission levels for heating and cooling runs is indeed linked to a small hysteresis of the MIT of a small remaining number of unaffected NCs. Note that the process of selective deactivation described in Ref. [87] and Section 7.2 is performed with an argon dose of $70 \cdot 10^{14}\,\mathrm{cm}^{-2}$, which is 3.5 times the dose of sample Ar-20 resulting in only 1% transmission decrease.

To sum up, the critical temperatures of the MIT in the probed ensemble of VO_2-NCs can be altered using argon implantation. At the same time, a fraction of the NCs becomes 'deactivated' and cannot undergo the MIT anymore. Both effects increase with increasing argon dose. The deactivation of the MIT is useful tool for photonic applications, see [87; 130] and Chapter 9. Future studies could benefit from finer increments of the argon dose and/or the comparison of different dopants. The data in the upper panel of Fig. 6.5 suggests that the critical temperature of some NCs is shifted below 0°C. A wider temperature range has to be investigated to clarify this issue. Finally, isolating single NCs would help to eradicate the complication of analyzing the optical response of a huge ensemble of NCs.

Tuning only the thermal properties using argon ions, without deactivating the MIT in a part of the NCs, does not seem feasable. Other dopants like tungsten seem to be more suited for this purpose, since the critical temperature of the probed NC ensemble is shifted as a whole, without deactivation of the MIT [128; 132].

Chapter 7

Optically Imprinted Reconfigurable Photonic Elements

The active, fast and deterministic modulation of light is an essential building block of photonics. Numerous means of imposing a control mechanism on the propagation of light are of general interest for photonic applications. In this context, phase change materials are subject to extensive research, since they offer strongly nonlinear modifications of the dielectric, structural or electronic properties of a material. Modern everyday applications of phase change materials are rewritable optical discs (CD, DVD, Blu-ray) and novel solid state memory chips [133].

Vanadium dioxide (VO_2) is of special interest because of the metal-insulator phase transition (MIT) that occurs at near-ambiant temperatures. More specifically, the light-matter interaction (absorption, reflection, amplitude and phase of transmission) changes drastically during the MIT, since the two phases feature a different complex dielectric function. The marked change of the optical properties during the MIT is a promising tool for photonic applications. Several photonic elements employing this control mechanism have been demonstrated or proposed, comprising lenses [134], polarization optics [130; 135; 136] or photonic modulators [137–140]. The concepts and results presented in this chapter add to this field of research by addressing the potential use of an optically generated spatial dielectric contrast of insulating and metallic VO_2 nanocrystals for novel photonic applications.

Employing the VO_2-NCs studied in this thesis, it was demonstrated that a spatial dielectric contrast between insulating and metallic areas defines thermochromic diffraction gratings [87]. In this approach, a site-selective bombardment with argon ion (see Section 6.4) inhibits the MIT in sub-ensembles of the sample. The resulting dielectric contrast for temperatures below and above T_C allows for the implementation of switchable, large-contrast diffraction gratings at telecom wavelength. Section 7.2 gives a summary of the physics and fabrication of VO_2-based diffraction gratings. These structures are also utilized for the demonstration of switchable plasmonic grating couplers, presented in Chapter 9 of this thesis.

As has been pointed out in the previous chapter, VO_2 offers a variety of ways to control the MIT via thermal, electronic, optical or mechanic excitation. In the following section, it is investigated how the MIT in VO_2-NCs can be induced optically, and it is analyzed how the broad bistability of the phase transition may be utilized in this context. It is shown that the combination of thermal and optical excitation allows for the creation of a persistently supercooled metallic phase. The long-term stability and the ability to perform highly repetitive, non-destructive switching are explicitly verified. Both properties are decisive for the functionality and lifetime of potential devices for switching or memory applications.

Using optical means to trigger the MIT offers the possibility to selectively switch NCs in chosen areas of the sample into the metallic phase. Thereby, spatial patterns of insulating and metallic NCs are created optically with more flexibility compared to the selective deactivation mentioned above. Figuratively speaking, a sample of VO_2-NCs is a blank canvas that can be painted on using focused laser light as a brush. In this picture, a two-color image can be created, represented by the dielectric contrast of insulating and metallic VO_2.

The goal of the work presented in Section 7.3 is to optically imprint dielectric patterns into an otherwise unstructured sample. Utilizing spatially a selective optical excitation, photonic micropatterns of insulating and metallic NCs are imprinted which serve as photonic elements for telecom radiation. As fundamental paradigms, diffraction gratings and optical zone plates are demonstrated. While such photonic elements are long-term stable at slightly elevated temperatures, they can be fully erased in a non-destructive fashion by cooling the structures to below room temperature.

7.1 Optically Induced Phase Transition & Hysteresis

It is now studied how the phase transition can be induced optically and how the thermal hysteresis translates to this optical excitation. The specimen investigated in this context are identical to the samples used for the experiments presented in the previous chapter. They are again mounted on a temperature controlled holder in order to control the overall lattice temperature.

An all-optical approach is used to induce and monitor the MIT of the VO_2-NC nanocomposite, see Fig. 7.1. A cw 532 nm pump laser is focused onto the sample surface to a $\approx 100\,\mu$m spot diameter (FWHM). It mainly deposits heat in order to raise the lattice temperature T above the critical temperature T_C and, thereby, switches the illuminated NCs to the metallic phase. The details of this optical excitation are addressed below. The momentary phase of the VO_2-NCs is probed with a focused low-power cw 1.55 µm laser (spot diameter $\approx 45\,\mu$m FWHM). Specifically, the transmitted probe radiation is measured using an InGaAs photodiode and lock-in detection referenced to the laser output. A small

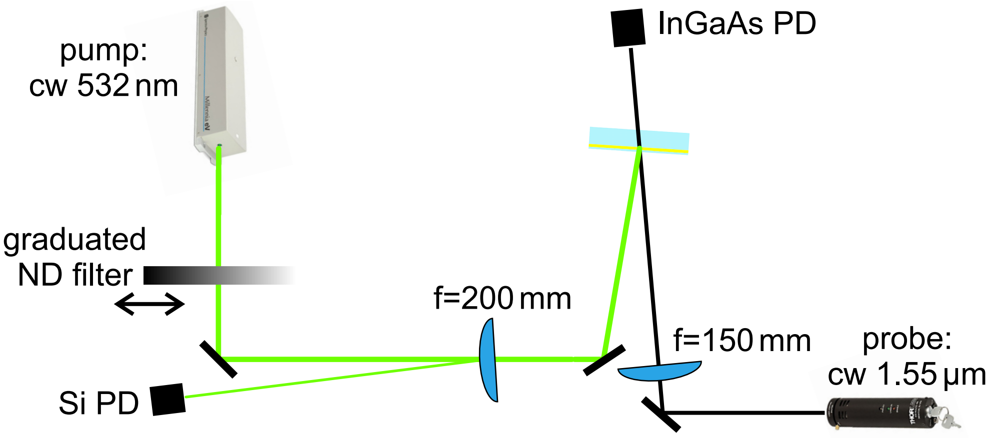

Fig. 7.1: Scheme of the experimental setup used for the optical generation of the MIT in VO_2-NCs. The pump and probe lasers are a SpectraPhysics Millennia and a Thorlabs LDM1550 diode laser, respectively. The $\lambda = 1.55\,\mu m$ probe transmission through the sample is measured using InGaAs photodiode (PD) and lock-in detection, while a $\lambda = 532\,nm$ pump laser induced the phase transition. To adjust the pump power, which is measured by a silicon PD, a graduated neutral density filter (ND) filter is used.

reflected fraction of the pump laser is collected in a silicon photodiode and measured at the lock-in amplifier. This is done in order to simultaneously monitor the momentary pump irradiance and the probe transmission. The pump power is adjusted with a linear graduated neutral density filter attached to a translation stage.

Since the spatial distribution of the pump irradiance on the sample surface is approximately Gaussian, the heat deposition in the illuminated area is non-uniform. Although it is expected to roughly follow the Gaussian pattern, the details and temporal dynamics of the heat dissipation in the sample plane into the non-illuminated areas are non-trivial. In order to rule out potentially detrimental effects, two steps are performed: For one, the probe spot diameter is chosen to be less than half of the pump spot diameter, whereby the probed area is illuminated with nearly homogeneous pump irradiance. The actual spot profiles and positions are determined beforehand using a rotating slit beam profiler. Secondly, the formation of a thermal equilibrium is ensured after each modification of the pump irradiance by waiting until the probe signal has settled to a constant value (~2-3 s).

Fig. 7.2(a) displays the relative probe transmission for various combinations of sample temperatures and pump irradiances. All data points are normalized to the unpumped signal strength. The sharp drop of the signals for increasing pump irradiance reflects the optically induced MIT caused by the local temperature increase in the pumped area. At a sample temperature of $T = 15°C$, a broad and fully reversible hysteresis is found that resembles the thermal hysteresis shown Fig. 7.2(b). When the procedure is repeated for elevated sample temperatures, the irradiance needed to induce the MIT is reduced. This fact indicates that a combination of thermal and optical excitation is responsible for the MIT. A more detailed

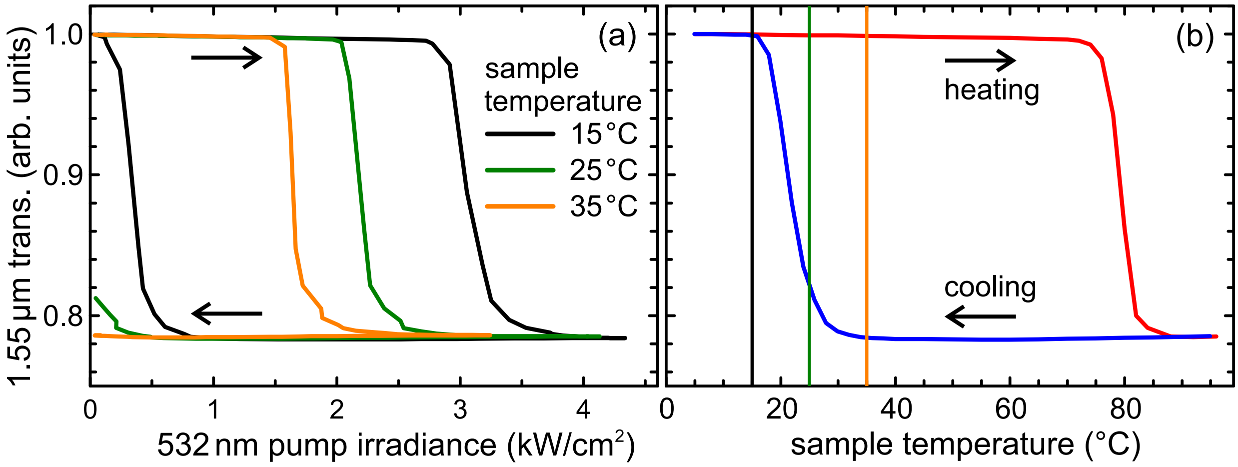

Fig. 7.2: (a) Optically induced insulator-to-metal phase transition and hysteresis recorded by tracking the 1.55 µm probe transmission for different sample temperatures. Arrows indicate increasing and decreasing pump powers. (b) Thermally induced MIT and hysteresis for increasing (red) and decreasing (blue) sample temperatures (note that data in this panel is identical to Fig. 6.4). The vertical lines indicate the temperatures used during the optical excitation shown in panel (a).

discussion of this issue is given later on. Remarkably, for elevated lattice temperatures slightly above ambient temperatures, the metallic phase persists in the entire ensemble of NCs without any further illumination. More specifically, this behavior sets in when the lattice temperature is raised above a temperature at which the reverse phase transition metal→insulator sets in ($T \approx 35$°C). The pronounced hysteresis of the MIT, together with the elevated nominal lattice temperature, now inhibits the NCs from undergoing the reverse MIT. The NCs remain in the supercooled metallic phase without additional optical excitation. In essence, the range of effective sample temperatures in the illuminated area is restricted to the right side of the vertical lines in Fig. 7.2(b).

The approach to optically define supercooled VO_2-NCs opens up the opportunity to almost arbitrarily create planar photonic micropatterns in an otherwise unstructured sample. In the experiments presented here, local control of the MIT is already demonstrated, albeit with a spatial resolution of only ≈ 100 µm. Using a focused pump laser, only illuminated NCs are switched to the metallic phase while the rest of the sample remains insulating. Before moving on to the demonstration of photonic elements, some important features of the optically generated MIT in the VO_2-NC:SiO_2 samples are discussed.

Mechanism Behind the Optically Induced MIT

The mechanism behind the optically induced MIT is now briefly discussed. The question arises to what extent the phase transition is triggered by the optical injection of carriers, or if it can be regarded as purely thermal. To clarify this aspect, time-resolved pump-probe studies are performed[1]. Specifically, the output of a regenerative amplifier (RegA) at 810 nm wavelength), emitting 50 fs pulses at a repetition rate of 250 kHz, is used. As a probe light source, the output of the OPA tuned to 1.23 µm is used. The experimental setup follows a basic pump-probe scheme with a mechanical delay stage and two lenses that independently focus pump and probe beams onto the sample, similar to Fig. 4.1.

The dynamical temporal response gives hints towards the contributions of electronic and structural degrees of freedom. Its timescales are largely consistent with recently reported findings on VO_2 thin films and point to only minor influence of the nanoscale structure on the ultrafast dynamics of the MIT (see Section 6.1 and, e.g., [102; 106; 107]). Contributions to the pump-induced signal on the time-scales of electronic effects (100 fs to 100 ps) never exceed a strength of 2%.

In addition, the experiments presented above in Fig. 7.2 are repeated with the pulsed pump and probe laser sources. The time-averaged irradiance level required to induce the MIT with this source is $\approx 4.4\,\mathrm{kW/cm^2}$ at 20°C lattice temperature. This value is very similar to the one seen in the data in Fig. 7.2, even though the peak irradiance of the pulsed pump light is increased by a factor of $(50\,\mathrm{fs} \cdot 250\,\mathrm{kHz})^{-1} = 8 \cdot 10^7$ when compared to cw excitation. Furthermore, the required time-averaged irradiance does not change significantly for different time-delays, which cover the regime of electronic and thermal effects.

In conclusion, the observations made above leads to the assumption that the phase transition is effectively thermally triggered in both situations. The optically induced MIT can be considered as originating from a rapid laser-induced heating of the VO_2-NCs throughout all experiments presented in this chapter. The origin of the phase transition can be briefly summarized as follows: The absorption of photons optically excites a hot electron plasma, which cools down via electron-phonon scattering. Thereby, the lattice temperature T is raised. At a certain photon density, these processes subsequently combine to raise $T > T_C$ and the structural transition sets in.

Preparing a Long-Term Stable Supercooled Metallic State

The long-time stability of the optically generated supercooled metallic phase is explicitly verified at a lattice temperature of $T = 40°\mathrm{C}$, using the experimental configuration shown in Fig. 7.1. For this purpose, the duration of the cw 532 nm pump illumination is precisely

---

[1] Note that no data is presented in this subsection in order to restrict the length this discussion. The details of the temporal dynamics are not relevant for understanding the main results of the following chapters.

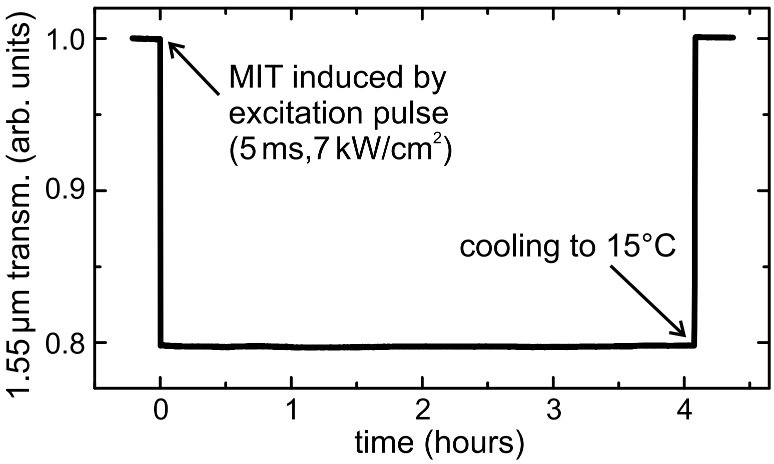

Fig. 7.3: Long-term stability of the supercooled metallic phase characterized by the decreased probe transmission after inducing the MIT at time zero with a short optical excitation. The nominal sample temperature is kept at 40 °C until the sample is cooled after several hours to reset the VO_2-NCs to the insulating phase.

defined by a fast mechanical shutter. The MIT is now generated with a single optical excitation event while monitoring the phase of the NCs using the cw 1.55 µm probe tranmission.

The results of this procedure are shown in Fig. 7.3. At an arbitrary time zero, the pump excitation is present for 5 ms. It switches the NCs to the metallic phase, which is evident from the transmission drop. The supercooled metallic state persists for several hours without any noticeable relaxation. However, cooling the sample to $T = 15°C$ immediately induces the reverse MIT and resets all NCs to the initital, insulating state. This finding is utilized for the creation of reconfigurable photonic devices presented later in Section 7.3. Furthermore, it opens up the possibility to use nanoscale VO_2 and the large bistability of the MIT for potential applications in all-optical memory devices [83; 84; 86].

Repetitive Switching

The present optical approach also permits to explore the limits of highly repetitive switching of the MIT. Most applications aiming to utilize the phase transition in VO_2 require a non-destructive, reversal MIT in order to provide a long lifetime of potential devices. However, bulk and thin-film VO_2 specimen often suffer structural disintegration when repetitively undergoing the MIT. This effect is related to the $\sim 1\,\%$ change of the unit cell dimensions during the phase transition [90; 92; 141]. The crystal quality of the single-domain VO_2-NCs and the embedment into a fused silica matrix resolve this detrimental limitation [124]. Simply put, the substrate is able to absorb the MIT-induced strain and allows the NCs to expand their volume.

To verify this robustness, a 1 Hz on/off modulation is applied to the cw 532 nm pump laser using the mechanical shutter (500 µs open, 500 µs closed). The lattice temperature is

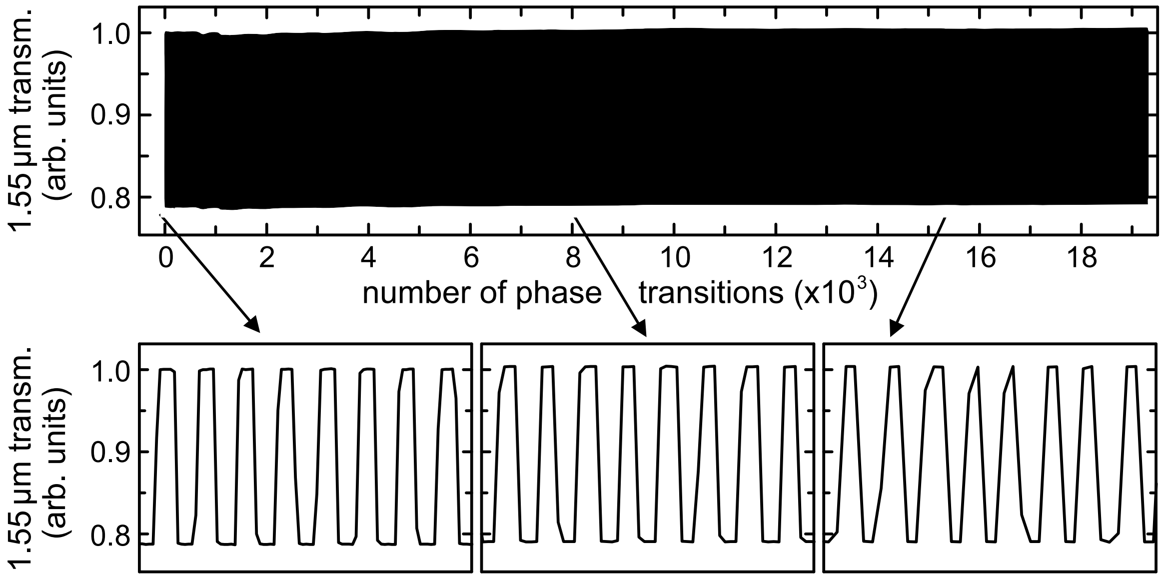

Fig. 7.4: Highly repetitive cycling through the phase transition. The probe transmission is monitored while the VO$_2$-NCs undergo through the forward and reverse phase transition induces by a 1 Hz on/off modulation of the pump laser. The lower panels are zooms into the data showing the alternating transmission levels that reflect the two phases.

kept at 2°C such that the NCs quickly recover to the insulating phase everytime the pump laser is blocked. The transmission of the cw 1.55 µm probe laser reveals how the phase of the VO$_2$-NCs follows this pump modulation. As is obvious from the data presented in Fig. 7.4, no evidence of structural degradation is found, even after $> 10^4$ cycles between insulating and metallic phases. In addition to this promising result, the fact that the VO$_2$-NCs are buried in fused silica drastically reduces the interaction with any atmospheric influences, such as oxidation, the contamination of the surface or the introduction of defect. Taken together, the VO$_2$-NCs:SiO$_2$ material system offers the possibility to create durable devices, which is beneficial for lab-related purposes and potential applications alike.

7.2 Fundamentals of VO$_2$-Based Diffraction Gratings

In order to create photonic structures that alter the propagation of light in amplitude, phase or direction, the dielectric contrast between the two phases of VO$_2$ is utilized in the following demonstrations of photonic elements. The principles of steering light using diffraction are outlined briefly in the following text. This knowledge is also crucial to understand the working principle of zone plates which will be explained in detail in the next section. Afterwards, the fabrication and working principles of VO$_2$-based diffraction gratings are presented.

A diffraction grating is an optical element capable of altering the direction of propagation of light. Furthermore, its inherent dispersive properties lead to a spatial separation of spectral components of the incident light. This feature is extensively used for applications like spectrometers, tunable diode lasers, laser pulse compression and for optomechanical components in experimental setups.

The following discussion is based on the wave character of light and, for simplicity, assumes plane waves. Following Huygen's principle, every point of the wave front is a source of elementary spherical waves and the propagation of a wave is determined by the superposition of all elementary waves (interference). Whenever a light wave interacts with an obstacle or aperture of a size comparable to the wavelength, such that parts of the wave are blocked or reflected, further propagation of the wave is altered. The angular distribution of the directions of propagation will increase and, in other words, the light beam becomes more divergent.

In order to utilize the effect of diffraction in a deterministic manner and control the propagation of light beams, periodically structured objects are employed, such that the widened distributions of light interfere and create the desired wave front[2]. A prominent example of this principle is the famous (Young's) double slit experiment: the superposition/interference of waves passing through two adjacent slits results in a irradiance pattern that is distinctly different from the subsequent addition of the two single-slit patterns.

A diffraction grating is composed of a row of slits of width a that are arranged at equal distance p, which alternate in being opaque and transparent. The interference of all spherical waves originating from the transparent slits results in an intensity pattern corresponding to new beams, which propagate under an angle θ with respect to the direction of propagation of the incoming light wave. Mathematically, the interference is determined by the path length difference from different slits to a point in the far field. Only at certain angles of diffraction, constructive interference leads to maxima in the intensity. Solving the Fraunhofer's integrals, the angle of the m-th order diffraction can be calculated to be (see Ref. [3], p.132)

$$\theta_m = \arcsin\left(\frac{m\lambda}{p}\right) . \tag{7.1}$$

Pre-Defined Thermochromic Diffraction Gratings based on VO_2

The idea of creating diffraction gratings based on the different refractive index of insulating and metallic VO_2 has been demonstrated by the group of Prof. Dr. Hubert J. Krenner from the University of Augsburg [87]. Alternating stripes of insulating and metallic VO_2-NCs are created using site-selective argon bombardment of otherwise unstructured samples. A short overview of the processing of the samples is given next. For details on the physical background of the deactivation of the MIT, the reader may refer to Section 6.4, which

---

[2] It is a delicate issue to distinguish the processes of diffraction and interference (or superpositon of light waves). Even the wave front shape behind a single slit with a width of two times the wavelength of light is determined by the interference of elementary waves originating from points within the slit.

presents an examination of the effect of argon bombardment on the phase transition and hysteresis of VO_2-NCs.

In order to create VO_2-based diffracation gratings for the telecom wavelength regime, VO_2-NC samples are processed using a method called selective deactivation. Following Fig. 7.5 and Ref. [87], this method is now briefly explained: (1) A 120 nm thick chromium mask, defined by optical lithography and a lift-off process, is deposited on top of a homogeneous layer of VO_2-NCs. (2) The mask protects stripe-patterned areas of NCs from the Ar^+ ion implantation ($7 \cdot 10^{15} \frac{\mathrm{at}}{\mathrm{cm}^2}$ at 80 keV). The argon ion bombardment introduces defects into the NCs which inhibit the MIT. As a result, the unprotected NCs will not switch into the metallic phase regardless of any thermal or optical excitation. (3) The mask is removed using chemical etching.

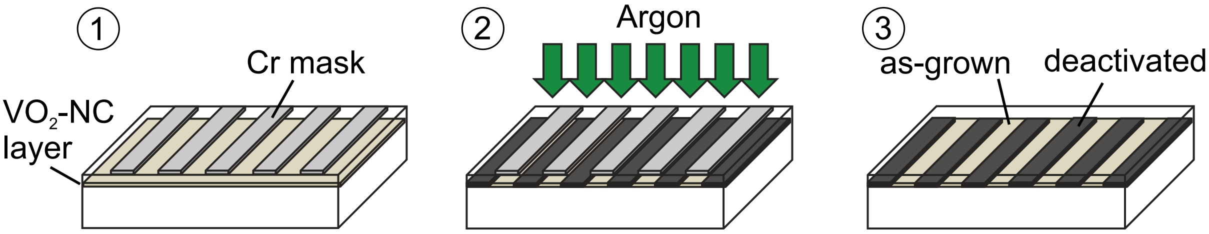

Fig. 7.5: Schematic steps of the fabrication of diffraction gratings in a VO_2-NC layer using the selective deactivation of the MIT with argon ions. See text for details. (Adapted from Zimmer et al. [87])

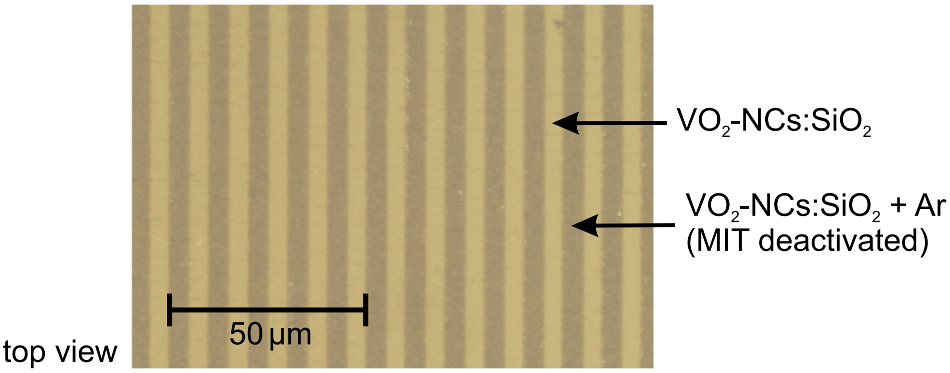

Fig. 7.6: Optical microscope top view of a VO_2-NC grating fabricated by selective deactiation process (from [87]). In the deactivated areas (brownish) areas the MIT is inhibited, while the NCs in the protected areas (yellow) remain as-grown and are able to undergo the MIT.

An optical microscope top view image of a grating fabricated by selective deactivation is displayed in Fig. 7.6. As is evident from the differently colored stripes, the transmission of visible frequencies is different for deactivated and as-grown areas, both in the insulating phase. The desired grating structure is clearly resolved. If a such-processed sample is heated above T_C, the MIT-induced switching of the dielectric contrast leads to a giant modulation of the diffraction efficiency of the grating. The idea of optically creating reconfigurable photonic elements in VO_2-NC samples is based on this demonstration of pre-defined, switchable diffraction gratings. The procedure of selective deactivation is also used in the context of this thesis to create switchable plasmonic grating couplers, see Chapter 9.

Before moving on to the demonstration of photonic elements, which rely on an all-optical imprinting of the dielectric contrast patterns, the origin of the diffractive functionality in VO_2-NC samples is discussed. With respect to gratings created by the dielectric contrast of the two VO_2 phases, the description of diffraction given above has to be extended. In the simple picture of a slit grating, the transmission of light is modulated between 1 and 0, i.e. light is fully blocked or transmitted. However, a diffractive functionality is also achieved by a partial periodic modulation of the transmission, as it is given due to the different extinction coefficients k of insulating and metallic VO_2. These lead to a difference in transmission of 20 % - 30 %. Since now only a fraction of the light's amplitude is affected by the diffraction, the resulting interference can only be partial and the diffraction efficiency is reduced. Note that the angles of diffraction are still given by Eq. (7.1).

As a final remark, the effects of a change in the real part n of the VO_2 refactive index is addressed. A periodic modulation of the optical path length is commonly used to create so-called 'phase gratings' with low losses and high diffraction efficiency (see Ref. [3], pp.136-141). This modulation is, in principle, also present in the VO_2-based gratings since the MIT-induced change of the refractive index $\Delta n \neq 0$ for most wavelengths. However, the phase shift turns out to be negligible, since it does not exceed $\Delta\phi = L \cdot \Delta n / \lambda \approx 1.4\,\%$ in units of the wavelength, with $\lambda = 0.905\,\mu\text{m}$, $L = 90\,\text{nm}$ and $\Delta n = 0.14$.

In the following section, the fact that diffraction gratings can be created using VO_2 and the ability to optically prepare a long-term stable metallic state are combined to demonstrate the optical imprinting of photonic elements.

7.3 Demonstration of Reconfigurable Photonic Elements

As has been shown above, local control of the MIT is made possible using spatially selective optical heat deposition with focused laser radiation. The laser can be imagined as a brush that creates a two-color image on a blank canvas, which is the VO_2-NC sample. This illustrative picture is actually not very far fetched since the color of insulating and metallic VO_2-NCs is slightly different due to the altered transmission in the visible wavelength regime, see Fig. 7.6.

The large bistability of the MIT facilitates the generation of a long-time stable metallic phase at slightly elevated lattice temperatures. Fig. 7.7 illustrates the principle of imprinting reconfigurable photonic elements. If the nominal sample temperature is kept in the range of ≈ 35°C-75°C, metallic areas can be written optically. Erasing any imprinted pattern is achieved in a non-destructive fashion by cooling the sample to below room temperature. In the following, different photonic elements are optically imprinted. As fundamental paradigms, two of the most commonly used devices are demonstrated, namely diffraction gratings and Fresnel zone plates. Different concepts to achieve the desired illumination pattern are examined.

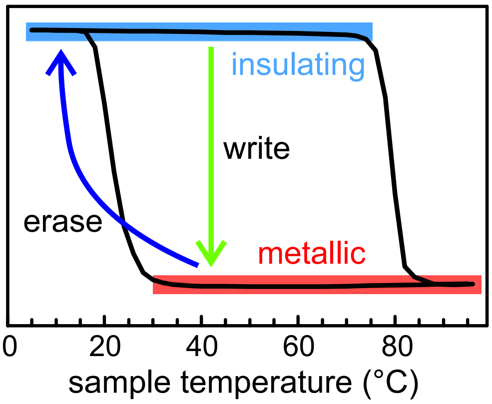

Fig. 7.7: Principle of optical writing and thermal erasing of dielectric patterns in VO_2-NC samples taking advantage of the broad hysteresis of the phase transition.

Diffraction Gratings: Interference-Based Inscription

In a first example, a grating structure of 15 µm periodicity is imprinted by creating a pattern of alternating stripes of insulating and metallic VO_2. The corresponding spatial distribution of the laser irradiance is generated by interfering two cw 532 nm pump beams that impinge on the sample with a relative angle of ≈ 3°. The nominal sample temperature is kept at 40°C during the optical definition of the gratings. As shown above, the thermal hysteresis of the

MIT ensures that the imprinted structures persist after the short-term optical excitation.

The experimental setup is an extended version of the one shown in Fig. 7.1, see Fig. 7.8. A beam splitter plate divides the focused pump beam in to equally powerful parts that interfere on the sample surface. In addition to the InGaAs photodiode, which measures the 0. order probe transmission through the sample, a large-area Ge photodiode is employed to collect the 1. order diffraction of the probe laser. Lock-in detection is used for both signals. In order to limit lateral heat diffusion, the duration of the pump beam exposure is set to 1 ms using the mechanical shutter. The spatially periodic, short-term heat deposition by the interfering beams results in a correspondingly striped pattern of insulating and metallic VO_2-NCs. Owing to their different complex dielectric functions, the structure acts as a diffraction grating for the telecom probe radiation.

To verify the functionality of the gratings created with this 'one-shot inscription', the diffraction of a cw 1.55 μm probe laser is analyzed before and after the inscription. The probe beam is focused to the center of the dielectric pattern to ensure the interaction with the imprinted grating. The pump irradiance pattern and the probe spot are illustrated in Fig. 7.9. Data of the transmission (black) and the first order diffraction efficiency (red) is displayed in Fig. 7.10, as a function of the irradiance of the 1 ms pump pulse. The efficiency is defined by normalizing the diffracted signal strength to the unpumped transmissivity.

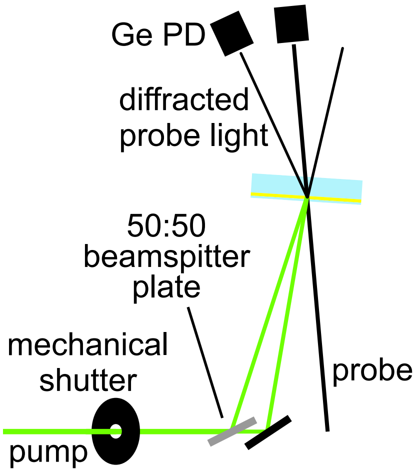

Fig. 7.8: Scheme of the experimental setup used for the one-shot inscription of grating patterns in VO_2-NC samples.

Using the one-shot approach, diffraction gratings are successfully imprinted into the VO_2-NC layer, as is evident from the data showing the diffraction efficiency for increasing pump irradiance in Fig. 7.10. For small pump irradiance, the probe transmission is nearly unchanged, which means that most NCs are still insulating. When the transmission starts to decline at a higher pump irradiance of about 1.15 kW/cm^2, stripes of metallic NCs are written into the sample and a diffractive functionality is generated. Only a small interval of pump irradiances provides the proper amount of heating to trigger the phase transition in areas with constructive interference, while at the same time preventing heat diffusion from raising $T > T_C$ in the entire illuminated area. In essence, for insufficient ($<$ 1.1 kW/cm^2) or excessive ($>$ 1.6 kW/cm^2) pump irradiance, the NCs in this area remain insulating or switch to the metallic phase, respectively. Both findings are corroborated by the transmission data in Fig. 7.10, which shows a signature similar to those seen for homogeneously illuminated NCs, i.e. a drop of transmissivity to ≈ 0.8.

In the present approach, the peak diffraction efficiency does not exceed $2 \cdot 10^{-4}$. To gain a benchmark for the maximum possible efficiency of gratings based on VO_2-NCs, a pre-defined grating with 10 μm periodicity is analyzed, which was fabricated using the method of selective deactivation presented above. At high sample temperatures, when the as-grown NCs switch to the metallic phase and the grating is activated, a maximum diffraction efficiency of $1.7 \cdot 10^{-3}$ if found. The efficiency of the grating inscripted with the interference-based method is about one order of magnitude smaller. This finding points to a dielectric contrast that is limited by heat diffusion in this approach of interfering two large-area pump beams. Nevertheless, the results evince the demonstration of the fast imprinting of long-time stable two-dimensional photonic patterns that can be non-destructively erased by cooling the sample to below room temperature.

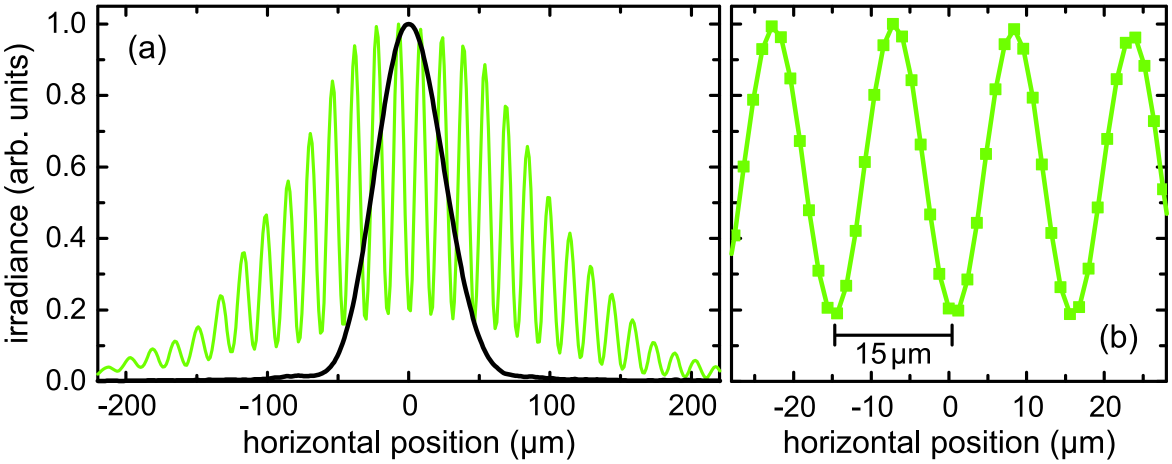

Fig. 7.9: (a) Horizontal scan of the 532 nm pump (green) and 1.55 µm probe (black) irradiance profiles recorded with a rotating slit beam profiler. (b) Close-up of the inner part of the interference pattern demonstrating the interference contrast.

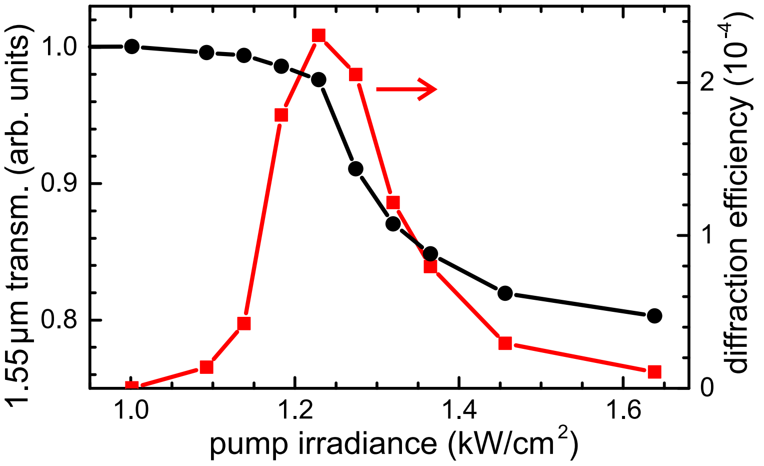

Fig. 7.10: Pump power dependence of the transmission (black) and the first order diffraction (red) of 1.55 µm probe light interacting with the optically imprinted grating of 15 µm periodicity.

Diffraction Gratings: Pixel-Type Inscription

The results of the interference-based inscription show that more sophisticated ways of generating a spatially confined MIT are needed. In this part of the text, a 'pixel-type inscription' of photonic patterns using tightly focused beams is presented. Small metallic areas, which can be seen as pixels in the two-color image mentioned above, are inscripted successively. The goal is to improve the spatial dielectric contrast, and to be able to define more complex patterns of insulating and dielectric VO_2-NCs.

To this end, the sample is mounted on a two-dimensional motorized translation stage with sub-µm accuracy. It is used to move the sample in lateral directions, i.e. in-plane of the surface. An aspheric lens with a focal length of 11 mm focuses the 532 nm pump light down to a spot size of ≈5 µm (FWHM). The area undergoing the MIT is reduced even below this optical spot size by utilizing the strongly nonlinear character of the MIT. For this purpose, the pump power and the duration of illumination are adjusted such that only the center section of the Gaussian irradiance profile of the illuminated area is heated sufficiently strong to locally raise the temperature above T_C. On the other hand, pixels with a diameter bigger than the optical spot size can be imprinted with higher pump powers or longer durations of illumination. The heat deposition and the consequent size of the metallic pixels can be adjusted using these experimental parameters.

In the present experimental configuration, this approach allows to locally drive the MIT using 10 mW pump pulses of ms duration such that low-cost laser diodes are sufficient to imprint photonic patterns. Fig. 7.11 shows a sketch of the different optical configurations used in the following to optically write metallic pixels, map the imprinted dielectric pattern and analyze the diffractive functionality.

Fig. 7.12(a) illustrates the procedure of pixel-type inscription. After each 2 ms excitation event, the sample is moved to the next target area. The mechanical shutter and the two-

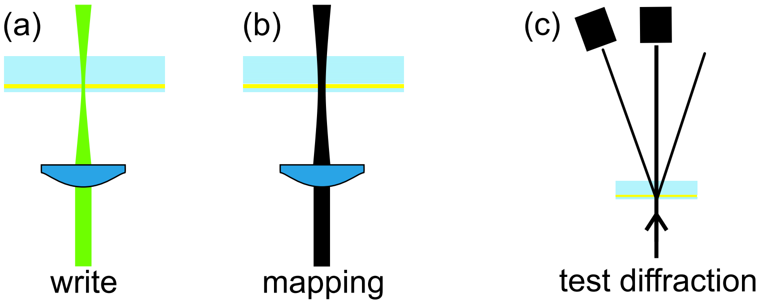

Fig. 7.11: Illustration of the different beams and focusing geometries. The sample is movable with sub-µm accuracy in lateral dimension. (a) Areas of metallic VO_2 are written with a cw 532 nm beam focused to ≈ 5 nm (FWHM) using an aspheric lens. (b) A cw 1.55 µm probe beam is focused through the same lens to a ≈10 µm (FWHM) spot, in order to map the imprinted structures. (c) The probe beam is loosely focused to ≈100 µm (FWHM) to measure the diffraction efficiency of the gratings, cf.. the setup depicted in Fig. 7.8.

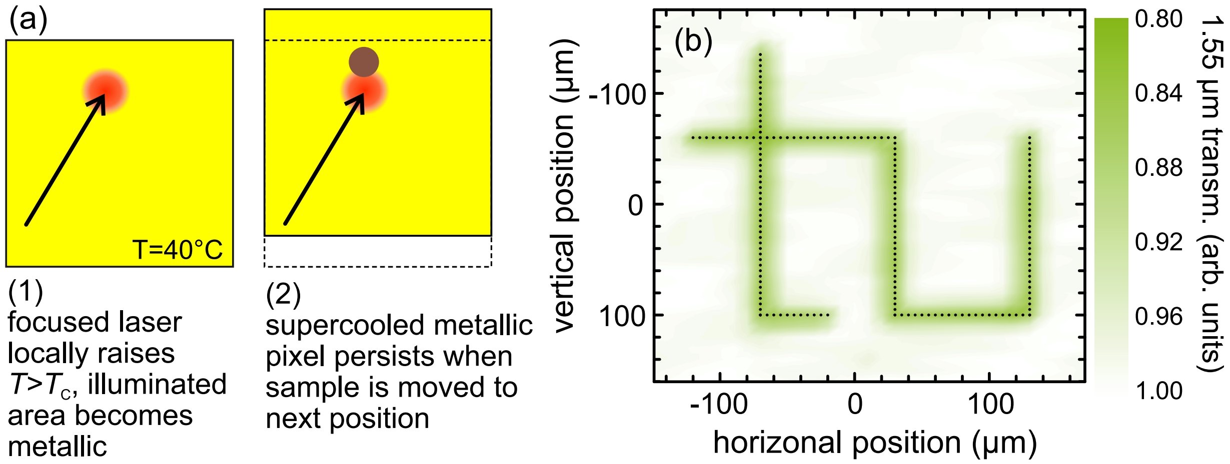

Fig. 7.12: (a) Illustration of the point-by-point inscription of metallic areas (brown) in an environment of insulating VO_2-NCs (yellow). (b) Demonstration of an arbitrary dielectric pattern imprinted into a VO_2-NC sample mapped by monitoring the transmission of a focused probe pulse. Dots mark the positions of photoexcitation.

dimensional translation stage are synchronized in a home-built LabView program to ensure the correct timing of these actions. Since the sample temperature is kept at $T = 40°\mathrm{C}$, and the supercooled metallic phase is persistent, arbitrary lateral patterns of insulating and metallic areas can be written without inherent limitations to the duration of the entire procedure. Note that any additional heating of metallic VO_2-NCs has no consequence on their phase or dielectric properties. Therefore, a spatial overlap of consecutive excitations is not detrimental, but rather allows to imprint connected metallic areas.

Fig. 7.12(b) shows a map of the transmissivity of the 1.55 µm probe beam, created by monitoring the transmitted intensity and moving the sample in lateral dimensions. The spatial resolution of the map is $\approx 10\,\mu\mathrm{m}$, given by the spot size of the probe beam at the sample surface. It is evident that the desired structure was successfully translated into the dielectric contrast.

Moving on, the pixel-type inscription is demonstrated using the example of a diffraction grating with 20 µm periodicity. The stripes of supercooled metallic VO_2 are formed by subsequently switching circular areas that are lined up like a string of pearls. Fig. 7.13 shows a 2D transmissivity map of the grating created by this successive definition. Ideally, areas in the metallic and insulating phases are represented by 1.0 and ≈ 0.8 transmissivity, respectively. These values are not seen in the map, because the spatial resolution is limited by a convolution of the Gaussian probe beam intensity profile and the imprinted dielectric contrast. Nevertheless, the grating structure composed of stripes of alternating metallic and insulating VO_2 is clearly resolved.

In the next step, gratings with different periodicity are subsequently imprinted into the same VO_2-NC sample and analyzed using the procedures described above. All gratings are created at a sample temperature of 40°C and erased by cooling to 10°C. Similar to the

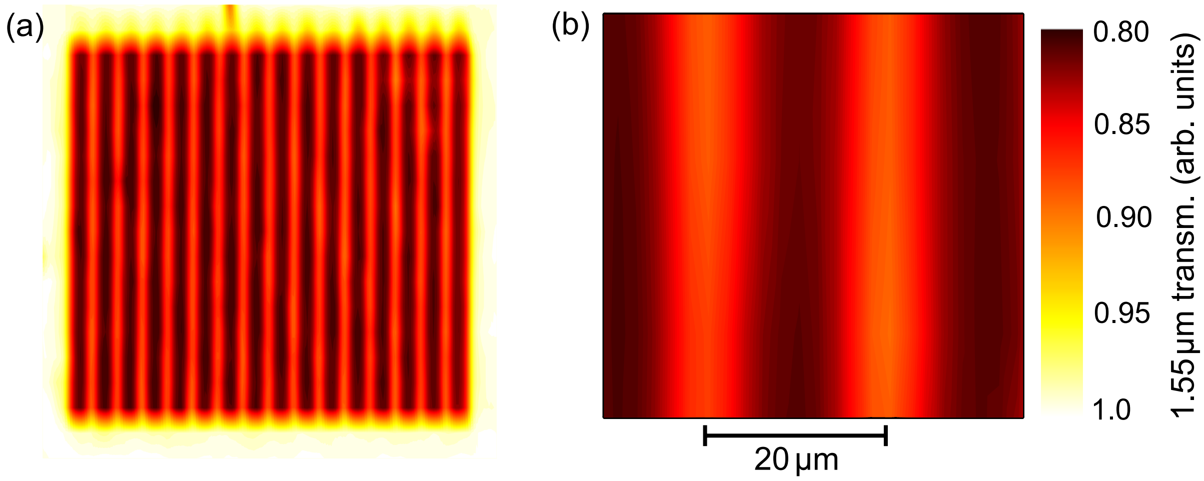

Fig. 7.13: (a) Transmissivity map of a 400µm × 400µm area of alternating stripes of insulating and metallic VO_2-NCs forming a diffraction grating. (b) Close-up showing the dielectric contrast between the stripes represented by the different transmissivity. The spatial resolution is ≈ 10 µm.

gratings created using the interference-based inscription, only certain combinations of pump power and duration results in a situation where half of the NCs are in either phase. For the present pixel-type approach, 2 ms pump pulses of 10 mW-15 mW power are used. The diffraction efficiency of the grating is determined by measuring the transmission and the first order diffraction of a 1.55 µm probe beam loosely focused to ≈ 100 µm (FWHM). As seen in Fig. 7.14(a), the gratings feature first order diffraction efficiencies of up to $1.7 \cdot 10^{-3}$, i.e. about one order of magnitude larger when compared to an inscription with interfering large area pump beams presented above. Apparently, the short-term heat deposition from tightly focused optical beams leads to much less heat dissipation when compared to the interference-based approach.

The diffraction angle markedly shifts with the grating period, as expected. Note that the angles of diffraction found in the experiment agree well with Eq. (7.1). The maximum diffraction efficiency decreases for decreasing grating periodicity. This behavior is most likely due to the reduced quality of the gratings and an increasing duty cycle, caused by narrower insulating stripes.

The fact that a grating with a periodicity of 6 µm is imprinted using pump spots with a diameter of 5 µm FWHM demonstrates how the strong nonlinearity of the MIT helps to create structures with µm resolution. The maximum efficiency of $1.7 \cdot 10^{-3}$ is equal to the values obtained with the pre-defined gratings fabricated using defect engineering with Ar ions. Therefore, it can be concluded that the optically generated micropatterns succeed in attaining the maximum possible dielectric contrast in the VO_2-NC samples.

Owing to the broad thermal hysteresis of the MIT, any imprinted structure is long-term stable (cf. Fig. 7.3) and can be erased in a non-destructive fashion if the temperature is reduced to $T < 20°C$. This fact is evident from Fig. 7.14(b), where the diffraction efficiency of a grating imprinted at 40°C sample temperature is displayed for decreasing temperatures. The dielectric contrast vanishes at temperatures below ≈20°C in accordance with the thermal hysteresis presented above. In essence, the grating is erased and the sample is reset to an unstructured, homogeneous state.

To sum up, the approach of inducing the MIT pixel by pixel with focused beams allows to control the detrimental heat dissipation to a great extent. It leads to a superior dielectric contrast and offers the possibility to imprint arbitrary 2D photonic patterns with μm resolution. In the next step, the approach is slightly varied and more complex planar photonic elements are demonstrated.

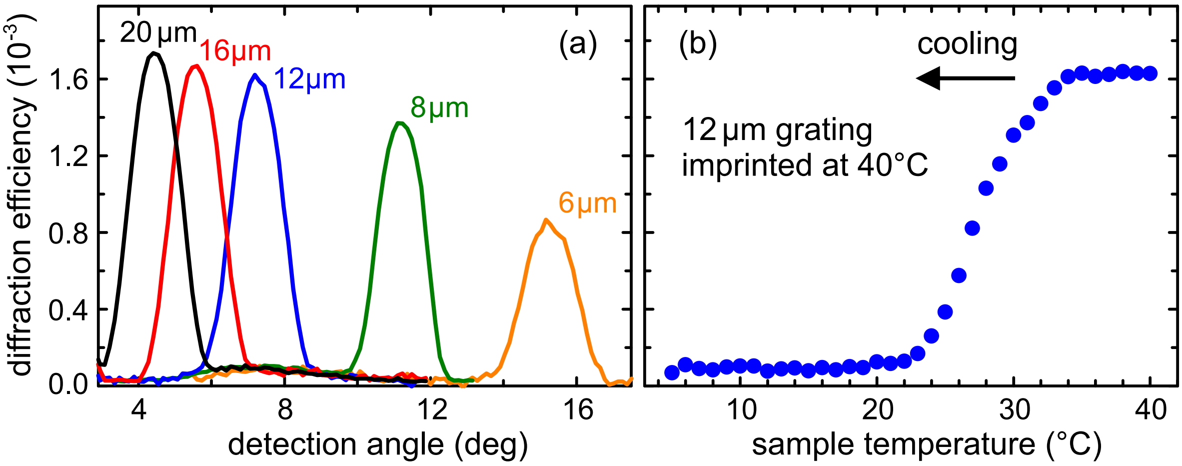

Fig. 7.14: (a) Angular scans of the diffraction efficiency of grating patterns formed from insulating and metallic VO_2-NCs. The number next to the lines states the grating's periodicity. (b) Temperature dependence of the diffraction efficiency. After the preparation of the grating at 40°C, the sample is cooled down to 5°C. The insulating state is fully recovered at temperatures below 20°C.

On- and Off-Axis Zone Plates: Continuous Inscription

The method of the pixel-type inscription is now expanded to create more sophisticated planar dielectric patterns of alternating insulating and metallic VO_2-NCs. Instead of using consecutive singular excitation events, the sample is now moved with a constant in-plane velocity while a continuous 532 nm pump spot induces the MIT. Any desired structure can now be written by driving the corresponing trajectories. As an example for this approach of 'continuous inscription', on- and off-axis zone plates are imprinted into a VO_2-NC sample.

A zone plate is a planar photonic element capable of focusing and redirecting beams of electromagnetic radiation using only diffraction. This fact distinguished its operating principle from lenses or parabolic mirrors that work with refraction or reflection at curved surfaces in order to focus light. Using a speficially designed zone plate, any electromagnetic or particle wave can be focused independent of the index of refraction of the utilized material for the specific spectral region. In modern X-ray optics, zone plates are commonly used for wavelength regions where most materials either strongly absorb or show only weak refraction [142]. Further applications of zone plates can be found in photography, holography and synchrotron optics [142]. Since zone plates can be constructed to have two planar interfaces, they are beneficial for the integration into thin planar photonic nanostructures. Historic background on the development of different types of zone planes and further details can be found in Refs. [143] and [144].

In general, an on-axis zone plate consists of concentric areas (rings) that alternate in transmissivity or optical path length. In the most basic configuration, depicted in Fig. 7.15, the circles alternate between being fully opaque and transparent. When this structure is illuminated under normal incidence and the irradiance of light is distributed radially symmetric, light will be focused to a point on the optical axis (which is normal to the center of the zone plate). In a simple picture, this focusing ability can be understood considering the zone plate to be composed of circular diffraction gratings with a periodicity that decreases from the center to the outside. Each grating is oriented in a way that makes diffracted orders of light hit the optical axis. The varying periodicity makes sure that diffracted light from all parts of the zone plate gathers at the same distance to the center of the zone plate. This spot is the focal point. Because larger angles of refraction are needed for light transmitted through the outer rings, the gratings periodicity decreases for increasing radii.

In a more fundamental point of view based on Huygen's principle, the design of the zones ensures that light originating from the transparent (opaque) zones interferes constructively (destructively) at the focal point. The radii of the alternating rings have to be chosen such that the difference in path lengths Δl from points in the transparent zones to the focal point is $0 < \Delta l < \lambda/2$, where λ is the wavelength of the incoming light. Any radiation

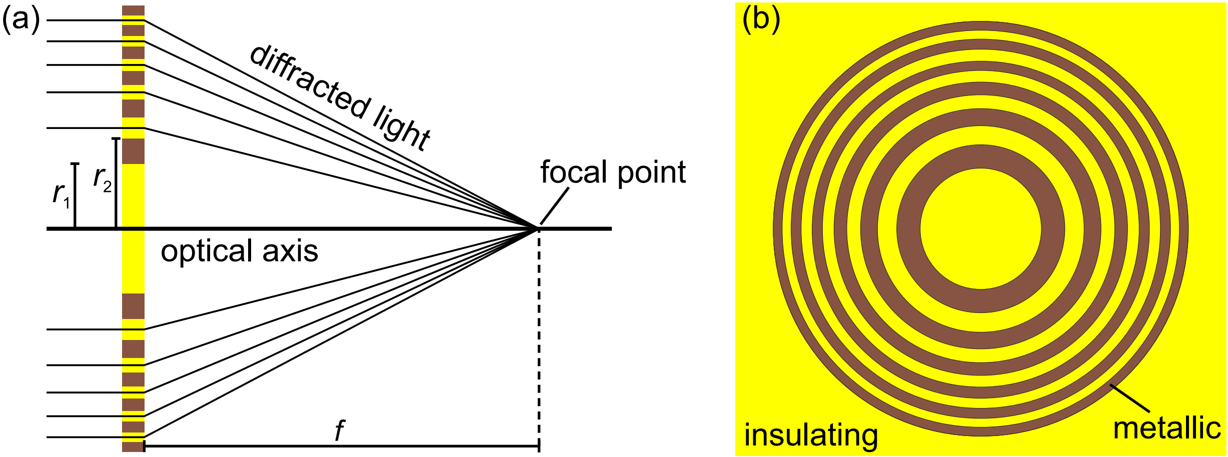

Fig. 7.15: (a) Schematic cross-section of a planar zone plate consisting of transparent (yellow) and opaque (brown) areas. The radii r_i are given by Eq. (7.2). Light from all points of the zone plate is diffracted to a mutual point on the optical axis of the system. (b) Schematic front view of the zone plate imprinted into a VO_2-NC sample.

transmitted through these zones will interfere constructively at the focal point. Vice versa, light originating from opaque zones has to fulfill $\lambda/2 < \Delta l < \lambda$ in order to ensure destructive interference. Owing to these requirements, the alternating rings are called half-wave zones. The radius of the m-th half-wave zone boundary r_m scales as (see Fig. 7.15(a) for an illustration and Ref. [144] p.5, or Ref. [143] for the derivation)

$$r_m = \sqrt{\left(\frac{m\lambda}{2}\right)^2 + m\lambda f} \approx \sqrt{m\lambda f} \quad , \tag{7.2}$$

where f is the focal length of the zone plate. The approximation is valid for $\lambda \ll f$.

Similar to diffraction gratings, zone plates are able to function based on both amplitude or phase (path length) modulations (see Ref. [144], pp.5-6). In the specimen under investigation in this thesis, the diffractive functionality is created by the different dielectric constants of the two phases of VO_2-NCs . As has been pointed out during the discussion of VO_2-based diffraction gratings in Section 7.2, the diffraction is dominated by amplitude modulation caused by the increased absorption in the metallic areas. In the context of the description of zone plates given above, metallic corresponds to opaque. However, instead of completely blocking the transmission, it is merely reduced by $\approx$ 30 %[3].

As a first example, a zone plate with a focal length of $f = 100$ mm for $\lambda = 1.55$ µm light is optically imprinted. Using these parameters, the widths of the metallic (opaque) rings, as determined by Eq. (7.2), range from $r_1 - r_2 = 163$ µm to $\approx$32 µm for the outer rings up to $m = 38$. In order to achieve the corresponding illumination pattern, the two-dimensional translation stage is programmed to move along circles with an in-plane velocity of 1 µm/ms while a continuous 532 nm, 10 mW pump spot of 5 µm diameter (FWHM) illuminates the VO_2-NCs. The radii of consecutive circles are increased in steps of 6 µm to ensure the formation of uninterrupted, areal metallic rings. Fig. 7.16 shows transmissivity maps of the imprinted zone plate, recorded with a 1.55 µm beam focused to a spot diameter of $\approx$10 µm (FWHM). The dielectric contrast between areas of insulating and metallic VO_2-NCs is clearly resolved, especially in the close-up in Fig. 7.16(b).

To verify the functionality of this zone plate, it is illuminated with a non-focused 1.55 µm probe beam with a diameter of $\approx$2 mm (FWHM). The irradiance profile of the beam is approximately Gaussian and centered in the middle of the zone plate, thus ensuring a radially symmetric illumination. Fig. 7.17 shows the spatial irradiance profile of the beam recorded at 100 mm behind the sample plane with (red) and without (blue) the optically imprinted photonic pattern. Upon definition of the zone plate, the overall far field transmission decreases by about 15 %, which is expected since $\approx$50 % of the NCs are now are in the

---

[3] The sample used for the zone plate experiments features a stronger transmission decrease and a smaller hysteresis width, when compared to the one used for the optically induced MIT and the inscription of gratings. Presumably, the NCs in the sample used here are slightly larger.

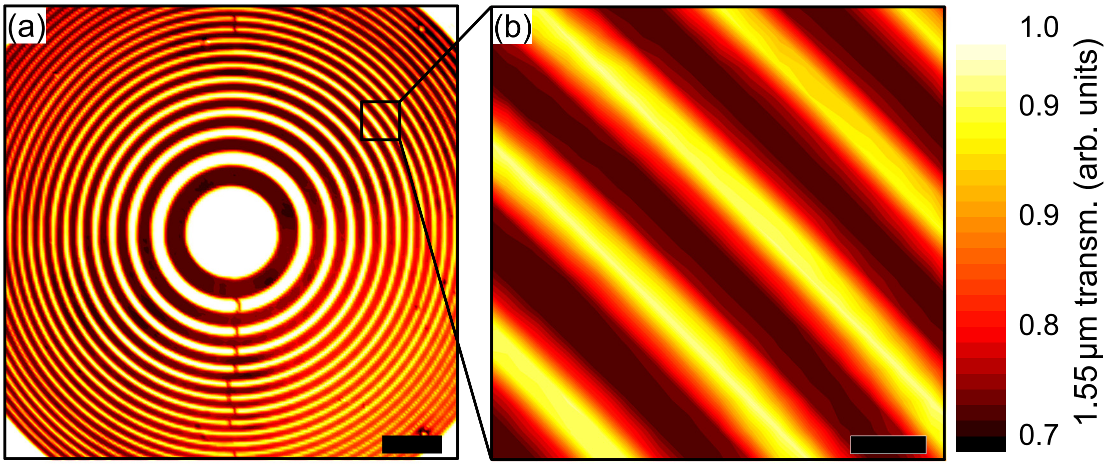

Fig. 7.16: (a) Transmissivity map of an on-axis zone plate defined by an optically imprinted pattern of insulating and metallic VO_2-NC at a sample temperature of 40°C. The scale bar is 500 µm. (b) Close-up of a part of the on-axis zone plate showing the dielectric contrast between the two phases of VO_2. The scale bar is 40 µm.

metallic state. Note the the dielectric pattern is not resolvable in the far field transmission of this large area beam. More importantly, the zone plate creates a focal spot in the center of the beam profile, which demonstrates the functionality of the imprinted zone-plate. As displayed in Fig. 7.17(b), the diameter of the nearly Gaussian profile of this focal point is ≈ 40 µm (FWHM). The local light intensity is enhanced and exceeds the intensity measured without an imprinted zone plate by 7 %, despite the absorption losses caused by the metallic VO_2-NCs. Note that the cross-section shown here is a horizontal cut through the beam's irradiance profile. The vertical cross-section shows the same additional focal point in the center of the beam.

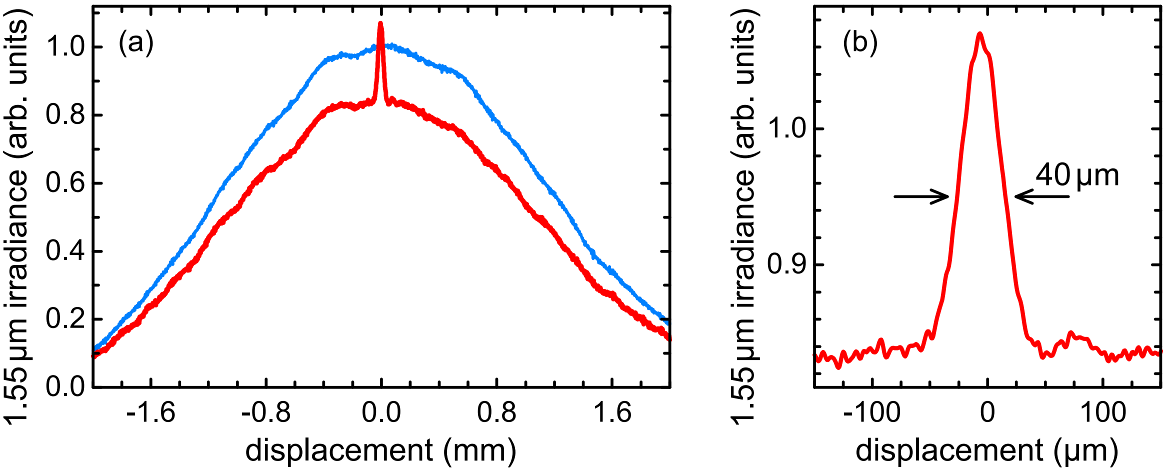

Fig. 7.17: (a) Cross-section of the $\lambda = 1.55$ µm beam in the focal plane of the on-axis zone plate before (blue) and after (red) optical imprinting of the zone plate recorded with a rotating-slit beam profiler. (b) Close-up to the additional focal spot created upon definition of the zone plate.

Moving on, the opportunity to create arbitrary two-dimensional photonic patterns is utilized further. The depictions of the working principle of zone plates made above are valid for on-axis zone plates. A different functionality can be achieved by creating off-axis zone plates. As the name implies, the focal point of an off-axis zone plate is not located on the optical axis (normal to the center of the zone plate) but is shifted to another point in the focal plane. This functionality is generated by illuminating only an outer section of the zone plate, as shown in Fig. 7.18(a). Essentially, this pattern merges the ability of a diffraction grating to change the direction of propagation of a light beam with the ability of a zone plate to focus light.

Fig. 7.18(b) displays the irradiance of the large area 1.55 µm probe beam at 100 mm behind the sample both with (red) and without (blue) the optically imprinted off-axis zone plate. The section of the beam profile shown here is displaced horizontally from the center. Again, the overall transmission decrease is due to the increased absorption in the metallic VO_2-NCs. Remarkably, a part of the probe light is now focused to a ≈ 45 µm spot (FWHM) outside of the transmitted beam, in accordance with the expected effect of the off-axis zone plate. Note that the horizontal cross-section is shown in Fig. 7.18(b). The vertical cross-section of the beam profile looks like the one shown in Fig. 7.17(a), with to focal spot in the center of the profile.

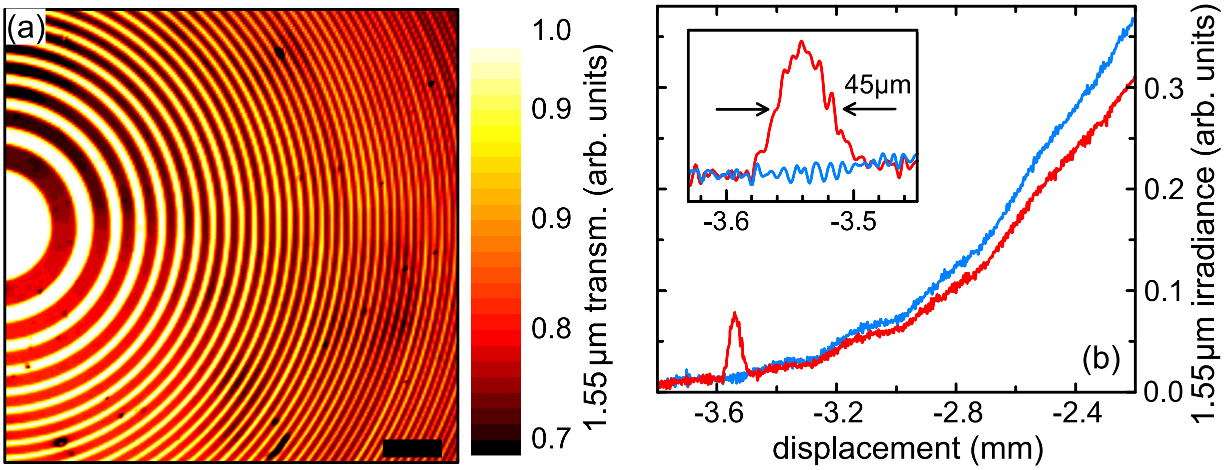

Fig. 7.18: (a) Transmissivity map of an optically defined off-axis zone plate. The scale bar is 500 µm. (b) Cross-section of the $\lambda = 1.55$ µm beam in the focal plane of the off-axis zone plate before (blue) and after (red) the optical imprinting of the zone plate. The inset shows the focal spot generated by the off-axis zone plate.

Chapter 8

Introduction to Surface Plasmon Polaritons (SPPs)

Apart from the applications of VO_2 addressed in the previous two chapters, it is also envisioned to be utilized for active plasmonic devices. The research field of plasmonics is a rapidly evolving area of photonics that relies on the interaction of free electrons in metals with light. The following section introduces plasmonics and how the interesting characteristics of VO_2 contribute to it. In the remainder of this thesis, different plasmonic elements based on VO_2 nanocomposites are demonstrated. The MIT-induced change of the dielectric function of VO_2-NCs is exploited to manipulate the coupling of light to surface plasmon polaritons (SPPs). In Section 8.2, the physics of SPPs at a gold-air interface is discussed together with a mathematical description. Section 8.3 describes the experimental setup employed for the excitation and detection of SPPs.

8.1 Motivation and Overview of the Field of Research

Plasmonic research comprises the science and applications of the interaction of electromagnetic fields and electrons at metal interfaces or in metallic nanostructures. Under certain circumstances, light and electrons strongly interact and form a hybrid quasiparticle composed of light and electrons called surface plasmon polariton (SPP).

In a simple yet successful approach, conducting electrons in a metal are treated like a dense liquid of free electrons ($\sim 10^{23}\,\mathrm{cm}^{-3}$) called plasma. Maxwell's equation show that the electron plasma can be excited to perform collective spatial oscillations called plasmons. In a bulk material, these volume plasmons can be visualized as a periodic, wave-like movement of the electron density against the restoring force of the background of ion cores.

As it happens in several fields of physics, intriguing and unexpected phenomena happen when the dimensions of the system approach the nanoscale. In the context of plasmonics, two main types of excitations emerge from either sub-wavelength structures such as metallic nanoparticles, or discontinuities in a heterostructure in the form of planar metal-dielectric interfaces. In the latter case, the interface supports electromagnetic surface waves called surface plasmon polaritons (SPPs). In essence, a SPP is composed of a light field that is bound to the surface of a metal because of a strong interaction with plasmons that propagate along the surface. The term 'polariton' reflects the photonic part of this quasiparticle.

The applications of and the research on localized plasmon resonances and SPPs are manifold. The sheer number of papers published per year ($\approx$ 8500 in 2014 and 2015 each) complicates a comprehensive overview of the ongoing research. To get an synopsis of the $\sim$ 100 years of history, the current stage and the future challenges of plasmonics, the reader might refer to a focus issue of Nature Photonics [22; 23]. In the following, a few of the most prominent applications that pushed this field of research are introduced.

One of the most interesting features of plasmons and SPPs is the fact that the light field is concentrated to dimensions of down to one hundredth of the wavelength of the light coupled to the SPP [145]. The electron oscillations can be excited by an external light field, thereby transforming far-field to near-field radiation. Specifically, the light's amplitude is maximum at the interface and decays exponentially into the metal on a distance of 10-30 nm, thereby beating the optical diffraction limit by more than one order of magnitude. A overview of current research on the prospects of nanoplasmonic can be found in the review article 'Plasmonics beyond the diffraction limit' [24].

An advanced class of applications are SPP-based sensors that utilize the strong sensitivity to the plasmon's properties on the sorroundings [146; 147]. Plasmonic sensor devices even reached the stage of ready-to-use commercial products. Surface plasmon resonance sensors are based on a method of exciting SPPs on plain metal films called 'attenuated total reflection' that is also part of the examinations carried out in this thesis (see Chapter 10). This type of sensor is commonly used in biomedical and genomic applications such as monitoring the affinity binding of molecules or studying DNA, RNA, proteins etc. [147]. The technique of surface-enhanced Raman spectroscopy (SERS) is able to detect the signature of single molecules adsorbed on metallic nanostructures [148; 149].

In a different class of applications, the field enhancement and symmetry breaking related to the bound nature of plasmons in nanoantennas is utilized in nonlinear optics. Recent developments in the research field of nonlinear plasmonics are second harmonic generation [68; 150] and the generation of extreme-ultraviolet light using high harmonic generation [151]. A review of nonlinear plasmonics can be found in Ref. [152].

Plasmonic interactions are also envisioned to enhance the efficiency of photovoltaic devices by exploiting their ability to catch and control light on the nanoscale [153; 154]. In thin film solar cells, the efficiency of transforming light to electrical energy is limited due to the low overall absorption. The addition of metallic nanoparticles or gratings structures helps to enhance the interaction of the light field with the active layer (which is usually silicon). In the same manner, nanoparticles help trapping light and increase the efficiency of organic solar cells [155].

The ability of plasmonic structures to confine optical and electronic information in lateral dimensions of $\sim 10\,\mathrm{nm}$, and guide it over length scales of $\sim$ mm, makes SPPs a promising candidate for future on-chip data processing [24; 156; 157]. They offer the opportunity to transfer information on metallic surfaces, nanowires or other waveguide designs and link optics and electronics on the nanoscale. The on-chip data transport or processing could potentially be done with light instead of pure current flow. In principle, SPPs also allow to use electronic and photonic degrees of freedom simultaneously. In order to create plasmonic circuits, a variety of elements is needed that convert light to SPPs and vice versa or steer SPPs on the chip: switches, modulators, in- and output couplers, waveguides and so on. Reviews of several implementations and designs that have been demonstrated so far can be found in Refs. [24; 156; 157].

The research on plasmonic elements carried out in the context of this thesis belongs to the field of active plasmonics. This area of research focuses on the fast and deterministic control of SPP launching or propagation. Ultimately, the goal is to find designs that allow for the ultrafast manipulation of light-SPP coupling on the nanoscale and, thereby, achieve the transfer of digital information (bits) onto SPPs. The conditions of light-SPP coupling and the properties of SPPs are very sensitive to the effective dielectric functions of media in their near field. Consequently, the active control of SPP launching using the controlled and fast manipulation of the dielectric properties associated with the photoexcitation is the topic of ongoing research. So far, most concepts have relied on electrical [158], electro-mechanical [159; 160] or (ultrafast) optical manipulations [161; 162]. A way to achieve even more substantial changes is the use of structural phase transitions [20].

In this thesis, the use of vanadium dioxide nanocrystals (VO_2-NCs) for the active control of SPP launching in the telecom wavelength regime is investigated. The aim of the research performed in this thesis is the thermochromic modulation of SPPs in vanadium dioxide (VO_2) nanocomposites. VO_2 is one of the most studied phase change materials for photonic and plasmonic applications because of its metal-insulator phase transition (MIT) that is accompanied by a marked change of the dielectric function. Several recent studies have been devoted to the use of VO_2 for modulating plasmonic functionalities [86; 140; 163–167], including the propagation of SPPs [72; 168; 169], sensor functionality [170] and antenna resonances [171–173]. In addition, similar concepts have been demonstrated based on other phase change materials (mainly chalcogenides such as $Ge_3Sb_2Te_6$) [174–179]. However, the benefit of VO_2 for active control of SPP launching in plain metal films has not been addressed so far.

The specimen used in this thesis are composed of VO_2-NCs embedded just below the surface of a gold-covered dielectric. The phase transition can be induced thermally, or optically on sub-picosecond timescales. In addition, it exhibits a large hysteresis with a supercooled metallic state near ambient temperatures. The bistability of nanoscale VO_2

specimen allows for the implementation of persistent, but erasable photonic elements [21] or plasmonic memory devices [86]. Owing to a Mie-type resonance of the spherical metallic NCs, the MIT-induced change of the dielectric function in the telecom windows is strongly increased compared to bulk films [109]. Furthermore, the spectral position of this resonance and the characteristics of the hysteresis can be engineered during the fabrication process. Details on the material system VO_2, the fabrication of the VO_2-NCs and the physics of the MIT and can be found in Chapter 6.

In order to optically launch SPPs on a metal-dielectric interface, the wave vectors of light and SPPs have to be matched, since free-space radiation does not carry enough momentum to excite SPPs (cf. Section 8.2). For this purpose, two main mechanisms have been identified. The benefits of combining VO_2 with both of these approaches for the purpose of demonstrating active plasmonic elements is investigated in this thesis:

(i) The wave vector of the incident light is increased using a spatially periodic structure in the near field of the SPP. This so-called grating-assisted coupling is realized using thermochromic diffraction gratings based on the site-selective deactivation of the MIT. As has been shown in Section 7.2, the dielectric contrast between insulating and metallic VO_2 allows to create switchable diffraction gratings. This fact is made use of for the demonstration of switchable thermochromic plasmonic grating couplers with giant switching contrast. See Chapter 9.

(ii) In a second set of experiments, the Kretschmann configuration is examined. Here, evanescent light created upon total internal reflection is able to excite SPPs on a plain metal film. The benefit of a VO_2-NC layer in the near field of the propagating SPPs is a marked MIT-induced modification of the light-SPP interactions that result in thermotunable plasmonic couplers. Extensive simulations of the optical response of this structure are in line with experimental results and measurements of the dielectric function of the VO_2-NC layer. See Chapter 10.

8.2 Fundamental Physics of SPPs

In this section, a short theoretical description of surface plasmon polaritons (SPPs) will be given. It is based on Maxwell's equations applied to an electromagnetic wave propagating at the interface of two semi-infinite media [180; 181]. Central findings will be applied to a gold-air interface, which is present in the samples examined in this thesis. The results of this mathematical treatment, especially the wave vector dispersion of SPPs, will be important for understanding the mechanisms of the different schemes of light-SPP coupling presented later in the text.

Mathematical Description of Surface Plasmon Polaritons

Fig. 8.1(a) shows a schematic of the interface between two semi-infinite media representing the dielectric and the metal. The interface is located in the x-y-plane at $z = 0$. For nonmagnetic media in the absence of external sources, Maxwell's vector equations for the electrical field strength **E** and the magnetic field strength **H** read

$$\nabla \times \mathbf{H}_i = \epsilon_0 \epsilon_i \frac{\partial \mathbf{E}_i}{\partial t} \quad , \quad \nabla \times \mathbf{E}_i = -\mu_0 \frac{\partial \mathbf{H}_i}{\partial t} \quad , \quad \nabla \cdot \mathbf{E} = 0 \quad \text{and} \quad \nabla \cdot \mathbf{H} = 0 \; , \tag{8.1}$$

where ϵ_i is the bulk dielectric function in the two media. In general, this function may be complex and depend on the frequency of light; this matter will be addressed later on in the text. The index i describes the two media, where $i = 1$ for $z > 0$ and $i = 2$ for $z < 0$. One can now construct an expression for the electromagnetic field of travelling SPPs that fulfills these equations. A propagation along the x-axis and a polarization of the transverse electric field in z-direction is considered, corresponding to TM polarized light. Since the mode of a SPP is confined to the interface, it is characterized by decaying electrical field z-components in the two surrounding media at $|z| > 0$. Fig. 8.1(b) shows a visualization of the SPP's electromagnetic field and the corresponding charge distribution in the metal. The wanted solution for travelling SPPs is written as

$$\mathbf{E}_i = \begin{pmatrix} E_{ix} \\ 0 \\ E_{iz} \end{pmatrix} \cdot \exp(\text{-}\kappa_i |z|) \cdot \exp[i(k_i x - \omega t)] \tag{8.2}$$

$$\mathbf{H}_i = \begin{pmatrix} 0 \\ H_{iy} \\ 0 \end{pmatrix} \cdot \exp(\text{-}\kappa_i |z|) \cdot \exp[i(k_i x - \omega t)] \tag{8.3}$$

where κ_i are decay constants and k_i is the magnitude of the wave vector corresponding to the propagation in x-direction. In addition to Eqs. (8.1), boundary conditions for the continuity of the field components parallel to the interface apply, which read $E_{1x} = E_{2x}$ and $H_{1y} = H_{2y}$. Inserting the equations (8.2) and (8.3) in (8.1), and considering these

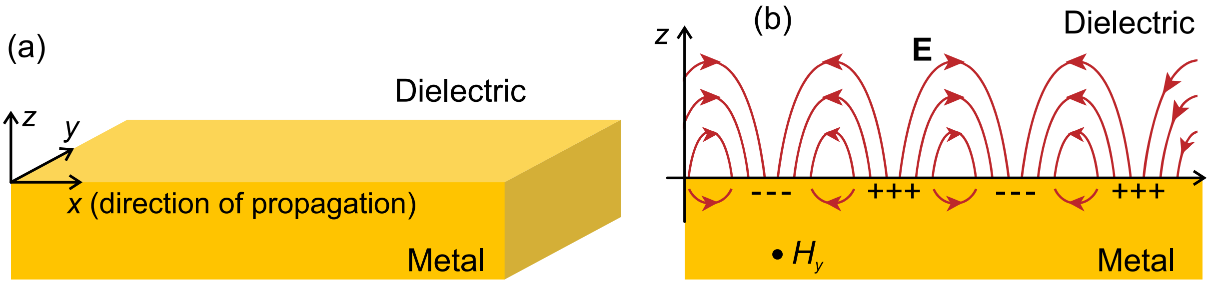

Fig. 8.1: (a) Schematic of the geometry used for the mathematical description of the SPP propagation along the interface between dielectric ($z > 0$) and metal ($z < 0$). **(b)** Visualization of the SPP's electric field amplitude **E** in the x-z-plane and the magnetic part H_y. The algebraic signs represent the electron charge accumulation, i.e. the plasma oscillations, that the SPP's electromagnetic field is coupled to (adapted from [145]).

conditions, leads to the system of equations

$$k_i^2 = \kappa_i^2 + \frac{\omega^2}{c^2}\epsilon_i^2 \tag{8.4}$$

$$\frac{\kappa_1}{\kappa_2} = -\frac{\epsilon_1}{\epsilon_2} \; . \tag{8.5}$$

The confinement of the electromagnetic mode and conservation of energy implies $\kappa_i > 0$ in both media. It is now obvious that the real parts of the dielectric functions in the two media must have opposite signs, in order to support SPPs at the their interface. This requirement is met when a dielectric and a metal are considered, as will be shown later. From the continuity of the electric field components follows $k_{\mathrm{SPP}} \equiv k_1 = k_2$, i.e. the continuity of the in-plane wave vector in the two media. The equations (8.4) and (8.5) can now be solved to obtain an expression for the in-plane wave vector of the SPP mode:

$$k_{\mathrm{SPP}} = \frac{\omega}{c}\sqrt{\frac{\epsilon_1\epsilon_2}{\epsilon_1+\epsilon_2}} \; . \tag{8.6}$$

All calculations performed so far could have been done assuming TE polarized light, with E_y, H_x, $H_z \neq 0$. However, considering the boundary conditions, it is straightforward to show that surface modes cannot exist under these circumstances (see Ref. [181], pp.26-27). Consequently, SPP modes only exist for TM polarization. A more descriptive argument for this restriction is provided by the spatially oscillating charge distribution in x-direction. The interaction of light with this charge distribution is only possible for $E_x \neq 0$.

So far, this section has shown that Maxwell's equations support the existence of collective electron plasma oscillations travelling along the interface of two media with $\epsilon_1/\epsilon_2 < 0$. The accompanying electric field is composed of longitudinal and transversal components. Next, these findings will be applied to a gold-air interface and light in the telecom wavelength regime, which corresponds to the experimental configurations examined in this thesis.

Surface Plasmon Polaritons at a Gold-Air Interface

To get a more specific understanding of the propagation of SPPs at a gold-air interface, the results of the previous section are now evaluated for the actual dielectric functions of these materials. Considering air as a dielectric, the situation is simple, since $\epsilon_1 = \epsilon_{\mathrm{air}} \approx 1$ in the visible and near-infrared wavelength regimes [182]. Gold is used throughout this thesis as the metal layer. The frequency-dependent dielectric function of gold $\epsilon_2 = \epsilon_{\mathrm{Au}}(\omega)$ in the near infrared is commonly described using a Drude model, where a gas of free electrons moves against fixed ion cores (see, for example, Ref. [181], pp.11ff). Following this model yields a complex dielectric function

$$\epsilon_{\mathrm{Au}}(\omega) = 1 - \frac{\omega_{\mathrm{p}}^2}{\omega^2 + i\gamma\omega} , \tag{8.7}$$

where $\omega_{\mathrm{p}}^2 = ne^2/\epsilon_0 m$ is the plasma frequency of a bulk plasmon (n = electron density, m = electron mass). Damping and scattering processes are included into the discription by the imaginary part of the dielectric function, see the discussion in Section 10.3 for details. The damping constant γ is typically in the order of $\gamma \sim 100\,\mathrm{THz}$ at room temperature, which corresponds to a relaxation time of $\sim 10\,\mathrm{fs}$. For gold $\hbar\omega_{\mathrm{p}} \approx 9\,\mathrm{eV}$ and, thus, $\mathrm{Re}[\epsilon_{\mathrm{Au}}(\omega)] < 0$ in the telecom wavelength regime. Note that Eq. (8.7) neglects the residual polarization caused by the background of ion cores and, furthermore, the onset of interband transitions at $\approx 2\,\mathrm{eV}$ is not included. See Ref. [181], pp. 11-14 for details. Equation (8.7) sufficiently approximates the complex dielectric function of gold in the telecom wavelength regime. However, for calculations and for the transfer-matrix simulations performed in the context of this thesis, literature data for $\epsilon_{\mathrm{Au}}(\omega)$ is used [183]. This data is presented in Fig. 8.2.

The real part of the dielectric function of gold is negative up to $\approx 6\,\mathrm{eV}$, which is far below the photon energies utilized in the experiments in this thesis. Therefore, the condition resulting from Eq. (8.5) is fulfilled. Inserting ϵ_{air} and $\epsilon_{\mathrm{Au}}(\omega)$ in Eq. (8.6) leads to the central

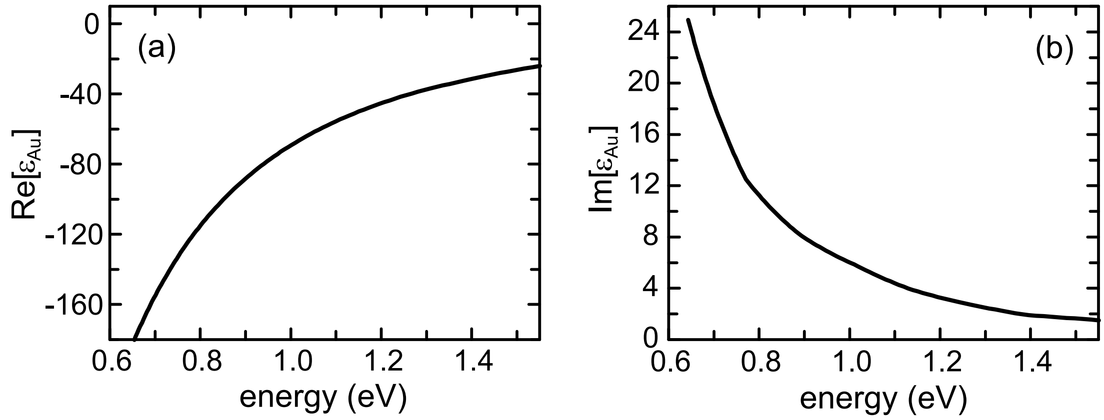

Fig. 8.2: (a) Real and (b) imaginary part of the dielectric function of gold. The data presented here are linear interpolations to data taken from Ref. [183].

result of this chaper, which is the frequency-dependent SPP wave vector at a gold-air interface:

$$k_{\mathrm{SPP}}(\omega) = k_0\sqrt{\frac{\epsilon_{\mathrm{Au}}(\omega)}{1+\epsilon_{\mathrm{Au}}(\omega)}} \ . \tag{8.8}$$

Here, $k_0 = \omega/c = 2\pi/\lambda$ is the free-space wave vector of light. It is important to notice that $k_{\mathrm{SPP}} > k_0$ at a given frequency ω. This finding can be associated with the binding of the SPP to the metal surface. In the next paragraph, the implications of this dispersion for the excitation of SPP modes with free-space radiation are discussed.

Launching SPPs using an external light source is the core of the experiments performed in the ensuing chapters. Since SPPs are excited states, energy needs to be added to the system to generate them. Coupling light that is incident on the gold-air interface to a SPP mode requires the conversation of momentum and energy, in order to transfer them both from photons to SPPs. Fig. 8.3 displays the SPP's dispersion relation $k_{\mathrm{SPP}}(\omega)$ according to Eqs. (8.7) and (8.8) together with the dispersion of light in air $\omega = c_{\mathrm{air}}k_0$. It is convenient to think of the simultaneous matching of energy and momentum as a crossing of the two dispersion lines. Since the wave vector of the SPP is larger then that of light for any given frequency, the lines never cross. In other words, photons in air do not provide enough momentum to excite surface plasmon polaritons. Moreover, the quantities that need to be considered here are the component of the light's wave vector that is parallel to the interface $k_{0,x}$ and k_{SPP} (which is intrinsically parallel to the interface). Naturally, the in-plane component $k_{0,x} \leq k_0$.

Considering the photon energies used in the following chapters, the relative deviation of the momenta $(k_{\mathrm{SPP}} - k_0)/k_0$ is in the range of 0.4 % to 1.6 %. The SPPs, therefore, mainly have photonic character and can be seen as light guided along the interface.

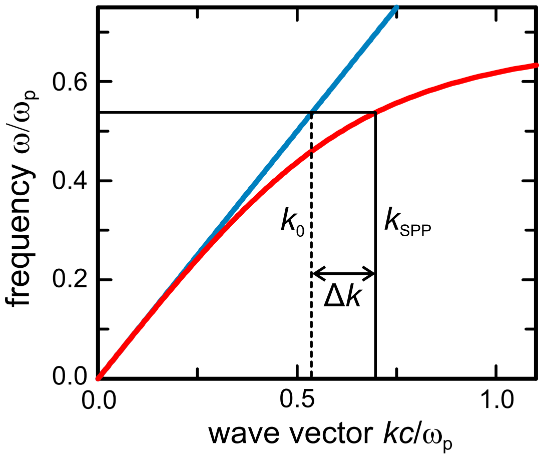

Fig. 8.3: Dispersion relation of a SPP at a gold-air interface (inverse function of Eq.(8.8), red curve) and the dispersion of light in air $\omega = c_{\mathrm{air}}k_0$ (blue curve) . At a given frequency, a momentum mismatch Δk prevents the direct excitation of SPPs using an external light source.

The momentum mismatch restricts the launching of SPPs using light at a planar gold-air interface. Consequently, it also hinders the reverse process, meaning that SPPs cannot radiate into free space via the emission of photons and are bound to the dielectric-metal interface. To overcome the momentum mismatch $\Delta k = k_{0,x} - k_{\mathrm{SPP}}$ and achieve coupling, different methods can be applied, which, simply put, rely on an alteration of the light's dispersion/momentum.

Two of the most commonly employed methods and their combination with VO_2-NCs are examined in this thesis. Details on how the light-SPP coupling is accomplished will be given in the respective Chapters 9 and 10. Two sample configurations employing different methods of changing the momentum of the incident photons are utilized: (i) Grating-assisted launching of SPPs utilizes the alteration of the light's momentum in a spatially periodic structure. By making use of the MIT in VO_2-based pre-defined diffraction gratings, a switchable SPP launcher is demonstrated, see Chapter 9. (ii) In the Kretschmann configuration, the momentum of free-space light is enhanced in a dielectric and the evanescent field created at a total internal refraction launches SPPs. The MIT in a VO_2 layer in the near field of these SPPs markedly changes the coupling conditions, see Chapter 10.

To provide the basis for understanding the mechanisms and results presented later in this manuscript, it is useful to look at quantities that characterize the spatial extension and the propagation of the SPP mode. Equation (8.8) also holds true for a complex dielectric function $\epsilon_{\mathrm{Au}}(\omega) = \epsilon'_{\mathrm{Au}}(\omega) + i\epsilon''_{\mathrm{Au}}(\omega)$. The imaginary part $\epsilon''_{\mathrm{Au}}(\omega)$, which is necessary to describe the gold layers examined in this thesis, is connected to the damping of the electron plasma and to the absorption of electromagnetic radiation in the metal. As a result, $k_{\mathrm{SPP}}(\omega)$ features an imaginary part that leads to an exponential decay of the SPP's amplitude along the direction of propagation E_x described by a length

$$d_x = \frac{1}{2 \cdot \mathrm{Im}(k_{\mathrm{SPP}})} \ . \tag{8.9}$$

Taking literature data for the dielectric function of gold [183], one finds $d_x \approx 200\,\mu\mathrm{m}$ at a wavelength of $1.55\,\mu\mathrm{m}$. The quantity d_x specifies the x-distance to the point of excitation at which the field amplitude drops to $1/e \approx 37\%$ of the initial value.

Another important quantity is the penetration depth of the SPP's electric field into the surrounding media which is determined by an exponential decay $\exp(-\kappa_i|z|)$. Considering the fact that an additional VO_2-based layer in the vicinity of the gold-air interface is supposed to strongly alter the light-SPP coupling, it is useful to know just how close this vicinity has to be. After rewriting Eq. (8.4), one ends up with an attenuation length given by

$$d_{z,i} = \frac{1}{\kappa_i} = \left(k_0 \sqrt{\frac{-\epsilon_i^2}{\epsilon_1 + \epsilon_2}} \right)^{-1} \ , \tag{8.10}$$

resulting in $d_{z,2} \approx 25\,\text{nm}$ in gold and $d_{z,1} \approx 2.4\,\mu\text{m}$ in air for $\lambda = 1.55\,\mu\text{m}$ light. On the dielectric side of the interface, the electric field is spread over a length scale similar to the wavelength of the exciting light. In contrast, the SPP mode is strongly concentrated to sub-wavelength dimensions on the metallic side. This spatial confinement opens up the possibility to guide light along structures smaller than the optical diffraction limit [24].

The following chapters elucidate how the design of the examined specimen, the phase transition in VO_2-NCs and the penetration depths of the SPP mode combine to facilitate the implementation of VO_2-based active plasmonic devices.

8.3 Experimental Setup for the Excitation and Detection of SPPs

Before moving on to the demonstration of VO_2-based plasmonic devices, the setup used for most of the experiments in following chapters is presented. Both the grating-assisted coupling and the Kretschmann configuration require a similar approach. In the experimental realization of both methods, the detection of the light-induced launching of SPPs relies on the fact that energy is transferred from light to SPPs once the coupling is established. Essentially, the change in the intensity of the transmission or reflection of light is used to analyze the light-SPP coupling. The phase of the VO_2-NCs can be controlled thermally or optically. The following text and Fig. 8.4 give a brief overview of the setup. Additional information is given in the respective sections, if needed to fully understand the experimental methods or the results.

A probe laser beam (red line) with a mixed polarization state (TM + TE) is focused onto the sample. It is used to analyze the light-SPP coupling by launching SPPs at the gold-air interface, if the conditions are met. Polarization optics allow to control the relative composition of the two components. The most frequently used probe light source is a commercial Er:fiber laser (Toptica FFS, see Ref. [184]) emitting at a central wavelength of $1.55\,\mu\text{m}$ ($\hbar\omega = 0.8\,\text{eV}$). In addition, a home-built titanium:sapphire laser (TiSa) and the optical parametric amplifier (OPA, introduced in Section 4.2) are made use of. The output wavelength of these sources is tunable. While the OPA is used for different central wavelengths specified later in the text, the TiSa is only used at $0.905\,\mu\text{m}$ ($\hbar\omega = 1.37\,\text{eV}$).

In parts of the experiments, an additional pump laser beam (blue line) is utilized to optically induce the phase transition. A commercial green cw 532 nm (2.3 eV) laser diode is frequently used during the alignment of the setup to quickly generate the MIT. A combination of OPA probe pulses and frequency-doubled RegA (regenerative amplifier) pump pulses obtained from the same laser system is utilized for time resolved pump-probe measurements. The RegA output is frequency-doubled to $\lambda = 405\,\text{nm}$ ($\hbar\omega = 3.06\,\text{eV}$) using the second harmonic generation (SGH) in a beta barium borate (BBO) crystal . Although all probe light sources emit pulsed light, they are not used for time-resolved measurements, except for the pump-probe experiments presented in Section 9.4. Other than that, their output can be considered as continuous probe radiation[1].

As will be thoroughly explained in the following sections of the text, the above-mentioned methods of enabling the light-SPP coupling utilize the angle of incidence of the exciting light to adjust the light's in-plane wave vector $k_{0,x}$ such that it matches k_{SPP}. Consequently, at a given photon energy, varying the angle of incidence provides the means to see signatures of light-SPP coupling. More specifically, the angular dependence of the transmission or reflection of light are analyzed. In the experiment, two goniometer stages allow to independently tune the angle of incidence and the angle of detection. By turning the detector section, either the transmission through the sample, the diffracted light created by a VO_2-based grating or the reflection from the sample can be collected. The samples are mounted on a temperature controlled holder, consisting of two stacked Peltier elements and a sample holder made of copper. The stages and the holder are movable in all spatial directions.

Since the magnitude of k_{SPP} and, consequently, the angular position of light-SPP coupling depends on the wavelength of the exciting light, an overly broad spectrum would lead to an unwanted smearing out of the resonances. To ensure a good spectral resolution, all probe light sources are combined with different optical bandpasses that narrow the output spectrum. The beam is loosely focused to a $\approx 100\,\mu\mathrm{m}$ spot (FWHM) using a lens with 125 mm focal length, which is chosen in trade-off between gaining sufficient lateral spatial resolution on the sample surface and preserving a good angular resolution ($\approx 1^\circ$).

In order to be able to see even minor alterations of the optical signals related to surface plasmon effects, the detector section features a polarizing beam splitter cube (PBSC) that redirects the polarization components. This spatial separation is beneficial because the light-SPP coupling is only possible for TM radiation. Simultaneously measuring both polarizations enhances the sensitivity of the detection to SPP-related effects. The detection is completed by InGaAs photodiodes and lock-in amplifier(s) (Stanford Research 830) referenced to either the probe or pump radiation, which are modulated by optical chopper wheels. In some experiments, the differential input of the lock-in amplifier(s) is used to form the signal TM-TE. Optical filters block pump radiation or attenuate the probe intensity, if necessary. Both goniometer stages as well as the lock-in amplifier(s) are controlled and read out using a computer and home-built software based on LabView.

---

[1] The use of pulsed optical sources is simply owed to the availability in the lab. Er:fiber laser: 90 MHz repetition rate, 100 fs pulse length. TiSa: 90 MHz repetition rate, ~,40 fs-60 fs pulse length [185]. Since the probe irradiance is kept low and the combination with optical band passes leads to a temporal broadening of the pulses, nonlinear optical effects generated by the probe radiation are negligible.

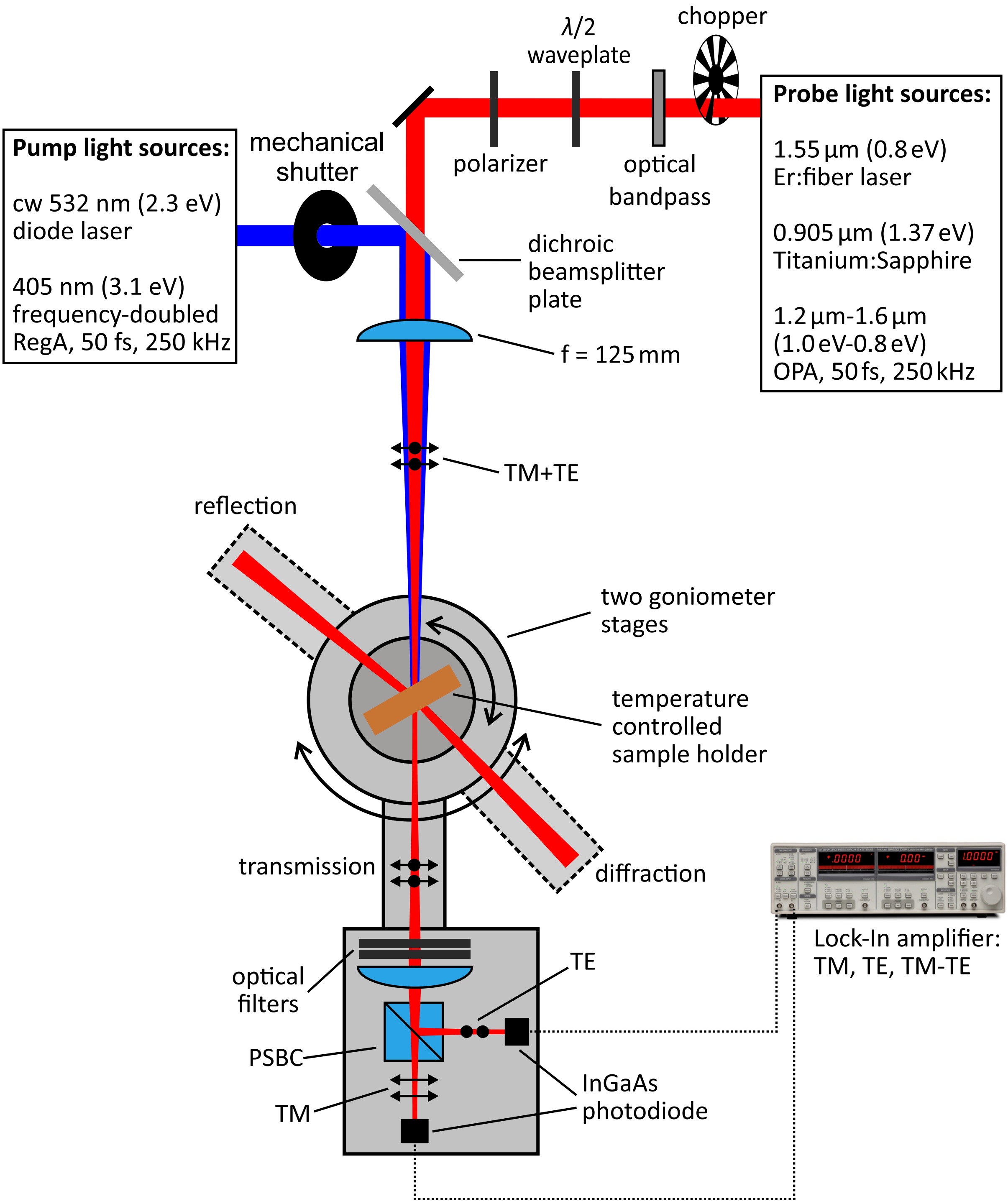

Fig. 8.4: Sketch of the basic experimental setup used for most of the experiments presented in this part of the thesis. Multiple probe and pump light sources can be utilized to monitor the phase transition in VO_2-NCs and its influence on the light-SPP coupling in different sample configurations. See the text of Section 8.3 for details.

Chapter 9

Switchable Plasmonic Grating Couplers

The controlled manipulation of the light-SPP coupling strength by external means is a key objective of research in the field of active plasmonics. Ultimately, the encoding of digital bits into the propagation of SPPs is needed to use plasmonic structures for the transfer of digital information. In this chapter, it is shown how gold-covered diffraction gratings based on site-selective deactivation of the MIT in VO_2-NCs act as switchable SPP launchers with a giant switching contrast. First, the concept of coupling light to SPPs by adding a diffractive functionality to the metal-dielectric interface is explained. Next, the combination of this method with VO_2-based switchable diffraction gratings and results on the active control of light-SPP coupling in these structures are presented. The guiding idea is to bring a pre-defined grating layer of VO_2-NCs into the near field of SPP modes at an unstructured gold-air interface and, thereby, transfer the switching contrast of the diffractive functionality to the light-SPP coupling. Finally, the capability of ultrafast optical plasmonic switching is addressed.

Parts of the results presented in this chapter have already been published in Ref. [25].

9.1 Grating-Assisted Light-SPP Coupling

This section gives a brief explanation and illustration of the grating-assisted launching of SPPs. It is evident from the dispersion relations Eq. (8.8) and Fig. 8.3 that the momenta of SPPs at a gold-air interface and light, which is incident from the air side of the interface, are different. Hence, the light-induced excitation of an SPP of a certain energy $\hbar\omega$ is prohibited, unless the photon momentum $k_{0,x}$ is increased and matched to k_{SPP} (all momenta are considered parallel to interface). One of the most commonly applied ways to achieve this momentum matching is the grating-assisted light-SPP coupling. In short, the momentum of light is changed by the interaction with a grating such that it matches the SPP. This method was discovered in the late 1960s by assigning anomalies in the diffraction of TM-polarized light at a metallic grating to the excitation of surface plasmons [186–188].

As already discussed in Section 7.2, a diffraction grating relies on the spatially periodic

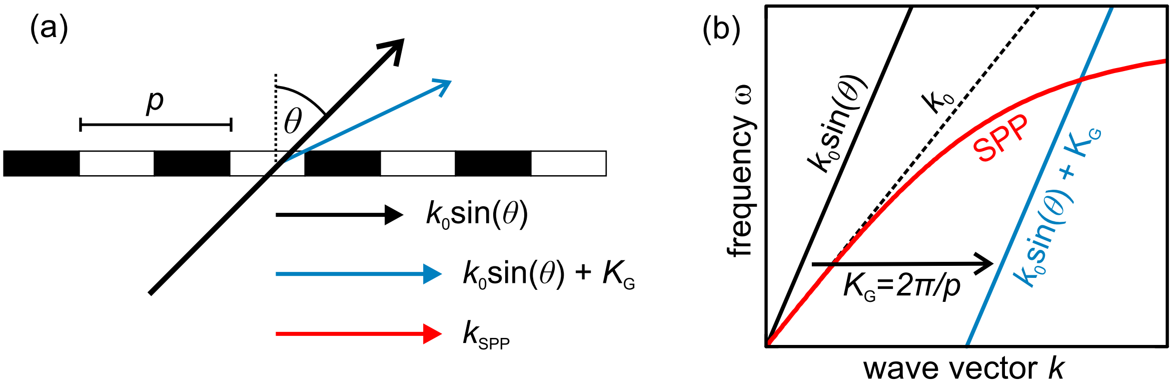

Fig. 9.1: (a) The guiding idea behind the grating-assisted coupling of light and SPPs: The in-plane wave vector of light is changed by the periodicity of the grating. At a certain angle of incidence θ the momentum matching condition $k_0 \sin(\theta) + K_\mathrm{G} = k_\mathrm{SPP}$ is fulfilled. (b) Schematic representation using the dispersion relations of light and SPP. The in-plane component (black line) of photons in air (black dashed line) is increased by K_G upon interaction with the grating (blue line).

alteration of the amplitude or the phase of light. Diffracted orders of light leave the grating under an altered angle of propagation compared to the initial angle of incidence. In terms of wave vectors, this effect is equal to a change of the wave vector component in the plane of the grating (while the component perpendicular to the grating plane remains unchanged). It is straightforward to quantify this change and write the in-plane wave vector of the m-th order of diffraction as

$$k_m = k_{0,x} + mK_\mathrm{G} \tag{9.1}$$

where $m = \ldots, -2, -1, 0, 1, 2, \ldots$ reflects the order (and direction) of diffraction and $K_\mathrm{G} = 2\pi/p$ is a wave vector connected to the grating's periodicity p.

The idea of using a grating to achieve light-SPP coupling is illustrated in Fig. 9.1(a). It relies on the fact that at some angle of incidence θ, the momenta of light and SPP are matched when condition $k_\mathrm{SPP} = k_m$ is fulfilled. In Fig. 9.1 and in the remainder of this thesis, only the first order of diffraction is considered, i.e. $m = 1$. From the geometry of this configuration follows $k_{0,x} = k_0 \sin(\theta)$ and the coupling condition now reads

$$k_\mathrm{SPP} = k_0 \sin\theta + K_\mathrm{G}\ . \tag{9.2}$$

The principle of grating-assisted SPP coupling can also be understood as a shift of the light's dispersion to higher wave vectors, as is depticted in Fig. 9.1(b). The point of the crossing of the two dispersions is determined by the periodicity p, the angle θ and the given energy $\hbar\omega$. Following a different point of view, the introduction of a spatially periodic structure to the metal-dielectric interface leads to the introduction of a Brillouin zone for the SPP wave vector, which is then restricted to $k = \pi/p = K_G/2$. In a more descriptive picture, the SPPs dispersion is folded back at a vertical line located at $K_G/2$.

This approach is completely equivalent to the scheme presented here, as it corresponds to $k_{\mathrm{SPP}} - mK_{\mathrm{G}} = k_0 \sin\theta$.

Following the Eqs. (8.8) and (9.2), the launching of SPPs using light with a wavelength λ at a gold-air interface is expected to happen at an angle of

$$\theta_{\mathrm{SPP}} = \arcsin\left(\sqrt{\frac{\epsilon_{\mathrm{Au}}}{1+\epsilon_{\mathrm{Au}}}} - \frac{\lambda}{p}\right) . \tag{9.3}$$

The efficiency of grating coupling is mainly defined by (but is not necessarily equal to) the diffraction efficiency of the related grating structure since this quantity is connected to the fraction of incident light that experiences a change in the wave vector. Using pre-defined gratings, such as periodically height-modulated metal interfaces [159] or additional grating overlayers [189], coupling efficiencies $> 50\%$ can be achieved. Note that, in principle, any rough surfaces can provide additional momentum and help launching SPPs, since it can be expressed of a Fourier-type composition of gratings [188; 190].

9.2 Characterization of VO_2-Based Pre-Defined Gratings

In Chapter 7, the principles of diffraction gratings utilizing the different dielectric functions of the two phases of VO_2 are outlined. Zimmer et al. demontrate pre-defined thermochromic gratings in an otherwise unstructured VO_2-NC layer [87], which are utilized in this chapter for the grating-assisted launching of SPPs. The underlying concept is a deactivation of the MIT using site-selective argon ion bombardment that is discussed in Sections 6.4 and 7.2.

For the aim of creating plasmonic grating couplers, the procedure of selective deactivation is applied to 500 µm×500 µm areas of an otherwise unstructured sample. Diffraction gratings with different periodicity p and duty cycles a/p are formed using a stripe-patterned chromium mask. The quantities p and a are visualized in Fig. 9.2. The different gratings comprise periodicities $p = 1.5\,\mu\mathrm{m}$, $2.0\,\mu\mathrm{m}$, $2.5\,\mu\mathrm{m}$, $3.0\,\mu\mathrm{m}$ and duty cycles a/p between 0.17 and 0.6. Before moving on to the demonstration of plasmonic couplers in Section 9.3,

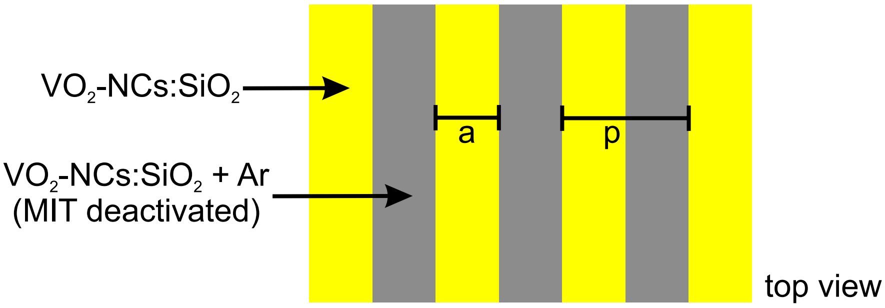

Fig. 9.2: Schematic top view of a grating defined by selective deactivation of the MIT using argon bombardment. The periodicity p and the duty cycle a/p are illustrated. Grey: deactivated areas (MIT is inhibited). Yellow: as-grown areas (NCs are able to undergo the MIT).

the diffractive functionality of these gratings is tested.

The investigation of the pre-defined gratings starts by characterizing their diffraction efficiency and switching contrast. Fig. 8.4 shows a sketch of the experimental setup that is used for this purpose and for most of the experiments presented later in this chapter. The samples are mounted on a temperature-controlled holder. Two goniometer stages allow to independently tune the angle of incidence and the detection angle. As a light source, the Er:fiber laser (Toptica FFS) is used. An optical bandpass centered at 1.55 µm (0.8 eV) narrows the output spectrum to 15 nm (FWHM).

The intensity of the first order diffraction is plotted in Fig. 9.3 for various sample temperatures during a heating and cooling cycle, normalized to the intensity of the transmission at 10°C sample temperature. The data is recorded for TM polarized light at normal incidence on a grating with $p = 3.0\,\mu\text{m}$ and $a = 1.5\,\mu\text{m}$. Below the critical temperature T_C, all NCs are in the insulating state. A small diffracted signal is seen, reflecting the residual dielectric contrast between Ar-exposed and as-grown NCs.

Upon heating, the steep rise of the signal at $T_C \approx 90°\text{C}$ is caused by the thermally induced MIT. Above T_C, only the as-grown areas (not deactivated) switch into the metallic phase, and the alternating areas of insulating (deactivated) and metallic VO_2-NCs act as a diffraction grating. The spatial distribution of insulating and metallic NCs is now similar to the one obtained using the optical inscription of diffraction gratings discussed in Section 7.3. The maximum diffraction efficiency of the $p = 3.0\,\mu\text{m}$ grating investigated here is $\approx 3.2 \cdot 10^{-3}$. This a factor of ≈ 2 higher when compared to the gratings presented in Section 7.3 (optically defined or pre-defined). This increase might be explained by an improved fabrication quality and the higher number of illuminated gratings slits.

While cooling the sample, the supercooled metallic phase persists down to $\sim 40°\text{C}$. Note that the diffraction efficiency slightly increases during the cooling cycle. This behavior was

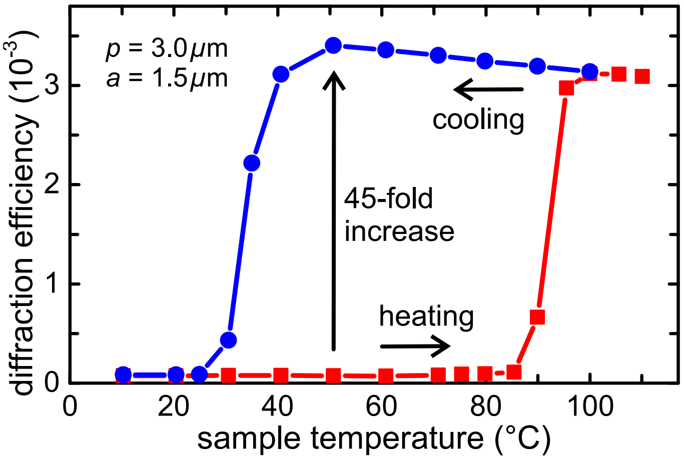

Fig. 9.3: First order diffraction efficiency of $\lambda = 1.55\,\mu\text{m}$ light at normal incidence for various sample temperatures during heating (red squares) and cooling cycles (blue circles).

also found in Ref. [87] and might be related to Ar-exposed NCs, in which the MIT is not completely deactivated. Such NCs are most likely to be to be found at the edges of the chrome stripes. These NCs could switch into the metallic phase at high temperatures, whereby the dielectric contrast does not reach its maximum possible quality. Upon cooling, these NCs switch back to the insulating phase at a higher temperature compared to the as-grown NCs. The maximum dielectric contrast of the grating structure is reached at this point in the heating/cooling cycle.

When the temperature is reduced further, the all NCs switch back into the insulating phase. As a consequence, the dielectric contrast vanishes and the diffraction efficiency approaches its initial value again. The marked thermal hysteresis of the the first order phase transition can be attributed to good crystallinity of the single-domain NCs, as well as to the surrounding SiO_2 matrix (see Section 6.3).

Note that although switchable diffraction was found for all grating periods and duty cycles, the following investigations mainly focus on $p = 2.5\,\mu m$ and $p = 3.0\,\mu m$ gratings with duty cycles near 0.5. Gratings with smaller periods or small duty cycles show a markedly reduced diffraction efficiency. This topic will be addressed in more detail below.

Remarkably, the almost complete absence of dielectric contrast between the as-grown and deactivated NCs in the insulating phase generates a substantial switching contrast. In the supercooled metallic phase, the diffraction efficiency exceeds that of the insulating phase by a factor of ≈ 45. With this validation of the switching abilities of the fabricated gratings, the focus of is now shifted to the demonstration of plasmonic devices that are capable of strongly modifying the light-SPP coupling.

9.3 Demonstration of VO_2-Based Switchable Plasmonic Grating Couplers

To enable the plasmonic functionality of the pre-defined VO_2-based gratings, a 2 nm titanium adhesion layer and a nominally 25 nm thick homogeneous gold layer are deposited on top of the sample surface close to the grating. Surface plasmon polariton modes are now supported at the gold-air interface. As is illustrated in Fig. 9.4, the thin metal film and the low damping in the SiO_2 substrate (similar to air) ensure an overlap of the SPP mode with the grating layer. In the gold layer, the field strength is damped to $\approx 1/e$ of its initial value, cf. Eq. (8.10).

In order to detect the excitation of SPPs by the incident light, the following method is employed: whenever the coupling condition (9.2) is fulfilled, energy is transferred from TM polarized light to SPP modes and the intensity of the transmitted light decreases. Hence, by investigating the angular dependence of the optical transmission, a signature of SPP launching is expected to be seen as a decrease in the signal strength at an angle given by

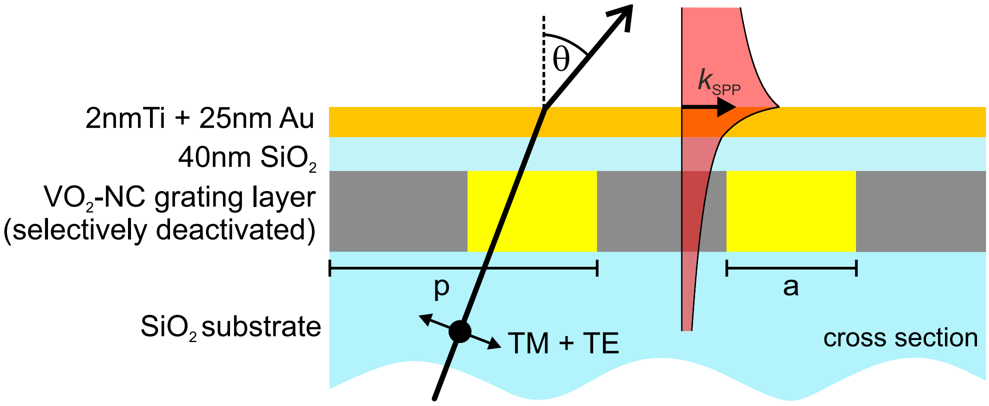

Fig. 9.4: Schematic cross-section of a gold covered VO$_2$-NC sample featuring alternating stripes of deactivated and as-grown NCs. The read area illustrates the field distribution ($E_x(z)$) of surface plasmon polaritons, launched by the TM polarized part of $\lambda = 1.55\,\mu$m light (black line). In order to detect the launch of SPPs, the transmission is measured for varying angle of incidence θ.

Eq. (9.3). The experimental realization of this method is based on the setup depicted in Fig. 8.4 on page 88 using the above-mentioned Er:fiber laser at 1.55 µm central wavelength. Probe light is incident on the substrate side of the sample. The angle of incidence θ at the gold-air interface is changed by turning the goniometers. Considering the fact that light-SPP coupling is only possible for TM polarized light, the difference in the transmissivity of TM and TE polarized light is measured using the differential input of the lock-in amplifier. Effects that equally influence both polarization components do not contribute to this differential signal. Laser noise and, more importantly, the increased absorption of the metallic VO$_2$-NCs are removed. Using the polarization optics, the relative fractions of TM and TE polarized light in the probe signal is adjusted such that the differential signal is zero when no plasmonic effects are present.

Fig. 9.5(a) shows the angular dependence of the difference of TM and TE transmissivity in the insulating and metallic phase. The sample temperature is adjusted to 50°C for both phases. By heating the sample to 105°C and subsequently cooling it down to 50°C, the VO$_2$-NCs are switched into the supercooled metallic phase. Performing this procedure ensures that the influence of the MIT is separated from any other thermal effects in the sample, like a temperature-induced change of a dielectric function of gold or SiO$_2$. Owing to the different angular dependences of the reflectivities of TM and TE polarized light at the various interfaces, the signals in Fig. 9.5(a) show an overall slope. This slope is different for insulating and metallic VO$_2$ because of the different refractive index of the two phases.

More importantly, a distinct signature of SPP launching is evident as a dip in the signal centered at $\theta \approx 23°$. When the grating in the VO$_2$-NC layer is activated by switching into the metallic phase, the coupling condition (9.2) is fulfilled. The sub-wavelength proximity of the gold-air interface to the grating layer ensures a spatial overlap with the SPP modes.

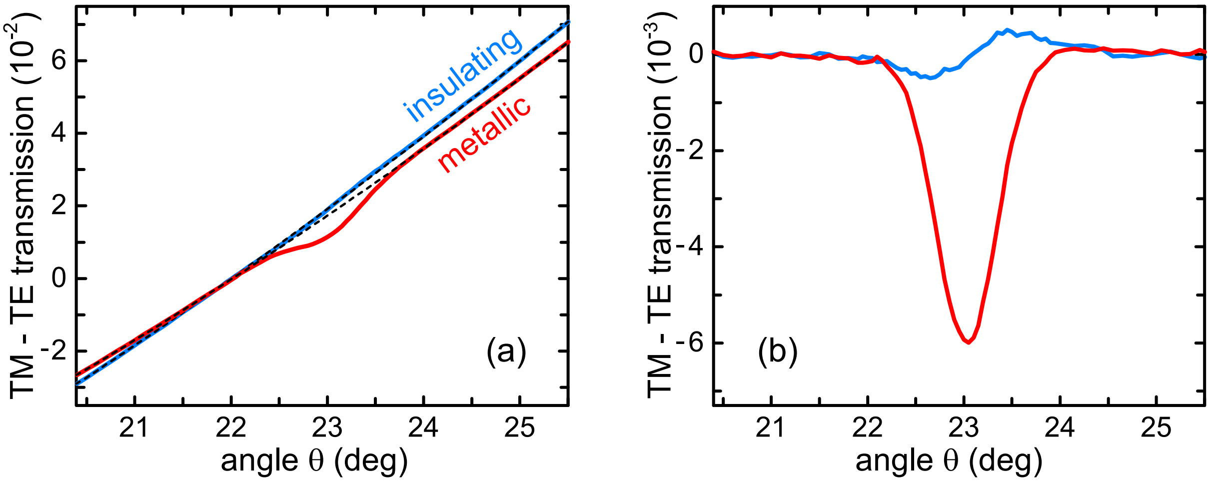

Fig. 9.5: (a) Difference of TM and TE polarized transmission through a gold-covered VO_2-NC grating for insulating (blue) and metallic (red) NCs in the as-grown areas. The grating parameters are $p = 2.5\,\mu m$ and $a = 1.37\,\mu m$. Dashed lines are parabolic fit to the background signals. (b) Background-corrected differential transmission data (a parabolic fit is subtracted from data in panel (a)).

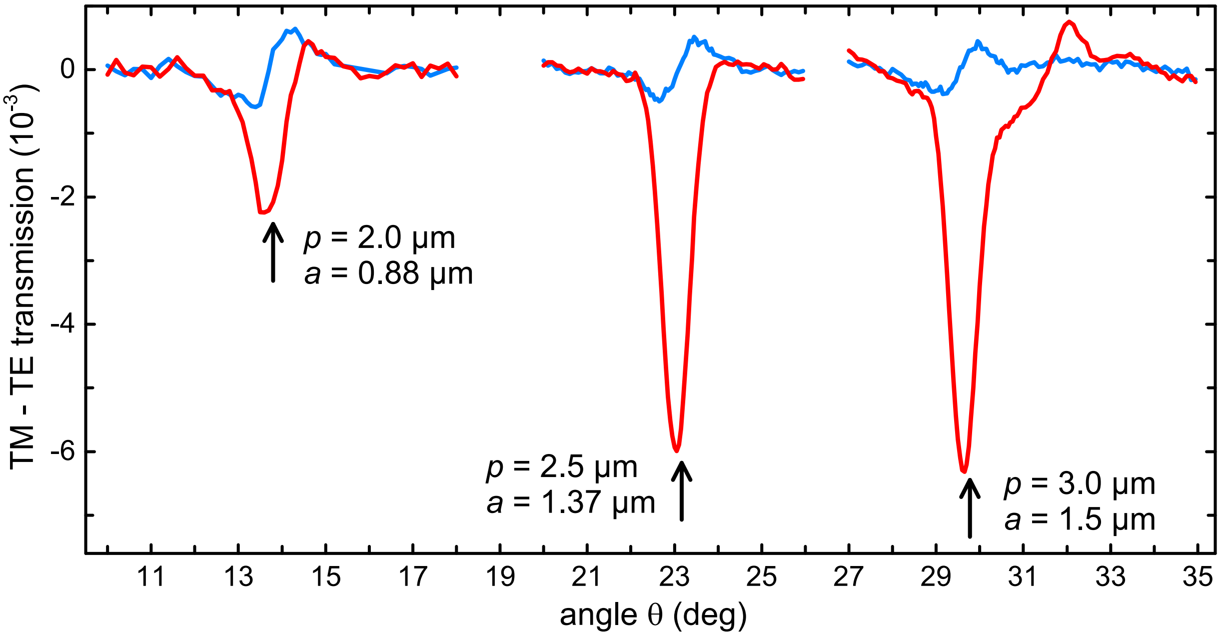

Fig. 9.6: Background-corrected differential transmission data for different grating periods p for insulating (blue) and metallic (red) VO_2-NCs in the as-grown areas. The vertical arrows mark the expected SPP resonance position calculated with Eq. (9.3).

As a result, a fraction of the TM polarized part of the incident light is converted to SPPs and, thus, the differential transmission decreases. The launching of SPPs is clearly seen in Fig. 9.5(b), where the background slope is subtracted employing a parabolic fit to data outside of the plasmonic resonance. The peak coupling efficiency of the SPP launching, defined by the fraction of missing TM polarized light, is $\approx 0.6\,\%$, which is in the order of the diffraction efficiency of the grating layer seen in Fig. 9.3.

To further corroborate our interpretation and confirm that the signals arise from thermochromic SPP resonances, two additional steps are performed: (i) The experiments are repeated for additional samples with different grating periods. (ii) A calculation of the SPP resonance angle is carried out, using Eq. (9.3) and literature data for the dielectric function of SiO_2 [191], gold [183] and air [182]. The results of these steps can be found in Fig. 9.6, where background-corrected transmissivity signals are presented together with calculated resonance positions (vertical arrows). As expected, the resonance angle strongly shifts with the gratings period. From the good agreement of the experimentally observed minimum of the dip in the data with the calculated angles, it can be concluded that the thermally induced MIT indeed leads to the launching of SPPs at the gold-air interface.

Influence of Fabrication Quality and Duty Cycle

One degree of freedom in the design of gratings fabricated by the selective deactivation procedure is the duty cycle a/p. This paragraph will address the influence of the gratings quality and the duty cycle on the diffraction and SPP coupling efficiency. As mentioned earlier, gratings with $p \leq 2.0\,\mu\text{m}$ show a reduced diffraction efficiency compared to larger periods, which can mainly be attributed to the reduced fabrication quality. This behavior translates into the grating-induced light-SPP coupling as a drop of the efficiency by a factor of ≈ 3 for $p = 2.0\,\mu\text{m}$ compared to $p \geq 2.5\,\mu\text{m}$, cf. Fig. 9.6. Furthermore, no SPP launching was detected for $p = 1.5\,\mu\text{m}$.

The data presented so far was taken with samples where a/p is close to 0.5. This configuration yields the largest diffraction and coupling efficiency, as is evident from the data presented in Fig. 9.7. Here, the efficiencies are presented for two different grating periods and multiple duty cycles a/p. The strength of light-SPP coupling and the diffraction efficiency show a similar dependence on the duty cycle, but drop for small duty cycles. This might be explained by the detriment of very narrow chrome stripes during the fabrication. Furthermore, there is a noticeable feature in the two data points for $p = 2.5\,\mu\text{m}$ and $a/p = 0.42$ or 0.40, respectively: a minor modification of the duty cycle results a twofold reduction of the efficiency, which points towards the quality of the grating being the major influence in this case. Optical microscope pictures of the chromium mask confirm occasional problems during the lift-off process.

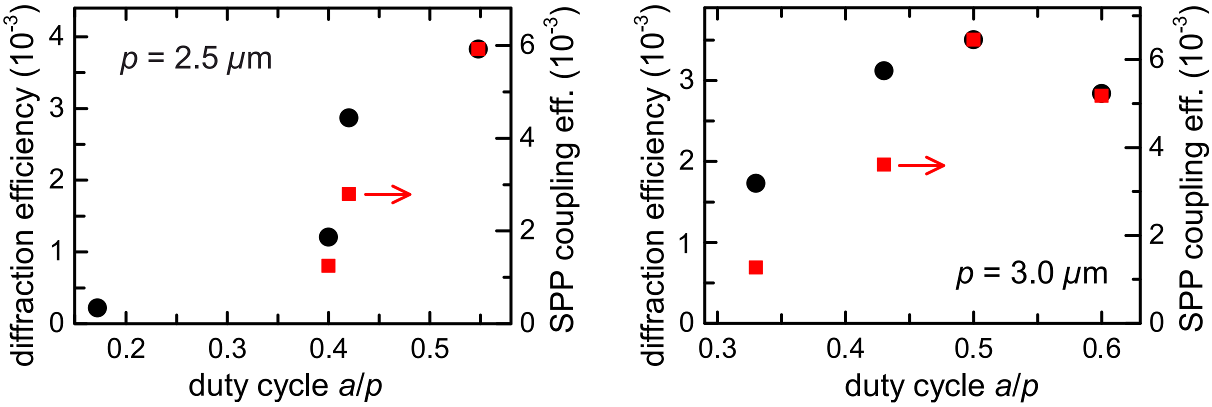

Fig. 9.7: Effect of different duty cycles a/p on the first order diffraction efficiency (black circles) and the light-SPP coupling efficiency (red squares) for different grating periods.

Plasmonic Switching Contrast

The thermally-induced MIT leads to a strong modification of the light-SPP coupling in the pre-defined VO$_2$-based nanocomposite. When the VO$_2$-NCs are in the insulating phase, only a minor dispersive feature is seen, which is probably caused by the residual dielectric contrast between Ar-exposed and as-grown NCs (cf. blue curves in Fig. 9.5 and Fig. 9.6). While scanning the angle of incidence, the differential transmission signal TM - TE shows a sign change with a reversal point just at the position of the plasmonic resonance.

Such a feature might be related to a Fano resonance [192]. In general, this type resonance is caused by the interference of a broad, slowly-varying excitation path and a resonant, narrow or discrete one. In plasmonics, this phenomenon can occur as an interference of transmitted or reflected light (i.e. scattering into a continuum of states) with light that is re-emitted from excited localized plasmons or SPPs [193–195]. Depending on the relative strength of the two processes and a phase change of the re-emitted light, a Fano resonance shows line shapes ranging from strongly asymmetric to Lorentzian. In the present case, the excited SPP modes can re-radiate into the far field via the inverse process of grating-assisted light-SPP coupling [94; 181]. The differential transmission of TM and TE polarized light is highly sensitive to a change in the intensity of one component. Hence, it is reasonable to assume that a constructive or destructive interference of the TM component with even a small amount of re-emitted light field shows up in the signal. When the VO$_2$-NCs are switched to the metallic phase and the grating is activated, the energy transfer TM→SPP and the damping of the SPPs in the metallic NCs presumably dominate this re-emission.

The dispersive feature in the insulating phase cannot unambiguously be attributed to the launching of SPPs, given the sensitivity of the experiment. Moreover, the differential signal in the insulating phase is close to zero at the angle of the resonance. It does not seem appropriate to define a quantitative switching contrast of the plasmonic grating couplers, as done with to the switching contrast of the underlying diffraction grating. The data presented in Fig. 9.6 suggests that the activation of the grating layer leads to the dominant light-SPP coupling in the first place. Therefore, the MIT-induced effect can be considered as a full on-off modulation of the light-induced launching of SPPs.

9.4 Temporal Dynamics of the Optical Activation of Pre-Defined Gratings

The MIT can be induced optically, potentially on sub-ps time scales, as discussed in Section 7.1. During the experiments performed in the context of this chapter, this fact is exploited in several ways.

The active control over SPP launching is also achieved using an optically induced MIT, instead of a purely thermal activation. For this purpose, a cw 532 nm pump light source is utilized (see the experimental setup on page 88). Commercial, low-cost cw 532 nm laser diodes can be used to rapidly induce the MIT in the VO_2-NC gratings, similar to the experiments presented in Chapter 7. The (as-grown) NCs in the probed sample area illuminated by the $\approx 100\,\mu m$ wide probe light spot are switched to the metallic phase using a short-time pump light exposure (~ 1 ms-10 ms) with ~ 100 mW average power. Depending on the overall sample temperature, the plasmonic coupler either switches into the long-time stable supercooled metallic phase or relaxes back to the insulating phase after the photoexcitation. In the given experimental configuration using a gold-covered VO_2-NC sample, this relaxation takes ~ 10 ms-100 ms. This time scale stems from the large heat capacity of the sample and the thermal hysteresis of the VO_2-NCs.

In order to explore the limits of ultrafast plasmonic switching, pump-probe measurements are performed using the output of a frequency-doubled regenerative amplifier (RegA) at 405 nm as pump pulses and the OPA output at 1.55 µm as probe pulses.The pump wavelength of 405 nm ($\hbar\omega = 3.06\,eV$) is chosen because the absorption of light by VO_2-NCs in the insulating phase shows a 10-fold enhancement at this wavelength compared to the readily available 810 nm or 1.55 µm pulses. Accordingly, the average pump power required to induce the phase transition is expected to be reduced. For an introduction to the pump-probe technique the reader may refer to Section 4.2.

As a practical test of the ability to modify the light-SPP coupling on ultrashort timescales in the present specimen, the pump-induced change to the diffraction efficiency of the VO_2-based gratings is examined in the following. The experimental configuration is sketched in Fig. 9.8. Pump and probe pulses are incident on the substrate side of the sample. They co-propagate through the fused silica and overlap in the area of the gold-covered VO_2-NC gratings. The diameter of the pump beam is chosen to be larger than the probe spot diameter to ensure a homogeneous pump irradiance in the probed area. A retro-reflector mounted on a mechanical delay stage with µm spatial accuracy is used to control the time delay $\Delta\tau$ between the two pulses. By moving the detector to the angle of the first diffracted order, a practically background-free measurement of the pump-induced effect on the grating is ensured. The total magnitude of the diffracted signal and the pump-induced change to this signal are measured simultaneously using two lock-in amplifiers and two choppers with different frequencies modulating the pump and probe beam, respectively. The sample temperature is kept at 3°C, i.e. the NCs are in the insulating phase in the absence of optical pump excitation.

The total strength of the diffracted signal D (referenced to the chopper in the probe beam) is displayed versus the time delay between the two pulses in Fig. 9.9(a). Note that this signal is directly related to the diffraction efficiency of the grating. Negative delay times correspond to a situation where the probe pulse precedes the pump pulse. The temporal evolution of the diffracted signal reveals two main signatures: (i) A large signal at negative delay times, and (ii) a marked decrease of the diffraction efficiency within $\approx 300\,\mathrm{fs}$ at zero time delay. Apparently, each singular pump event generates a transient reduction of the the refractive index contrast of the grating.

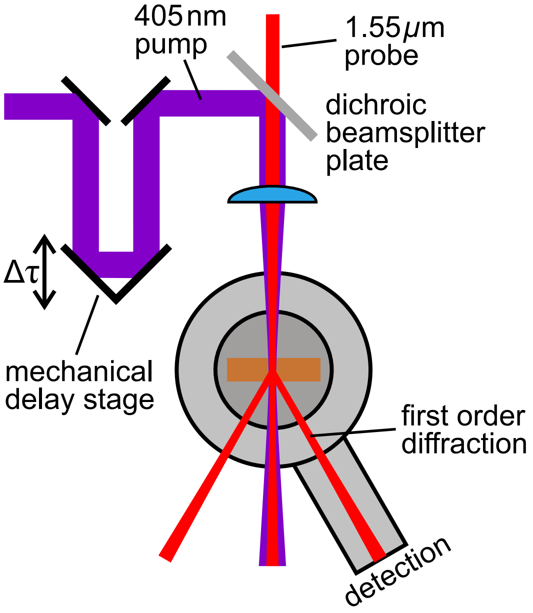

Fig. 9.8: Part of the experimental setup used for the time resolved pump-probe experiments on the ultrafast switching of the VO_2 based grating layer. The full setup is shown on page 88.

The first observation may be explained as follows: the NCs are heated by the pump pulse train and cannot relax back to thermal equilibrium within the pulse repetition period of 4 µs because of the large thermal hysteresis and insufficient lateral heat dissipation. The strong absorption and heating of the nearby gold film adds to this effect. Even though the sample temperature is kept far below T_C, the localized heat deposition by the pump pulse train switches the NCs to the persistent supercooled metallic phase. Thus, the grating is activated and a diffracted signal is present irrespective of the temporal pump-probe delay. Apparently, the long-term heat deposition in the sample is a dominating factor and leads to an undesirable overall temperature increase. This effect takes place on macroscopic time scales ($\sim$seconds) and can be understood disregarding the ultrafast dynamics of the pump-induced changes to the probe diffraction.

In order to clarify the second aspect, the pump-induced change ΔD to the diffracted signal D is evaluated with the detection referenced to the pump excitation, i.e. the usual pump-probe technique is implemented. The resulting transient showing the relative pump-induced change to the diffracted signal $\Delta D/D$ is displayed in Fig. 9.9(b). Here, only a small residual signal at negative time delays is seen. It reflects the fact that only pump-induced

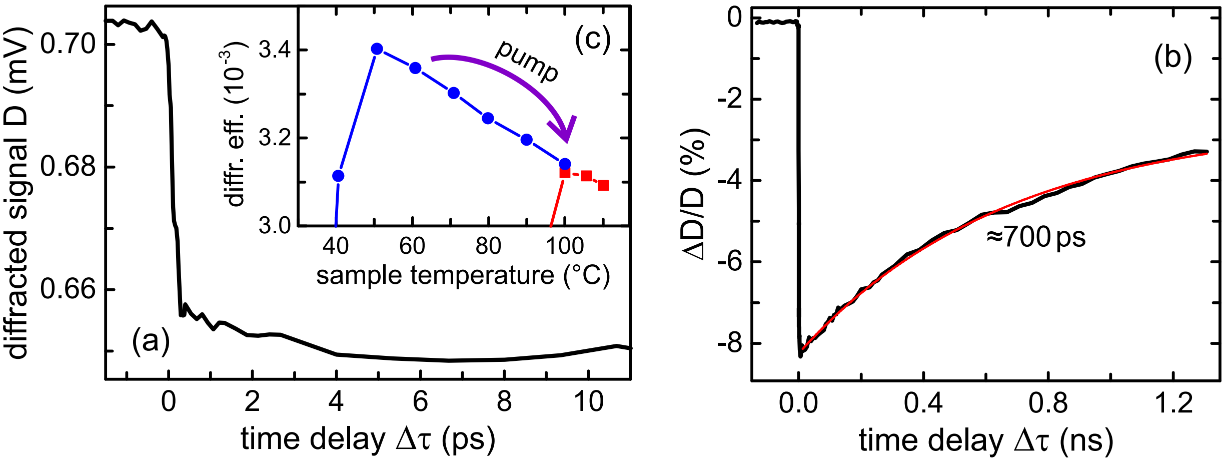

Fig. 9.9: Time dynamics of the activation of a VO_2-NC grating measured with a pump-probe scheme based on 405 nm pump and 1.55 mm probe pulses. (a) Time evolution of the diffracted signal amplitude D for varying pump-probe time delay $\Delta\tau$. (b) Long-time dynamics of the relative pump-induced change $\Delta D/D$ showing the return to the effective thermal equilibrium with an exponential time constant of $\approx$ 700ps. The red line is an exponential fit to the data for $\Delta\tau > 10$ ps. (c) Thermal hysteresis of the diffraction efficiency in the supercooled metallic phase (cf. Fig. 9.3 for the full data set). The purple arrow illustrates the influence of the a pump pulse on the diffraction efficiency of the grating.

effects occurring at the frequency of the chopper modulation (4300 Hz) are displayed.

At zero time delay, the signal is reduced by $\approx 8\,\%$ in agreement with the data in Fig. 9.9(a). Assuming the NCs are in the supercooled metallic phase, a potential explanation of the signal drop at zero time delay is the following: the pump excitation creates a situation that is equivalent to an increased sample temperature. As discussed above, the diffraction efficiency of the grating is reduced at high sample temperatures compared to lower temperatures in the supercooled metallic phase. This idea is illustrated in Fig. 9.9(c), where the temperature dependence of the diffraction efficiency is shown for the supercooled metallic phase (cf. Fig. 9.3 for the full data set). The subsequent evolution of the signal is due to the return to the effective thermal equilibrium, which is determined by the heat deposition by the pump pulse trail, with an exponential time constant of $\approx$ 700 ps.

Taken together, the pump-probe data shows a marked modification of the diffraction efficiency of the VO_2-based grating on sub-ps to ns timescales. An optically controlled full on-off modulation of the diffractive functionality is restricted to the regime of $\sim$ 10ms-100 ms in the given experimental configuration.

The obvious next step would be the extension of the optical activation of the gratings to an ultrafast modification of the light-SPP coupling. However, a transfer of the change $\Delta D/D$ to an ultrafast pump-induced SPP launching could not be demonstrated within the experimental noise level and sensitivity.

Chapter 10

Tunable Plasmonic Couplers in the Kretschmann Configuration

This chapter addresses the effects of an unstructured VO_2-NC layer in the near field of SPPs that are optically excited on a plain metal film. It is shown how the MIT-induced change of the refractive index of the VO_2-NC layer inside the mode volume of the SPP induces marked changes to the light-SPP coupling conditions. Thermo-tunable plasmonic couplers are demonstrated that introduce a novel concept of creating active plasmonic devices.

First, the method of exciting SPPs using evanescent waves in the Kretschmann configuration and the actual sample geometry used in this approach are presented (see Section 10.1). In the next step, the optical response of the specimen is analyzed experimentally for different photon energies and a thermally controlled change of the light-SPP coupling is demonstrated (see Section 10.2).

The change of the complex dielectric function of the VO_2-NCs during the MIT results in a complicated alteration of the SPP resonance conditions. Using transfer-matrix simulations, the experimental data is reproduced and a detailed picture of the MIT-induced effects on the light-SPP coupling is developed (see Section 10.3). Specifically, the roles of the change in the real and imaginary part of the VO_2-NCs is elucidated in order to understand the behavior of the thermo-tunable coupler across the energy range of the Mie-type resonance in VO_2-NCs. Potential future implementations of the approach presented here, or similar concepts, might benefit from this treatment.

Parts of the results presented in this chapter have already been published in Ref. [25].

10.1 The Kretschmann Configuration

The momentum mismatch between SPPs and light incident from the air side of the interface can be overcome using a three layer structure consisting of a thin metal film sandwiched between two dielectrics with different refractive index. SPPs are launched at the interface of the metal and the lower index medium (usually air), while the necessary enhancement of the light's wave vector happens in the additional dielectric layer with the higher refractive index. An explanation of this method is given below. In the structures examined here, the two dielectrics are air and the fused silica (SiO_2) substrate of the VO_2-NC samples.

The Kretschmann configuration is commonly employed in plasmonic ready-to-use biosensing sensors [147–149]. It enables the launching of SPPs at plain metal-dielectric interface without the need for structuring the interface, which other methods like the grating-assisted coupling usually require. Furthermore, the Kretschmann configuration played a key role in the early work on plasmons and SPPs.

Different groups found and demonstrated slightly varied implementations of this idea in the late 1960s [190; 196–198]. Kretschmann and Raether developed a way to optically excite bound SPPs on an unstructured gold-air interface, merely in order to prove that these SPP modes can re-radiate because of surface roughnesses on the gold film [190]. However, the method that excited the SPPs in the first place was later introduced more thoroughly as a way to determine the optical constants of metal films and became known as the Kretschmann configuration [197]. A very similar approach was published a little earlier by Otto [196]. In this thesis, the plasmonic couplers in the Kretschmann configuration are combined with a VO_2-NC layer.

In essence, this method relies on the transfer of light with enhanced momentum from the dielectric to the metal-air interface. This transfer is achieved utilizing the total internal reflection of light at the dielectric-metal interface, together with the subsequent tunneling of an evanescent wave though the metal layer. When the coupling conditions are met, energy is transferred from the incident light to SPP modes. Owing to this coupling scheme, the above-mentioned methods are often referred to as attenuated internal reflection . Before moving on to a detailed explanation of how the light-SPP coupling is achieved, the basic physics of the total internal reflection and evanescent waves are outlined.

Total Internal Reflection of Light & Evanescent Waves

If light hits an interface of two media with different refractive index under a non-normal angle of incidence, it will be refracted and partly transmitted as well as reflected. See the graphic on the right-hand side for an illustration of the geometry.

The amplitudes of transmitted and reflected waves can be calculated using Fresnel equations. If the transition of light is occuring from the optically thicker (i, incident) to the thinner medium (t, transmitted), i.e. from a medium with a higher refractive index $n_i > n_t$ to a medium with lower refractive index n_t, and the angle θ_i is large enough, the light will be totally reflected. In this case, all of the incident light is sent back and no energy is flowing into the lower index medium.

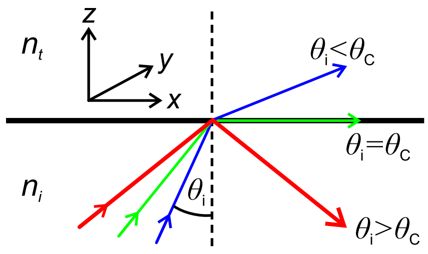

The most famous application of this effect are optical fibers, which are able to confine and guide light over hundreds of kilometers without drastical losses. Remarkably, the electromagnetic field still penetrates the lower index medium medium in form of a so-called evanescent wave. This phenomenon plays a key role in the light-SPP coupling using the attenuated internal reflection. A short description of total internal reflection and, more importantly, of the thereby generated evanescent wave will be given now. It is based on Ref. [49], pp.68ff and Ref. [199], pp.16-17).

Mathematically, the properties of the evanescent wave can be derived using Snell's law of refraction

$$\sin(\theta_t) = \frac{n_i}{n_t}\sin(\theta_i) \ . \tag{10.1}$$

Total reflection happens for $\theta_i > \theta_C$, where θ_C is the critical angle of incidence that leads to $\theta_t = \pi/2$, i.e. the refracted light is propagating parallel to the interface. In this situation ($\theta_i = \theta_C$), there is already no energy flow into the medium t. Since now $\sin(\theta_t) = 1$, Eq. (10.1) reads $1 = \frac{n_i}{n_t}\sin(\theta_i)$. For $\theta_i > \theta_C$ the right hand side of this equation becomes larger than 1. This fact will be important in the following.

In the next step, the properties of the evanescent wave will be derived. The electric field of a propagating plane wave in the x-z-plane in medium t has the form

$$E \propto \exp[i(k_{t,x}x + k_{t,z}z - \omega t)] \ . \tag{10.2}$$

The total magnitude of the propagation constant in the medium t and its two components are given by

$$k_t^2 = k_{t,x}^2 + k_{t,z}^2 \ , \quad k_{t,x} = k_t\sin(\theta_t) \ \text{ and } \ k_{t,z} = k_t\cos(\theta_t) \ , \tag{10.3}$$

with $k_t = nk_0 = n2\pi/\lambda$. The component $k_{t,x}$ is given by $k_{t,x} = k_{i,x} \equiv k_x$, which follows from Snell's law or, likewise, from the boundary conditions for the continuity of the fields components $E_{i,x} = E_{t,x}$. At this point, one can already see that the transmitted wave will have a real propagation constant in the direction parallel to the interface. By combining Snell's law and the Eqs. (10.3), the wave vector $k_{t,z}$, i.e. the propagation constant in the second medium in the direction perpendicular to the interface, can be expressed as

$$k_{t,z} = k_t\sqrt{1 - \frac{n_i^2}{n_t^2}\sin^2(\theta_i)} = i\kappa_z. \tag{10.4}$$

Since in the case of total reflection $\frac{n_i}{n_t}\sin(\theta_i) > 1$, the expression under the square root is negative and $k_{t,z}$ becomes purely imaginary. Inserting $k_{t,z} = i\kappa_z$ into Eq. (10.2) the electric field takes the form

$$E \propto \exp(\text{-}\kappa_z z)\exp[i(k_x x - \omega t)] \ , \tag{10.5}$$

which corresponds to a travelling wave in x-direction with an exponential decay of the field amplitude in z-direction. This field shows a striking similarity to the electric field of surface plasmon polaritons, cf. Eq. (8.2) on page 81. Therefore, it is not surprising that this radiation can be utilized to excite SPPs. The so-called Kretschmann configuration, which is implemented in this thesis for the purpose of demonstrating tunable plasmonic couplers, is based on this idea and will be detailed in the following.

Light-SPP Coupling in the Kretschmann Configuration

The essential idea of the above-mentioned methods is to transfer light, that is supposed to excite SPPs, from a dielectric with $n > 1$ to the gold-air interface, see Fig. 10.1(a). This transfer is achieved using the tunneling of evanescent radiation generated upon the total internal reflection at the dielectric-metal interface through a sufficiently thin metal layer. Note that total internal reflection is independent of the polarization of light, but the excitation of SPPs is only possible for TM polarization, cf. Section 8.2.

Let $k_{\mathrm{ev}} = nk_0 \sin(\theta)$ be the in-plane wave vector of the tunneled evanescent wave ($k_{\mathrm{ev}} = k_x$ in Eq. (10.5)). Similar to the principles of grating coupling, the momentum matching condition $k_{\mathrm{SPP}} = k_{\mathrm{ev}}$ is fulfilled at some angle $\theta > \theta_C$ and energy is transferred from photons to SPPs. The coupling condition in the Kretschmann configuration reads

$$k_{\mathrm{SPP}} = k_0 n \sin(\theta)\,, \tag{10.6}$$

where $k_0 = \lambda/2\pi$ is the free-space wave vector of light. When the energy transfer light→SPP is established, the reflectivity of such a structure is drastically reduced, despite

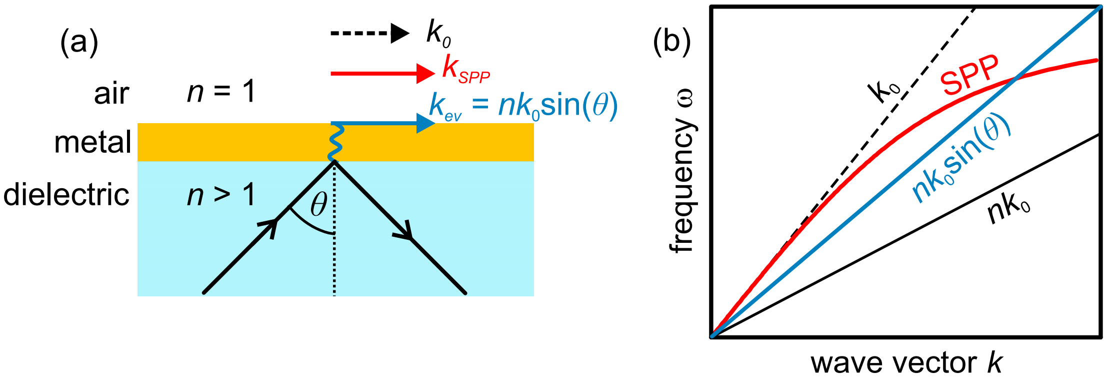

Fig. 10.1: (a) Layer structure of the Kretschmann configuration. The momentum of light is increased in a dielectric with $n > 1$. The evanescent wave generated upon total reflection tunnels through a thin metal film and excites SPPs at a metal-air interface. (b) Schematic representation using the dispersion relations of light and SPP. The momentum of photons is enhanced in the dielectric (black line) compared to free-space radiation (black dashed line). By tuning the angle θ, the momenta of the evanescent wave (blue line) and the SPP (red line) are matched for a given frequency.

the total internal reflection. Owing to this fact, the underlying principle of the Kretschmann and Otto configuration is named 'attenuated total reflection' (ATR).

Common dielectrica used in this configuration are glasses, since they are non-absorbing for most visible and near-infrared wavelengths. If a refractive index $n \approx 1.4$-1.5 is considered, the resonance angle determined by Eq. (10.6) of SPPs at an gold-air interface exited by light in the telecom regime is $\theta \sim 41°$-$45°$. Because the dielectric function of gold shows only a weak spectral dependence between 0.7 µm-2 µm, the resonance angle does not shift much in this wavelength regime. A planar dielectric layer would inhibit the angle θ from becoming large enough to excite SPPs, because of the refraction at the air-dielectric interface. To circumvent this problem, light is incident on a prism or semi-sphere in actual implementations of the Kretschmann configuration [180; 197].

The way SPP launching is made possible in the Kretschmann configuration can also be understood from the point of view of crossing the dispersions of light and SPPs. As is depicted in Fig. 10.1(b), the slope of the photon dispersion in the dielectric (black line) is smaller compared to free-space dispersion (black dashed line). By tuning the angle of incidence, any point of the SPP dispersion can be hit by the in-plane wave vector of photons in the dielectric (blue line). The momentum of these photons is transferred to the gold-air interface by the evanescent wave.

A detailed discussion of the angular shape of SPP resonance in the Kretschmann configuration as well as the influences of the material properties on the SPP will be given at the end of Section 10.3. Next, the actual Kretschmann geometry based on a VO_2-NC sample, that is applied this thesis, is introduced.

Sample Geometry

In this thesis, the influence of a VO_2-NCs layer on the light-SPP coupling generated by attenuated total reflection is investigated. For this purpose, a SPP coupler in Kretschmann configuration is combined with a layer of VO_2-NCs in the near field of the SPPs. The sample geometry used to implement this configuration is depicted in Fig. 10.2. An ≈ 35 nm thin layer of gold[1] is grown on top of a VO_2-NC sample. The dielectric that is used to increase the photon momentum is the substrate of the VO_2-NC samples, i.e. fused silica (SiO_2) with $n_{\mathrm{fs}} \approx 1.44$ for near infrared wavelengths. The critical angle for total internal reflection at the SiO_2-gold interface is $\theta_C \approx 20°$.

In order to enable the angle θ to become large enough to fulfill Eq. (10.6), a SiO_2 prism is attached to the sample substrate using an UV-curing adhesive. Note that the thickness of

---

[1] The thickness of the gold layer could not be precisely controlled during the deposition. However, its actual thickness can be estimated by comparing the output of the transfer-matrix simulations, introduced in Section 10.2, with the optical response of this structure. A few iterations were sufficient to find growth parameters that seem to correspond to a optimized film thickness of ≈ 35 nm leading to a maximized light to SPP conversion efficiency (see the discussion at the end of Section 10.3).

the fused silica substrate (500 µm) prevents any influence of the adhesive layer or the prism on the SPPs. When the coupling is established, energy is transferred from incident light to SPP modes and, thus, the optical reflectivity of the structure is reduced. The following section presents results on the influence of the VO_2 layer on the light-SPP coupling in this sample geometry.

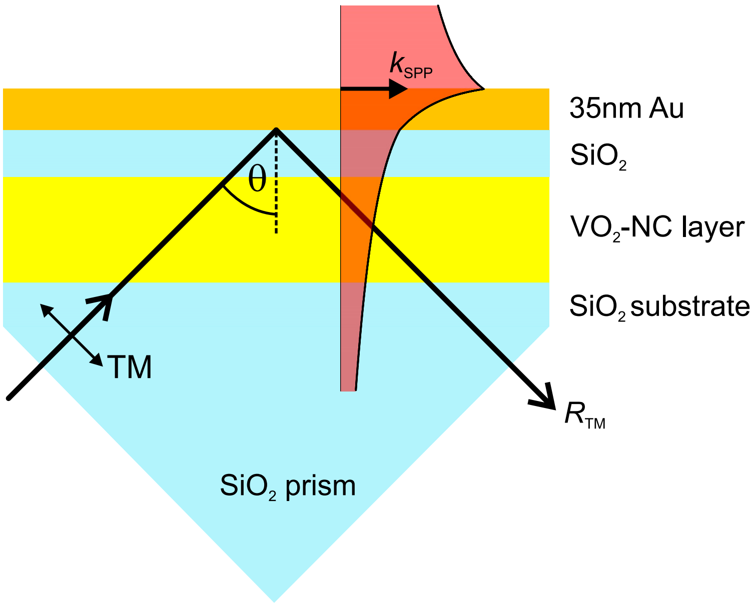

Fig. 10.2: Schematic cross-section of the sample geometry used in the Kretschmann configuration. TM polarized light (black line) is incident on a fused silica (SiO_2) prism attached to a gold covered VO_2-NC sample (not to scale). The red area illustrates the field distribution of SPPs at the gold-air interface.

10.2 Demonstration of Tunable Plasmonic Couplers

It is now studied how the light-SPP coupling at the gold-air interface is affected by the change of the dielectric function of the nearby VO_2-NC layer during the MIT. To this end, the reflected TM polarized signal R_{TM} is collected in the double-goniometer setup described above for varying angle of incidence θ. As a light source, the OPA in combination with a bandpass (12 nm FWHM) centered at a wavelength of 1.26 µm (0.98 eV photon energy) is used. At this energy, the change of the imaginary part of the NCs during the MIT is close to the maximum value, while the real part is nearly unchanged (see Fig. 6.3 on page 46).

The angular dependence $R_{\mathrm{TM}}(\theta)$ is displayed for insulating NCs (65°C sample temperature, blue line) in Fig. 10.3. Note that the data is normalized to $R_{\mathrm{TM}}(\theta = 43.0^\circ) = 1$. The rise of the signal at $\theta \approx 43.8^\circ$ is due to the onset of total internal reflection of the evanescent wave at the SiO_2-air interface. Most importantly, it is followed by a rapid decrease of the reflectivity due to the excitation of SPPs by the evanescent light. At the resonance

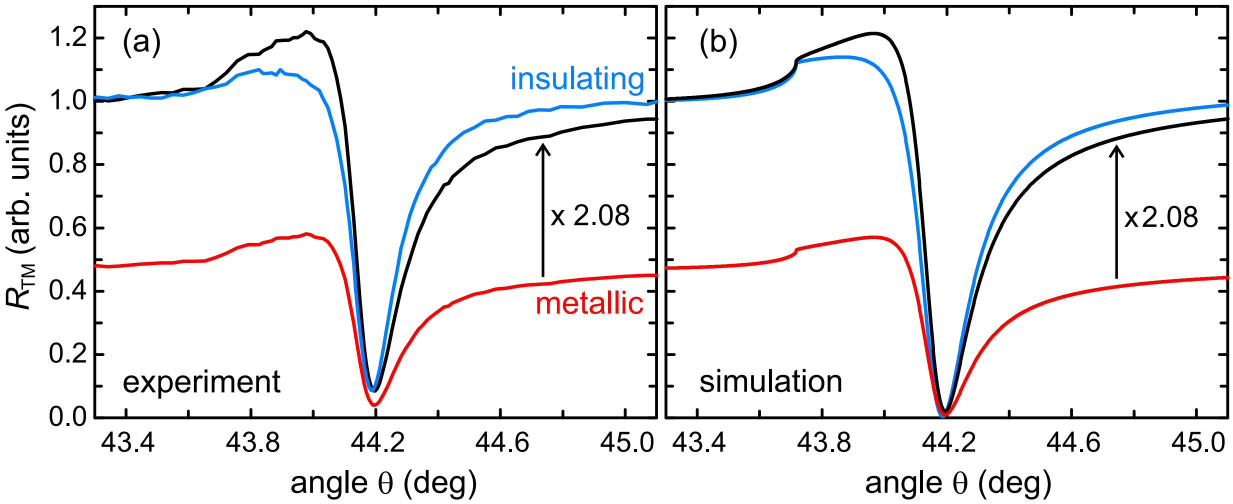

Fig. 10.3: (a) Influence of the MIT on the light-SPP coupling in the Kretschmann configuration displayed by reflectivity data $R_{TM}(\theta)$. The SPPs are launched with $\hbar\omega = 0.98\,\text{eV}$ photon energy ($\lambda = 1.26\,\mu\text{m}$). The dip at $\theta = 44.19°$ corresponds to the launching of SPPs by the incident light. (b) Transfer-matrix calculations simulating $R_{TM}(\theta)$. In both panels, data is shown for insulating (blue line) and metallic (red line) VO_2-NCs together with normalized metallic phase data (black line).

peak at $\theta = 44.19°$, almost all of the energy of the incident light is transferred to SPP modes. When the angle is increased further, it is detuned from the resonance, such that the plasmonic coupling is reduced and the signal approaches its initial value.

Moving on, the effect of the MIT-induced change of the dielectric function in the nearby VO_2 layer on the light-SPP coupling is investigated. The phase transition in the VO_2-NCs is generated by heating the sample to 105 °C, followed by cooling back to 65°C. The sample temperatures in both insulating and (supercooled) metallic phase are chosen to be equal, in order to rule out any thermal effect but the MIT on the signals.

In the metallic phase, the overall signal strength is reduced by a factor of roughly two. This reduction is caused by the double-pass through the VO_2-NC layer and agrees well with the single pass transmission decrease displayed in Fig. 6.3(c) on page 46. More importantly, the plasmonic resonance broadens and shifts to a slightly larger angle. The altered shape of the resonance becomes more evident when the signal is corrected for the overall transmission decrease by normalizing it to $R_{TM}(\theta = 43.0°) = 1$ (black line). The strength of this thermo-tunable change of the light-SPP coupling is studied in detail below.

The broadening and shift may be explained by the increased damping related to the absorption of the photonic part of the SPP in the metallic VO_2-NCs. It is discussed below, how additional damping processes change the frequency and momentum of the SPP and result in altered light-SPP coupling conditions.

Modeling the Optical Response Using the Transfer-Matrix Method

To further corroborate the influence of the MIT-induced change of the refractive index of the VO_2-NCs on the SPP resonance, the optical response of the Kretschmann geometry is simulated using the transfer-matrix method (see Ref. [49], pp.102-115)[2]. The simulations provide a crucial tool to understand the MIT-induced change to the light-SPP coupling, which is discussed in detail in Section 10.3.

Based on Fresnel equations, which are derived from Maxwell's equations, this method is able to compute the amplitudes and phases of electric and magnetic fields inside layered isotropic media. As pointed out in Section 8.2, Maxwell's equations show the existence of bound travelling plasmons (SPPs), if the materials at the interface have the required refractive index. Therefore, the transfer-matrix method intrinsically includes plasmonic effects, even though the only incorporated material properties are the bulk complex refractive index $\tilde{n} = n + ik$. More specifically, the simulations are used to compute the reflectivity of TM polarized light in the Kretschmann sample configuration for varying angles of incidence. They reproduce the experimental data since the calculated quantity is equal to the experimentally measured parameter $R_{\mathrm{TM}}(\theta)$. The sample is modeled by a sequence of five homogeneous, planar layers, with air and fused silica as the semi-infinite top and bottom layer, respectively. A 35 nm gold film and a 42.5 nm SiO_2 layer are used. The data for the refractive index of air [182], SiO_2 [191] and gold [183] is taken from literature.

The VO_2-NCs are taken into account as a homogeneous layer with a thickness of 90 nm. As mentioned earlier, the VO_2-NC samples used throughout this thesis were processed using sightly different parameters and, consequently, the distribution of NC diameters and their dielectric properties are not exactly equal for all specimen. In particular, the Kretschmann experiments presented here are performed on a different sample as the spectral ellipsometry. For the simulations, the real part of the refractive index for both VO_2 phases is taken from the actual ellipsometry data, cf. Fig. 6.3. The same is true for the imaginary part k in the insulating phase. However, the imaginary part of the metallic phase is adjusted such that the transmission decrease far away from the plasmonic resonance is reproduced by the simulations. This procedure eliminates the uncertainty in the dielectric function to some extent and results in a better overall agreement of simulations and experimental data. Apart from the just-mentioned adjustment, only literature values for the dielectric functions are used. Note that they are not used as a fitting parameter to optimize the congruence of simulations and experimental data near the SPP resonance.

In a first step, transfer-matrix simulations are performed to model the Kretschmann resonance presented above for 0.98 eV photon energy. The results of this simulation are depicted in Fig. 10.3(b). Again, the blue and red lines correspond to insulating and metallic

---

[2] The simulations are performed using Mathematica. The original code was created by Dr. Claudia Ruppert and modified by the author to fit the Kretschmann geometry.

VO_2-NCs, respectively, and the black line shows normalized metallic phase data. It is evident that the optical response seen in the experiment is met well by the simulations. In particular, the positions of the resonance coincide and, furthermore, the broadening and the shift of the resonance in the metallic phase is reproduced. The missing sharpness of the angular features and the slightly larger value of the minimum reflectivity in the experimental data can be attributed to the finite angular and spectral resolution of the setup.

To sum up, the agreement of the data sets and the simulations is satisfying in multiple ways. (i) The simulations succeed in modelling the optical response of the five-layer Kretschmann geometry including the launching of SPPs. (ii) The VO_2-NCs can be treated as a homogeneous effective medium. (iii) The MIT-induced effect on the SPP resonance shape is successfully reproduced by changing the refractive index of the VO_2-NC layer.

Tunability & Spectral Dependence of the Light-SPP Coupling

In order to attain a more detailed analysis of the MIT-induced changes to the SPP resonance, the Kretschmann-type experiments are repeated for different photon energies in the telecom wavelength regime. In particular, the special nature of the VO_2 nanocomposite opens up the opportunity to study the respective effects of a change in the real or imaginary part of the refractive index $\tilde{n} = n + ik$. The aim of this examination is to understand and potentially predict the behavior of the tunable plasmonic coupler across the entire energy range of the absorptive resonance in the VO_2-NCs.

The change of $\tilde{n}$ during the MIT in the VO_2-NC layer is dominated by the Mie-type resonance in the metallic NCs, as is shown in Fig. 6.3 on page 46. The imaginary part k increases for all photon energies in the telecom wavelength regime, which allows for a selection of different magnitudes of change by varying the photon energy. As opposed to this, the resonance gives the opportunity to select photon energies where the real part increases (0.80 eV), remains unchanged (0.98 eV) or decreases (1.37 eV).

Table 10.1 provides an overview of the values of $\tilde{n}$ used in the simulation, where n is taken from the ellipsometry data presented in Fig. 6.3 and k is adjusted to match the transmission decrease away from the plasmonic resonance. In addition to the light sources mentioned above (Er:fiber laser and OPA), the TiSa laser in combination with a bandpass (10 nm FWHM) at 0.905 µm (1.37 eV) is used. The three above-mentioned photon energies are covered by these lasers.

The experimentally measured angular SPP resonances for the three photon energies and both insulating and metallic VO_2-NCs are shown in Fig. 10.4(a)-(c). Again, the MIT-induced overall drop in transmission is related to the decreased transmission through the metallic VO_2-NCs. For all photon energies, the resonance is broadened and shifted to larger angles in the metallic phase compared with the insulating phase. The different signs of the change in the real part have no obvious counterpart in the signals. Apparently, a quantitative

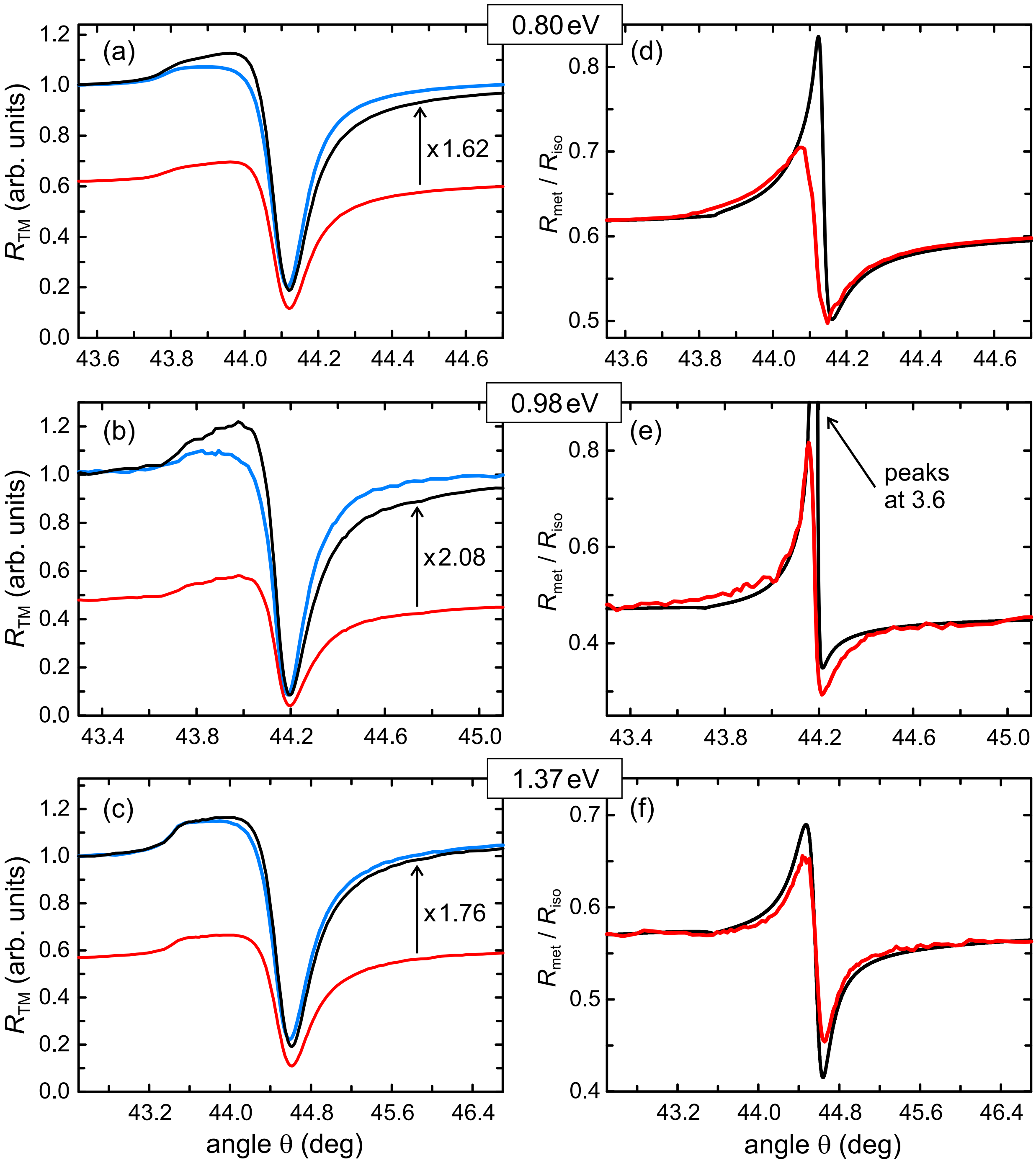

Fig. 10.4: (a)-(c) Reflectivity data $R_{TM}(\theta)$ taken with different photon energies given in the figure for insulating (blue) and metallic (red) VO_2-NCs. The black line shows normalized metallic phase data. (d)-(f) Relative change of the reflectivity caused by the MIT for different photon energies. Red lines: experimental data, black lines: results of transfer-matrix simulations.

Table 10.1: Values of the complex refractive index of the VO_2 nanocrystal layer $\tilde{n} = n + ik$ for insulating (ins) and metallic (met) VO_2-NCs. Note that the sign of the change in n is opposite for 0.80 eV and 1.37 eV photon energy.

	n		k	
$\hbar\omega$ (eV)	ins	met	ins	met
0.80	1.75	1.91	0.063	0.368
0.98	1.75	1.73	0.077	0.457
1.37	1.74	1.61	0.091	0.260

analysis of the MIT-induced change to the light-SPP coupling is hard to achieve from the raw reflectivity data. This issue is clarified in the following section.

In the next step, the tunability of the light-SPP coupling is quantified. For this purpose, the relative MIT-induced change of the reflectance is shown (red lines) in the right-hand panels (d)-(f) of Fig. 10.4. This quantity is defined as the ratio $R_{\mathrm{met}}/R_{\mathrm{iso}}$. While the overall offset is due to the transmission decrease, the changes to the SPP resonance lead to marked modifications of the reflectance near the resonance angle. It can be seen that the effect of the MIT on the optical response is strongly sensitive to the angle of incidence. For example, at 0.98 eV photon energy, the change in reflectance is tunable from 30% to 80% within an angular range of only 0.05°. If the tunable coupler is used in a configuration where the angle of incidence is fixed, the MIT gives rise to a substantial change of the light-SPP coupling efficiency.

The experimental data is now compared to the simulations in order to explore the capabilities of the investigated structure. The black lines in Fig. 10.4 show the results of the simulations using the procedure for determining the refractive index of the metallic phase given above. For all photon energies, the positions of the resonances in simulation and experiment coincide and the shape of the change near the resonance matches the experimental data. It is evident that the MIT-induced changes seen in the experiment do not reach the maximum values that can potentially be obtained in the investigated sample geometry. Remarkably, the simulations peak at $R_{\mathrm{met}}/R_{\mathrm{iso}} \approx 3.6$ for $\hbar\omega = 0.98\,\mathrm{eV}$ (not shown). Improvements in the experimentally achieved tunability could be made using higher spectral and angular resolution.

To sum up, marked MIT-induced modifications of the light-SPP coupling are found for different photon energies spanning the telecom wavelength regime. From the experimental data and simulations presented here, the physical background of the respective influence of n and k on the SPP launching is not elucidated. The data suggest that the angular shape of the alteration to the light-SPP coupling depends on the detuning from the central energy of the Mie-type resonance in the VO_2-NCs.

10.3 Influence of the MIT-Induced Change of the Complex Refractive Index

In this section, the respective effect of a change in the real or imaginary part of the refractive index $\tilde{n} = n + ik$ of the VO_2-NCs on the light-SPP coupling is investigated. The change of n has a different sign on either side of the Mie-type resonance in the metallic NCs, and the experiments presented above could not elucidate the effects of real and imaginary part. In order to design potential applications, it is important to have a sound knowledge of the interactions in the five-layer sequence of the tunable plasmonic coupler. This section presents a detailed analysis of this issue based on elaborate transfer-matrix simulations. Furthermore, established textbook knowledge of the physics of the Kretschmann configuration is incorporated into the discussion of the results.

When comparing the signals (experimental data or simulations) with respect to the influence of the change in the real part, no obvious trend is seen (cf. Fig. 10.4). This finding points towards a rather complicated interplay that is not easily resolved in the data presented so far. Fortunately, the transfer-matrix calculations offer the opportunity to selectively switch only either the real part n or the imaginary part k to the respective value of the metallic phase. Exemplary results of this procedure are depicted in Fig. 10.5 for 1.37 eV photon energy. The labels next to the curves state the parts of the refractive index that are switched to the metallic phase, i.e.:

none (blue): insulating $VO_2 \rightarrow \tilde{n} = n_{\text{iso}} + ik_{\text{iso}}$
both (red): metallic $VO_2 \rightarrow \tilde{n} = n_{\text{met}} + ik_{\text{met}}$
real (green): only real part of metallic $VO_2 \rightarrow \tilde{n} = n_{\text{met}} + ik_{\text{iso}}$
imaginary (black): only imaginary part of metallic $VO_2 \rightarrow \tilde{n} = n_{\text{iso}} + ik_{\text{met}}$

The two main observations to be made here are that the shift of the resonance position seems to be caused solely by the change in the imaginary part Δk, while Δn leads to an altered overall reflectivity and a deeper resonance.

Before moving on to an explanation of these findings, a more instructive representation of the effects of n and k for the three different photon energies is given. In Fig. 10.6, the relative change to the reflectivity in the insulating phase is shown for a selective switching of real and/or imaginary part, i.e. for the three configurations (both, real, imaginary) defined above. Note that the full simulations (both) are also included in Fig. 10.4(d)-(f). For all photon energies, the observation made above applies: the shift is caused by the increased imaginary part. It is interesting that the altered real part leads to stronger resonances at both 0.80 eV and 1.37 eV photon energy, even though the sign of Δn is different. At 0.98 eV, the small negative Δn results in a minor decrease of the resonance strength. In the following, an explanation of this behavior will be given. At this point, it can already be stated that a full description of the MIT-induced changes to the SPP resonance shape needs to include the change of both the real part and imaginary part of the refractive index.

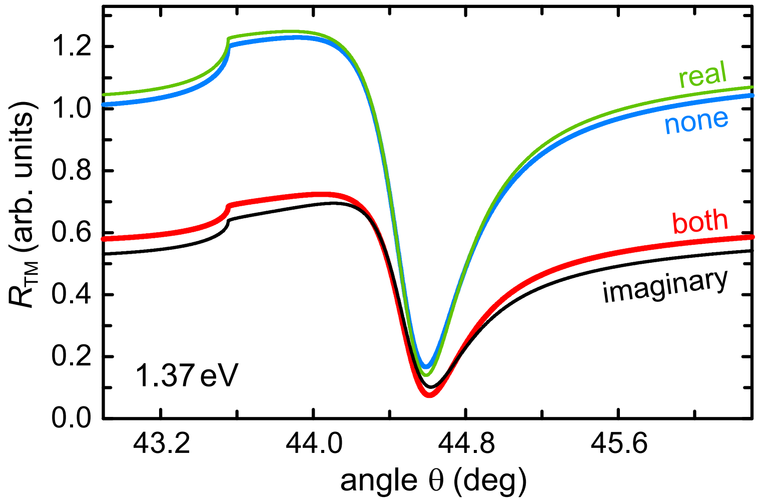

Fig. 10.5: Results of transfer-matrix simulations of the reflectivity R_{TM} in the Kretschmann configuration for 1.37 eV photon energy when only the real (green line) or imaginary (black line) part of the VO_2 refractive index is changed to the metallic phase. Blue and red lines show the simulation for full insulating and metallic VO_2, respectively. All data points are normalized to $R_{TM}(\theta = 42°)$ in the insulating phase (blue).

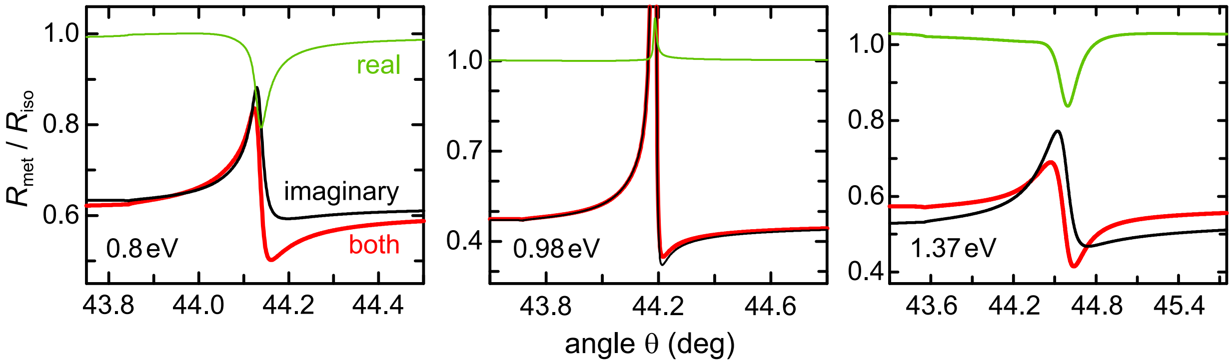

Fig. 10.6: Results of the transfer-matrix simulations for a change of only either the imaginary or the real part of the VO_2 refractive index $\tilde{n} = n + ik$. The labels at the lines in the left-hand panel state the part(s) of the refractive index with value(s) of the metallic phase .

Scattering and Damping Processes in the Kretschmann Configuration

Finally, the influence of the real and imaginary part of the VO_2 refractive index is elucidated with respect to the physics in the five-layer Kretschmann geometry. The following discussion will distinguish between effects of Δk or Δn on the propagation of the incident/reflected light and on the properties of the SPP. It might be helpful for the reader to keep in mind that the physics of a SPP, which is a plasma oscillation coupled to an electromagnetic field, show similarities to a driven, damped harmonic oscillator.

The most obvious effect of a change in the imaginary part is the strongly decreased reflectivity induced by the increased absorption of light in the VO_2 layer. This effect is not connected to the light-SPP coupling and does not require further discussion.

Mathematically, the plasmonic resonance in the standard three layer Kretschmann geometry can be approximated by a Lorentzian function[3] [180]

$$R(k_x(\theta)) = 1 - \frac{4\Gamma_i \Gamma_{\mathrm{rad}}}{[k_x(\theta) - (k^0_{\mathrm{SPP}} + \Delta k_{\mathrm{SPP}})]^2 + (\Gamma_i + \Gamma_{\mathrm{rad}})^2} \tag{10.7}$$

where $k_x(\theta)$ is the in-plane wave vector of light (evanescent wave) and k^0_{SPP} is the SPP wave vector calculated for two semi-infinite media given by Eq. (8.8). The quantities Γ_i and Γ_{rad} describe the internal and radiative damping, respectively. The term Δk_{SPP} is a complex quantity connected to the refractive index of the materials in the SPP mode volume, which effectively corrects the SPP wave vector to a new value $(k^0_{\mathrm{SPP}} + \Delta k_{\mathrm{SPP}})$. The real part of Δk_{SPP} causes a shift of the position of minimum reflectivity and the imaginary part introduces an additional damping term that broadens the resonance (as all imaginary quantities in the Lorentzian function do).

To get a more microscopic view of the physical processes that are summarized in the complex refractive index, the next paragraph discusses the damping mechanisms in the VO_2-based nanocomposite. If the VO_2-NCs are switched to the metallic phase, these mechanism change the light-SPP coupling. First, scattering processes associated with the imaginary part k are discussed, followed by a possible explanation of the influence of the real part n.

Elastic and inelastic scattering processes of the photonic or electronic part of the SPP change its energy or momentum, which, in turn, leads to altered light-SPP coupling condition [180; 181; 200; 201]. The absorption of photons in a metal due to the interaction with conducting electrons (Ohmic losses) leads to a loss of energy of the SPP. Likewise, the collective electron motion may be damped by electron-phonon scattering. These processes results in a decreased oscillation frequency ω of the electron ensemble, which means that the dispersion line of the SPP is shifted to lower frequencies, cf. 10.1(b). In other words, the SPPs get 'heavier'. Consequently, a higher photon momentum is needed to drive the oscillation at a given frequency determined by the exciting photon. Since the photon momentum is adjusted by the angle of incidence θ in the Kretschmann configuration, the resonance seen in the data for $R_{\mathrm{TM}}(\theta)$ is shifted to larger angles. The dominant effect of elastic scattering processes is a redistribution of the momentum of the SPP. Different photon momenta are now needed to drive the SPP, resulting in a broadening of the resonance.

---

[3] This approximation is valid when $\mathrm{Re}[\epsilon_{\mathrm{Au}}] < 1$ and $\mathrm{Im}[\epsilon_{\mathrm{Au}}] \ll \mathrm{Re}[\epsilon_{\mathrm{Au}}]$. These assumptions are true for all photon energies considered here, see Fig. 8.2.

An additional damping mechanism Γ_{rad} is instrinsically present in the Kretschmann configuration, which is the emission of leakage radiation into the dielectric [180; 181]. This effect might explain the alteration of the minimum reflectivity upon changing the real part n of the VO_2-NC's refractive index. In Fig. 10.1(b), the propagation constant of the SPP mode is on the left side of the light's dispersion in the dielectric. Accordingly, the energy of the SPPs is sufficient so that they can re-radiate into the dielectric. In there, this leakage radiation interferes with the totally reflected light (which experiences a phase-change of π upon reflection). It is this interference that determines the minimum reflectivity R_{min}. Since the amplitude of the leakage radiation depends on the thickness of the metal film, R_{min} also does. It can be shown that the metal film can be designed to have an optimal thickness which leads to a perfect destructive interference, i.e. $R_{\mathrm{min}} = 0$ [180]. In this case, all of the incident energy is deposited in metal film.

Returning to the MIT-induced changes to the reflectivity in the five player geometry of the samples examined here, the change of the resonance strength caused by Δn can be understood when looking at the interference that determines R_{min}. When the real part of the VO_2-NCs refractive index changes, light passing through the VO_2 layer experiences a phase change. Thereby, the interference is modified and the minimum reflectivity changes.

In order to test this assumption, the phase shift $\Delta\phi(n)$ in the VO_2 layer is computed based on the geometry and a refractive index of the layer in the range $1.5 < n < 2$. Next, R_{min} is extracted from transfer-matrix simulations for k_{iso}, $1.5 < n < 2$ and 0.8 eV and 1.37 eV photon energy. Taken together, these steps yield the dependence $R_{\mathrm{min}}(n)$, which reveals the potential influence of a phase shift in the VO_2 layer on the depth SPP resonance. The results of this procedure (data not shown) show a similar reduction of R_{min} as seen in the experimental data. For both photon energies, the interference is altered in a way that leads to a more stronger destructive interference of incoming with re-emitted light.

To sum up, this section has shown that the real and imaginary part of the VO_2-NC's refractive index change the light-SPP coupling conditions in distinct ways. Scattering processes in the metallic NCs predominantly shift and broaden the resonance, as is expected from the physics of driven, damped oscillations. The MIT-induced change in the real part presumably has a less obvious effect on the SPP resonance. The phase shift in the VO_2-NC layer, and the related alteration of the interference that determines the minimum reflectivity, seem to be the cause for the deeper resonance in the metallic phase.

Chapter 11

Conclusions and Outlook Part II

Vanadium dioxide (VO_2) is a smart optical material featuring a potentially ultrafast metal-insulator phase transition (MIT) close to room temperature. In ion-beam-implanted VO_2-NCs, the MIT is accompanied by a marked change of the dielectric function, which can be tailored to be strongest in the telecom wavelength regime. Based on cooperative research, this change is spectrally resolved and assigned to a resonance in the metallic spherical NCs, see Section 6.2. Differently processed (future) samples may be analyzed the same way and compared systematically.

Since the active layer of VO_2-NC samples is only ≈ 90 nm thick, they are favorable for the integration into nanoscale photonic devices and 'flat optics'. Furthermore, the implantation of VO_2-NCs is compatible with the technology relevant materials SiO_2 and Si.

The uniquely broad thermal hysteresis of the MIT in VO_2-NCs is studied, classified and compared to literature in Section 6.3. A combining analysis of the microscopic, structural details of the VO_2-NC specimen and the physics of the MIT allows to attribute the large bistability to the good crystallinity of the single domain NCs as well as to the embedment in the fused silica matrix. Potential devices related to memory and storage applications could benefit from this large hysteresis. Furthermore, it is a requirement for the creation of photonic and plasmonic element presented in this thesis.

The post-fabrication irradiation of VO_2-NCs with argon ions enables the engineering of the critical temperatures and the thermal hysteresis. A series of samples is studied in order to elucidate the effect of different doses of argon in Section 6.4. Essentially, the argon ions introduce defects into the lattice of the NCs that change the critical temperature or, ultimately, completely inhibit the MIT. This deactivation is made use of in this thesis for the creation of switchable diffraction gratings and plasmonic grating couplers. However, for the purpose of tuning the critical temperature of the MIT in VO_2-NCs, without inducing a deactivation at the same time, other dopants seem to be more suitable.

Using low-cost diode lasers, the MIT in VO_2-NCs can be readily induced on a ms time scale. It is shown that the optically induced MIT can be combined with the broad thermal hysteresis to enable the preparation of a long-term stable supercooled metallic state, cf. Section 7.1. Because of the surrounding fused silica, the MIT in VO_2-NCs does not result in any degradation such that the structures may be used for highly repetitive operation. The long-term stability of the supercooled metallic phase and durability of the structures is explicitly verified.

The spatial dielectric contrast between areas of insulating and metallic VO_2-NCs allows for the fabrication of switchable diffractive elements using the site-selective deactivation of the MIT [87]. A spatially selective, optically induced MIT on the µm scale offers the possibility to realize reconfigurable photonic elements formed from spatial micro-patterns of insulating and supercooled VO_2-NCs. The definition of arbitrary two-dimensional pattern happens optically with µm spatial resolution. Different approaches of imprinting fundamental photonic elements such as diffraction gratings and zone plates are successfully demonstrated in Section 7.3. Any imprinted structure is easily erased in a non-destructive fashion by cooling to below room temperature.

The present study focuses on thin planar optical elements that are favorable for the integration into layered nanoscale specimen. However, more complex structures may be realized in samples containing several layers of NCs.

The hysteresis underlying the presented concept can be tailored to suit possible applications. While the definition of smaller NCs would further enlarge the hysteresis, doping the NCs or choosing different substrates allows to bring the critical temperatures of the MIT closer to room temperature.

Son et al. use a homogeneous thin film of VO_2 to demonstrate a reconfigurable photonic element for focusing optical beams in the telecom wavelength regime [134]. They utilize a phase front curvature that is generated by a laser-induced temperature gradient and the approximately linear relationship of refractive index change and temperature in their VO_2 system.

The concepts underlying the demonstration of photonic elements presented here has been taken up by other groups. Rensberg et al employ selective ion beam engineering of VO_2 layers for the generation of active optical metasurfaces [130]. Furthermore, the approach to optically define reconfigurable patterns is extended by Zhang et al. [202]. In their work, UV light is used to imprint local supercooled metallic areas into a thin VO_2 layer in order to create laterally confined conductive patterns. This work utilizes the different conductivity of insulating and metallic VO_2 and demonstrates the versatility of the approaches introduced in Chapter 7 and Ref. [21].

Currently ongoing research utilizes the change of the VO_2 refractive index in a Fabry-Perot resonator geometry. The light-induced MIT leads to a marked modification of the transmission spectrum through this structure. Preliminary results gained in a early stage of the project point towards a MIT-induced spectral shift of singular modes of up to 1 nm, which is ≈ 10 % of the mode spacing.

Different methods of utilizing the MIT-induced change of the dielectric function in VO_2-NCs for the demonstration of plasmonic modulators are demonstrated in this thesis.

The method of grating-assisted light-SPP coupling is introduced in Section 9.1. It utilizes the change of the momentum of light in a periodically structured layer to overcome the momentum mismatch between photons and SPP. Switchable diffraction gratings based on VO_2 nanocomposites are created using the deactivation of the phase transition in selected ensembles of VO_2 nanocrystals. The resulting thermochromic grating layers show a substantial switching contrast of a factor 45 in the diffraction efficiency, cf. Section 9.2. When placing this layer in the near field of SPPs at an otherwise unstructured gold-air interface, deterministic control over the light-SPP coupling is made possible using the thermally or optically induced MIT, cf. Section 9.3.

In all investigated samples, the substantial dielectric switching contrast of the gratings ensures a practically complete on-off modulation of the SPP resonance. The successful demonstration of the VO_2-based grating couplers opens up new routes for the creation of active plasmonic elements.

The variety of ways to induce the MIT in VO_2 offers many possibilities to control the launching of SPPs in the proposed structures. Thermal and optical activation is demonstrated in this thesis. Because of the close vicinity of the VO_2-NC layer to the gold film, Ohmic heating by a current flow through the gold film could be utilized to control the grating coupler electronically.

A full modulation of the light-SPP coupling on ultrafast timescales using fs laser pulses is not feasible in the given experimental configuration, as shown in Section 9.4. An interplay of the heat capacity of the sample, the pulse repetition rate and the thermal hysteresis of the VO_2-NCs prevents a such a modulation. However, even at elevated effective temperatures, a pump-induced sub-ps modulation of the diffraction efficiency of ≈ 8 % is found, demonstrating the potential of fast, switchable grating couplers based on VO_2-NCs. VO_2 systems with a narrower hysteresis can be expected to yield a better performance with regard to fast switching. Thin films of VO_2, which generally show a narrower hysteresis, have the drawback of a lower MIT-induced dielectric contrast in the telecom wavelength regime. On the other hand, doping VO_2-NCs after the fabrication provides the tools to maintain the benefits of the NCs, while at the same time reducing the width of the hysteresis (see Section 6.3)

In the Kretschmann configuration, which is introduced in Section 10.1, the excitation of SPPs is made possible by increasing the momentum of photons in an additional dielectric layer. This momentum is transferred to a gold-air interface by the evanescent wave generated upon total internal reflection.

A layer of VO_2-NCs is placed in the near-field vicinity of the interface supporting the SPPs, cf. Section 10.2. The MIT-induced change of the VO_2 refractive index changes the effective dielectric function associated with the optical generation of SPPs and, thereby, leads to a marked modification of light-SPP coupling. Specifically, the transition to the metallic phase shifts and broadens the angular resonance. Taken together, thermo-tunable plasmonic couplers are demonstrated. They facilitate a substantial modulation of the light-SPP coupling efficiency and offer a strong sensitivity to the angle of incidence near the resonance angle.

VO_2 offers many potential means to control its phase. Instead of triggering the MIT thermally, optical or electronic means could be used as a control input of the modulation. For example, an additional pump laser or a current flow through the gold layer are possible ways to control the light-SPP interaction with external means.

The sub-wavelength dimensions of the metal-dielectric-VO_2 nanocomposite, together with the various interactions of the photonic and plasmonic part of the SPP mode with light and matter, result in a complicated answer of the system to the change of the VO_2-NC's refractive index during the MIT. Both real and imaginary part have to be considered in order to understand the MIT-induced effect, as discussed in Section 10.3. Important features of the change in the SPP resonance shape are reproduced in transfer-matrix simulations of the optical response of the actual sample geometry. Furthermore, a large part of the features is explained based on the physics of the three layer Kretschmann configuration. The design and interpretation of future experiments or potential applications will benefit from this treatment.

Bibliography

[1] International Year of Light 2015, *About the Year of Light*, last accessed 18 August 2016, URL: `http://www.light2015.org/Home/About.html`

[2] National Research Council, *Harnessing Light: Optical Science and Engineering for the 21st Century* (The National Academies Press Washington, DC, 1998)

[3] R. Menzel, *Photonics - Linear and Nonlinear Interactions of Laser Light and Matter*, 1st ed. (Springer, Berlin, 2001)

[4] The Royal Swedish Academy of Sciences, *Scientific Background on the Nobel Prize in Chemistry 2014*, retrieved 18 August 2016, URL: `https://www.nobelprize.org/nobel_prizes/chemistry/laureates/2014/advanced-chemistryprize2014.pdf`

[5] Class for Physics of the Royal Swedish Academy of Sciences, *Scientific Background on the Nobel Prize in Physics 2014*, retrieved 18 August 2016, URL: `https://www.nobelprize.org/nobel_prizes/physics/laureates/2014/advanced-physicsprize2014.pdf`

[6] Bundesministerium für Bildung und Forschung (BMBF), *Photonik Branchenreport: Aktuelle Lage 2015*, German, retrieved 25 July 2016, URL: `https://www.bmbf.de/files/Aktueller_Lagebericht_Photonik_2015.pdf`

[7] G. E. Moore, "Cramming More Components Onto Integrated Circuits," *Proceedings of the IEEE* **86**, 82–85 (1998)

[8] P. S. Peercy, "The drive to miniaturization," *Nature* **406**, 1023–1026 (2000)

[9] The Economist, *After Moore's law | Technology Quarterly*, last accessed 18 August 2016, URL: `http://www.economist.com/technology-quarterly/2016-03-12/after-moores-law`

[10] M. Bohr, *Opening New Horizons: 14 nm Process Technology*, © Intel Corporation, retrieved 19 August 2016, URL: `http://www.intel.com/content/dam/www/public/us/en/documents/technology-briefs/bohr-14nm-idf-2014-brief.pdf`

[11] H. J. Caulfield and S. Dolev, "Why future supercomputing requires optics," *Nature Photonics* **4**, 261–263 (2010)

[12] G. Chen, H. Chen, M. Haurylau, N. A. Nelson, D. H. Albonesi, P. M. Fauchet and E. G. Friedman, "Predictions of CMOS compatible on-chip optical interconnect," *Integration, the VLSI Journal* **40**, 434 –446 (2007)

[13] A. Ghiasi, "Large data centers interconnect bottlenecks," *Optics Express* **23**, 2085–2090 (2015)

[14] G.P. Argawal, *Fiber-Optic Communication Systems*, 4th ed. (John Wiley & Sons, Inc, Hoboken, New Jersey, 2010)

[15] D. J. Richardson, J. M. Fini and L. E. Nelson, "Space-division multiplexing in optical fibres," *Nature Photonics* **7**, 354–362 (2013)

[16] J. H. Davies, *The Physics of Low-Dimensional Semiconductors: An Introduction*, 1st ed. (Cambridge University Press, 1998)

[17] T. Jostmeier, T. Wecker, D. Reuter, D. J. As and M. Betz, "Ultrafast carrier dynamics and resonant inter-miniband nonlinearity of a cubic GaN/AlN superlattice," *Applied Physics Letters* **107**, (2015)

[18] F. J. Morin, "Oxides Which Show a Metal-to-Insulator Transition at the Neel Temperature," *Physical Review Letters* **3**, 34–36 (1959)

[19] H. W. Verleur, A. S. Barker Jr and C. N. Berglund, "Optical Properties of VO_2 between 0.25 and 5 eV," *Physical Review* **172**, 788–798 (1968)

[20] Z. Yang and S. Ramanathan, "Breakthroughs in Photonics 2014: Phase Change Materials for Photonics," *IEEE Photonics Journal* **7**, 1–5 (2015)

[21] T. Jostmeier, J. Zimmer, H. Karl, H. J. Krenner and M. Betz, "Optically imprinted reconfigurable photonic elements in a VO_2 nanocomposite," *Applied Physics Letters* **105**, 071107 (2014)

[22] Editorial, "Surface plasmon resurrection," *Nature Photonics* **6**, (2012)

[23] Interview with Joachim Krenn by David Pile, "Perspective on plasmonics," *Nature Photonics* **6**, 714–715 (2012)

[24] D. K. Gramotnev and S. I. Bozhevolnyi, "Plasmonics beyond the diffraction limit," *Nature Photonics* **4**, 83–91 (2010)

[25] T. Jostmeier, M. Mangold, J. Zimmer, H. Karl, H. J. Krenner, C. Ruppert and M. Betz, "Thermochromic modulation of surface plasmon polaritons in vanadium dioxide nanocomposites," *Optics Express* **24**, 17321–17331 (2016)

[26] T. Ando, A. B. Fowler and F. Stern, "Electronic properties of two-dimensional systems," *Review of Modern Physics* **54**, 437–672 (1982)

[27] H. Machhadani, P. Kandaswamy, S. Sakr, A. Vardi, A. Wirtmüller, L. Nevou, F. Guillot, G. Pozzovivo, M. Tchernycheva, A. Lupu, L. Vivien, P. Crozat, E. Warde, C. Bougerol, S. Schacham, G. Strasser, G. Bahir, E. Monroy and F. H. Julien, "GaN/AlGaN intersubband optoelectronic devices," *New Journal of Physics* **11**, 125023 (2009)

[28] L. Monteagudo-Lerma, F. B. Naranjo, S. Valdueza-Felip, M. Jiménez-Rodríguez, E. Monroy, P. A. Postigo, P. Corredera and M. González-Herráez, "III-nitride-based waveguides for ultrafast all-optical signal processing at 1.55 µm," *physica status solidi (a)* **213**, 1269–1275 (2016)

[29] J. Faist, F. Capasso, D. L. Sivco, C. Sirtori, A. L. Hutchinson and A. Y. Cho, "Quantum Cascade Laser," *Science* **264**, 553–556 (1994)

[30] M. Beck, D. Hofstetter, T. Aellen, J. Faist, U. Oesterle, M. Ilegems, E. Gini and H. Melchior, "Continuous Wave Operation of a Mid-Infrared Semiconductor Laser at Room Temperature," *Science* **295**, 301–305 (2002)

[31] D. Hofstetter, S.-S. Schad, H. Wu, W. J. Schaff and L. F. Eastman, "GaN/AlN-based quantum-well infrared photodetector for 1.55 µm," *Applied Physics Letters* **83**, 572–574 (2003)

[32] F. H. Julien, M. Tchernycheva, L. Nevou, L. Doyennette, R. Colombelli, E. Warde, F. Guillot and E. Monroy, "Nitride intersubband devices: prospects and recent developments," *physica status solidi (a)* **204**, 1987–1995 (2007)

[33] M. Beeler, E. Trichas and E. Monroy, "III-nitride semiconductors for intersubband optoelectronics: a review," *Semiconductor Science and Technology* **28**, 074022 (2013)

[34] N. Suzuki and N. Iizuka, "Electron Scattering Rates in AlGaN/GaN Quantum Wells for 1.55µm Inter-Subband Transition," *Japanese Journal of Applied Physics* **37**, L369 (1998)

[35] C. Gmachl, S. V. Frolov, H. M. Ng, S. N. G. Chu and A. Y. Cho, "Sub-picosecond electron scattering time for $\lambda = 1.55\mu$m intersubband transitions in GaN/AlGaN multiple quantum wells," *Electronics Letters* **37**, 378–380 (2001)

[36] J. D. Heber, C. Gmachl, H. M. Ng and A. Y. Cho, "Comparative study of ultrafast intersubband electron scattering times at 1.55 µm wavelength in GaN/AlGaN heterostructures," *Applied Physics Letters* **81**, 1237–1239 (2002)

[37] N. Iizuka, K. Kaneko and N. Suzuki, "Sub-picosecond modulation by intersubband transition in ridge waveguide with GaN/AlN quantum wells," *Electronics Letters* **40**, 962–963 (2004)

[38] J. Hamazaki, S. Matsui, H. Kunugita, K. Ema, H. Kanazawa, T. Tachibana, A. Kikuchi and K. Kishino, "Ultrafast intersubband relaxation and nonlinear susceptibility at 1.55 µm in GaN/AlN multiple-quantum wells," *Applied Physics Letters* **84**, 1102–1104 (2004)

[39] M. Tchernycheva, L. Nevou, L. Doyennette, F. H. Julien, E. Warde, F. Guillot, E. Monroy, E. Bellet-Amalric, T. Remmele and M. Albrecht, "Systematic experimental and theoretical investigation of intersubband absorption in GaN/AlN quantum wells," *Physical Review B* **73**, 125347 (2006)

[40] E. A. DeCuir, E. Fred, M. O. Manasreh, J. Schörmann, D. J. As and K. Lischka, "Near-infrared intersubband absorption in nonpolar GaN/AlN superlattices," *Applied Physics Letters* **91**, 041991 (2007)

[41] H. Machhadani, M. Tchernycheva, S. Sakr, L. Rigutti, R. Colombelli, E. Warde, C. Mietze, D. J. As and F. H. Julien, "Intersubband absorption of cubic GaN/Al(Ga)N quantum wells in the near-infrared to terahertz spectral range," *Physical Review B* **83**, 075313 (2011)

[42] J. Schörmann, S. Potthast, D. J. As and K. Lischka, "In situ growth regime characterization of cubic GaN using reflection high energy electron diffraction," *Applied Physics Letters* **90**, 041918 (2007)

[43] D.J. As, "Cubic group-III nitride-based nanostructures–basics and applications in optoelectronics," *Microelectronics Journal* **40**, 204–209 (2009)

[44] T. Wecker, "Herstellung und Charakterisierung von symmetrischen und asymmetrischen Doppel Quantum Wells," master thesis, University of Paderborn (2013)

[45] T. Wecker, F. Hörich, M. Feneberg, R. Goldhahn, D. Reuter and D. J. As, "Structural and optical properties of MBE-grown asymmetric cubic GaN/$Al_xGa_{1-x}N$ double quantum wells," *physica status solidi (b)* **252**, 873–878 (2015)

[46] F. Bernardini, V. Fiorentini and D. Vanderbilt, "Spontaneous polarization and piezoelectric constants of III-V nitrides," *Physical Review B* **56**, R10024–R10027 (1997)

[47] E. T. Yu, X. Z. Dang, P. M. Asbeck, S. S. Lau and G. J. Sullivan, "Spontaneous and piezoelectric polarization effects in III–V nitride heterostructures," *Journal of Vacuum Science & Technology B* **17**, 1742–1749 (1999)

[48] R. M. Kemper, P. Veit, C. Mietze, A. Dempewolf, T. Wecker, F. Bertram, J. Christen, J. K. N. Lindner and D. J. As, "STEM-CL investigations on the influence of stacking faults on the optical emission of cubic GaN epilayers and cubic GaN/AlN multi-quantum wells," *physica status solidi (c)* **12**, 469–472 (2015)

[49] P. Yeh, *Optical Waves in Layered Media*, 1st ed. (John Wiley & Sons, New York, 1988)

[50] P. Y. Yu and C. Cardona, *Fundamentals of Semiconductors: Physics and Material Properties*, 4th ed. (Springer, Berlin, 2010)

[51] C. G. Van de Walle and J. Neugebauer, "Small valence-band offsets at GaN/InGaN heterojunctions," *Applied Physics Letters* **70**, 2577–2579 (1997)

[52] S. Birner, S. Hackenbuchner, M. Sabathil, G. Zandler, J.A. Majewski, T. Andlauer, T. Zibold, R. Morschl, A. Trellakis and P. Vogl, "Modeling of semiconductor nanostructures with nextnano^3," *Acta Physica Polonica A* **110**, 111 (2006)

[53] H. Mathieu, P. Lefebvre and P. Christol, "Simple analytical method for calculating exciton binding energies in semiconductor quantum wells," *Physical Review B* **46**, 4092–4101 (1992)

[54] M. Feneberg, M. Röppischer, C. Cobet, N. Esser, J. Schörmann, T. Schupp, D. J. As, F. Hörich, J. Bläsing, A. Krost and R. Goldhahn, "Optical properties of cubic GaN from 1 to 20 eV," *Physical Review B* **85**, 155207 (2012)

[55] A. Helman, M. Tchernycheva, A. Lusson, E. Warde, F. H. Julien, Kh. Moumanis, G. Fishman, E. Monroy, B. Daudin, D. Le Si Dang, E. Bellet-Amalric and D. Jalabert, "Intersubband spectroscopy of doped and undoped GaN/AlN quantum wells grown by molecular-beam epitaxy," *Applied Physics Letters* **83**, 5196–5198 (2003)

[56] X. Y. Liu, P. Holmström, P. Jänes, L. Thylén and T. G. Andersson, "Intersubband absorption at 1.5–3.5 μm in GaN/AlN multiple quantum wells grown by molecular beam epitaxy on sapphire," *physica status solidi (b)* **244**, 2892–2905 (2007)

[57] C. B. Lim, M. Beeler, A. Ajay, J. Lähnemann, E. Bellet-Amalric, C. Bougerol and E. Monroy, "Intersubband transitions in nonpolar GaN/Al(Ga)N heterostructures in the short- and mid-wavelength infrared regions," *Journal of Applied Physics* **118**, (2015)

[58] C. B. Lim, M. Beeler, A. Ajay, J. Lähnemann, E. Bellet-Amalric, C. Bougerol, J. Schörmann, M. Eickhoff and E. Monroy, "Short-wavelength, mid- and far-infrared intersubband absorption in nonpolar GaN/Al(Ga)N heterostructures," *Japanese Journal of Applied Physics* **55**, 05FG05 (2016)

[59] J. B. Khurgin, "Inhomogeneous origin of the interface roughness broadening of intersubband transitions," *Applied Physics Letters* **93**, 091104 (2008)

[60] A. Y. Song, R. Bhat, P. Bouzi, C.-E. Zah and C. F. Gmachl, "Three-Dimensional Interface Roughness in Layered Semiconductor Structures and Its Effects on Intersubband Transitions," *arXiv [cond-mat.mtrl-sci]* **1507**, (2015)

[61] J. Shah, *Ultrafast Spectroscopy of Semiconductors and Semiconductor Nanostructures*, 2nd ed. (Springer, Berlin, 1999)

[62] C. F. Klingshirn, *Semiconductor Optics*, 3rd ed. (Springer, Berlin, 2006)

[63] Coherent Inc., *OPA 9800/9850*, last accessed 27 July 2016, URL: `https://www.coherent.com/Products/?934/OPA-9800-9850`

[64] Coherent Inc., *RegA*, last accessed 27 July 2016, URL: `https://www.coherent.com/Products/?940/RegA`

[65] L. Nevou, M. Tchernycheva, F. Julien, M. Raybaut, A. Godard, E. Rosencher, F. Guillot and E. Monroy, "Intersubband resonant enhancement of second-harmonic generation in GaN/AlN quantum wells," *Applied Physics Letters* **89**, 151101 (2006)

[66] R. W. Boyd, *Nonlinear Optics*, 1st ed. (Academic Press, San Diego, 1992)

[67] R. Rapaport, G. Chen, O. Mitrofanov, C. Gmachl, H. M. Ng and S. N. G. Chu, "Resonant optical nonlinearities from intersubband transitions in GaN/AlN quantum wells," *Applied Physics Letters* **83**, 263 (2003)

[68] J. Lee, M. Tymchenko, C. Argyropoulos, P.-Y. Chen, F. Lu, F. Demmerle, G. Boehm, Ma.-C. Amann, A. Alu and M. A. Belkin, "Giant nonlinear response from plasmonic metasurfaces coupled to intersubband transitions," *Nature* **511**, 65–69 (2014)

[69] O. Wolf, A. A. Allerman, X. Ma, J. R. Wendt, A. Y. Song, E. A. Shaner and I. Brener, "Enhanced optical nonlinearities in the near-infrared using III-nitride heterostructures coupled to metamaterials," *Applied Physics Letters* **107**, – (2015)

[70] M. Tazawa, P. Jin and S. Tanemura, "Optical constants of $V_{1-x}W_xO_2$ Films," *Applied Optics* **37**, 1858–1861 (1998)

[71] L. Bai, Q. Li, S. A. Corr, Y. Meng, C. Park, S. V. Sinogeikin, C. Ko, J. Wu and G. Shen, "Pressure-induced phase transitions and metallization in VO_2," *Physical Review B* **91**, 104110 (2015)

[72] A. Joushaghani, B. A. Kruger, S. Paradis, D. Alain, S. J. Aitchison and J. K. S. Poon, "Sub-volt broadband hybrid plasmonic-vanadium dioxide switches," *Applied Physics Letters* **102**, (2013)

[73] C. G. Granqvist, "Recent progress in thermochromics and electrochromics: A brief survey," *Thin Solid Films*, (2016)

[74] S. Wang, M. Liu, L. Kong, Y. Long, X. Jiang and A. Yu, "Recent progress in VO_2 smart coatings: Strategies to improve the thermochromic properties," *Progress in Materials Science* **81**, 1–54 (2016)

[75] R.T. Rajendra Kumar, B. Karunagaran, D. Mangalaraj, Sa. K. Narayandass, P. Manoravi, M. Joseph and Vishnu Gopal, "Pulsed laser deposited vanadium oxide thin films for uncooled infrared detectors," *Sensors and Actuators A: Physical* **107**, 62–67 (2003)

[76] E. Strelcov, Y. Lilach and A. Kolmakov, "Gas Sensor Based on Metal-Insulator Transition in VO_2 Nanowire Thermistor," *Nano Letters* **9**, 2322–2326 (2009)

[77] J. Cao, W. Fan, Q. Zhou, E. Sheu, A. Liu, C. Barrett and J. Wu, "Colossal thermal-mechanical actuation via phase transition in single-crystal VO_2 microcantilevers," *Journal of Applied Physics* **108**, 083538 (2010)

[78] H. Karl and S.C. Peyinghaus, "Tailoring of the thermomechanical performance of VO_2 nanowire bimorph actuators by ion implantation," *Nuclear Instruments and Methods in Physics Research Section B: Beam Interactions with Materials and Atoms* **365, Part A**, 75–78 (2015)

[79] M. Nakano, K. Shibuya, D. Okuyama, T. Hatano, S. Ono, M. Kawasaki, Y. Iwasa and Y. Tokura, "Collective bulk carrier delocalization driven by electrostatic surface charge accumulation," *Nature* **487**, 459–462 (2012)

[80] N. Shukla, A. V. Thathachary, A. Agrawal, H. Paik, A. Aziz, D. G. Schlom, S. K. Gupta, R. Engel-Herbert and S. Datta, "A steep-slope transistor based on abrupt electronic phase transition," *Nature Communications* **6**, (2015)

[81] T. Driscoll, H.-T. Kim, B.-G. Chae, B.-J. Kim, Y.-W. Lee, N. M. Jokerst, S. Palit, D. R. Smith, M. Di Ventra and D. N. Basov, "Memory Metamaterials," *Science* **325**, 1518–1521 (2009)

[82] T. Driscoll, H.-T. Kim, B.-G. Chae, M. Di Ventra and D. N. Basov, "Phase-transition driven memristive system," *Applied Physics Letters* **95**, 043503 (2009)

[83] H. Coy, R. Cabrera, N. Sepúlveda and F. E. Fernández, "Optoelectronic and all-optical multiple memory states in vanadium dioxide," *Journal of Applied Physics* **108**, 113115+ (2010)

[84] G. Seo, B. J. Kim, Y. W. Lee and H. T. Kim, "Photo-assisted bistable switching using Mott transition in two-terminal VO_2 device," *Applied Physics Letters* **100**, 011908+ (2012)

[85] Y. Zhou and S. Ramanathan, "Mott Memory and Neuromorphic Devices," *Proceedings of the IEEE* **103**, 1289–1310 (2015)

[86] D. Y. Lei, K. Appavoo, F. Ligmajer, Y. Sonnefraud, R. F. Haglund Jr. and S. A. Maier, "Optically-Triggered Nanoscale Memory Effect in a Hybrid Plasmonic-Phase Changing Nanostructure," *ACS Photonics* **2**, 1306–1313 (2015)

[87] J. Zimmer, A. Wixforth, H. Karl and H. J. Krenner, "Ion beam synthesis of nanothermochromic diffraction gratings with giant switching contrast at telecom wavelengths," *Applied Physics Letters* **100**, 231911+ (2012)

[88] A. X. Gray, J. Jeong, N. P. Aetukuri, P. Granitzka, Z. Chen, R. Kukreja, D. Higley, T. Chase, A. H. Reid, H. Ohldag, M. A. Marcus, A. Scholl, A. T. Young, A. Doran, C. A. Jenkins, P. Shafer, E. Arenholz, M. G. Samant, S. S. P. Parkin and H. A. Dürr, "Correlation-Driven Insulator-Metal Transition in Near-Ideal Vanadium Dioxide Films," *Physical Review Letters* **116**, 116403 (2016)

[89] J. B. Goodenough, "The two components of the crystallographic transition in VO_2," *Journal of Solid State Chemistry* **3**, 490 –500 (1971)

[90] V. Eyert, "The metal-insulator transitions of VO_2: A band theoretical approach," *Annalen der Physik* **11**, 650–704 (2002)

[91] P. Baum, D.-S. Yang and A. H. Zewail, "4D Visualization of Transitional Structures in Phase Transformations by Electron Diffraction," *Science* **318**, 788–792 (2007)

[92] D. Kucharczyk and T. Niklewski, "Accurate X-ray determination of the lattice parameters and the thermal expansion coefficients of VO_2 near the transition temperature," *Journal of Applied Crystallography* **12**, 370–373 (1979)

[93] V. Théry, A. Boulle, A. Crunteanu, J. C. Orlianges, A. Beaumont, R. Mayet, A. Mennai, F. Cosset, A. Bessaudou and M. Fabert, "Role of thermal strain in the metal-insulator and structural phase transition of epitaxial VO_2 films," *Physical Review B* **93**, 184106 (2016)

[94] S. Park, G. Lee, S. H. Song, C. H. Oh and P. S. Kim, "Resonant coupling of surface plasmons to radiation modes by use of dielectric gratings," *Optics Letters* **28**, 1870–1872 (2003)

[95] J. M. Atkin, S. Berweger, E. K. Chavez, M. B. Raschke, J. Cao, W. Fan and J. Wu, "Strain and temperature dependence of the insulating phases of VO_2 near the metal-insulator transition," *Physical Review B* **85**, 020101 (2012)

[96] M. Marezio, D. B. McWhan, J. P. Remeika and P. D. Dernier, "Structural Aspects of the Metal-Insulator Transitions in Cr-Doped VO_2," *Physical Review B* **5**, 2541–2551 (1972)

[97] V. R. Morrison, R. P. Chatelain, K. L. Tiwari, A. Hendaoui, A. Bruhács, M. Chaker and B. J. Siwick, "A photoinduced metal-like phase of monoclinic VO_2 revealed by ultrafast electron diffraction," *Science* **346**, 445–448 (2014)

[98] M. M. Qazilbash, M. Brehm, B.-G. Chae, P.-C. Ho, G. O. Andreev, Bong-Jun Kim, Sun Jin Yun, A. V. Balatsky, M. B. Maple, F. Keilmann, H.-T. Kim and D. N. Basov, "Mott Transition in VO_2 Revealed by Infrared Spectroscopy and Nano-Imaging," *Science* **318**, 1750–1753 (2007)

[99] R. M. Wentzcovitch, W. W. Schulz and P. B. Allen, “VO_2: Peierls or Mott-Hubbard? A view from band theory,” *Physical Review Letters* **72**, 3389–3392 (1994)

[100] A. Cavalleri, Th. Dekorsy, H. H. W. Chong, J. C. Kieffer and R. W. Schoenlein, “Evidence for a structurally-driven insulator-to-metal transition in VO_2: A view from the ultrafast timescale,” *Physical Review B* **70**, 161102(R) (2004)

[101] S. Biermann, A. Poteryaev, A. I. Lichtenstein and A. Georges, “Dynamical Singlets and Correlation-Assisted Peierls Transition in VO_2,” *Physical Review Letters* **94**, 026404 (2005)

[102] A. Pashkin, C. Kübler, H. Ehrke, R. Lopez, A. Halabica, R. F. Haglund, R. Huber and A. Leitenstorfer, “Ultrafast insulator-metal phase transition in VO_2 studied by multiterahertz spectroscopy,” *Physical Review B* **83**, 195120+ (2011)

[103] A. Zylbersztejn and N. F. Mott, “Metal-insulator transition in vanadium dioxide,” *Physical Review B* **11**, 4383–4395 (1975)

[104] D. Paquet and P. Leroux-Hugon, “Electron correlations and electron-lattice interactions in the metal-insulator, ferroelastic transition in VO_2: A thermodynamical study,” *Physical Review B* **22**, 5284–5301 (1980)

[105] T. M. Rice, H. Launois and J. P. Pouget, “Comment on VO_2: Peierls or Mott-Hubbard? A View from Band Theory",” *Physical Review Letters* **73**, 3042–3042 (1994)

[106] D. Wegkamp, M. Herzog, L. Xian, M. Gatti, P. Cudazzo, C. L. McGahan, R. E. Marvel, R. F. Haglund, A. Rubio, M. Wolf and J. Stähler, “Instantaneous Band Gap Collapse in Photoexcited Monoclinic VO_2 due to Photocarrier Doping,” *Physical Review Letters* **113**, 216401 (2014)

[107] S. Wall, L. Foglia, D. Wegkamp, K. Appavoo, J. Nag, R. F. Haglund, J. Stähler and M. Wolf, “Tracking the evolution of electronic and structural properties of VO_2 during the ultrafast photoinduced insulator-metal transition,” *Physical Review B* **87**, 115126 (2013)

[108] M. W. Haverkort, Z. Hu, A. Tanaka, W. Reichelt, S. V. Streltsov, M. A. Korotin, V. I. Anisimov, H. H. Hsieh, H.-J. Lin, C. T. Chen, D. I. Khomskii and L. H. Tjeng, “Orbital-Assisted Metal-Insulator Transition in VO_2,” *Physical Review Letters* **95**, 196404 (2005)

[109] M. Rini, A. Cavalleri, R. W. Schoenlein, R. López, L. C. Feldman, R. F. Haglund Jr., L. A. Boatner and T. E. Haynes, “Photoinduced phase transition in VO_2 nanocrystals: ultrafast control of surface-plasmon resonance,” *Optics Letters* **30**, 558–560 (2005)

[110] C. Kübler, H. Ehrke, R. Huber, R. Lopez, A. Halabica, R. F. Haglund and A. Leitenstorfer, “Coherent Structural Dynamics and Electronic Correlations during an Ultrafast Insulator-to-Metal Phase Transition in VO_2,” *Physical Review Letters* **99**, 116401 (2007)

[111] B. T. O'Callahan, A. C. Jones, J. Hyung Park, D. H. Cobden, J. M. Atkin and M. B. Raschke, "Inhomogeneity of the ultrafast insulator-to-metal transition dynamics of VO_2," *Nature Communications* **6**, (2015)

[112] R. Lopez, L. A. Boatner, T. E. Haynes, L. C. Feldman and Richard F. Haglund Jr., "Synthesis and characterization of size-controlled vanadium dioxide nanocrystals in a fused silica matrix," *Journal of Applied Physics* **92**, 4031–4036 (2002)

[113] D. Stroud, "The effective medium approximations: Some recent developments," *Superlattices and Microstructures* **23**, 567–573 (1998)

[114] H. Kakiuchida, P. Jin, S. Nakao and M. Tazawa, "Optical Properties of Vanadium Dioxide Film during Semiconductive–Metallic Phase Transition," *Japanese Journal of Applied Physics* **46**, L113 (2007)

[115] R. Lopez, L. Feldman and R. Haglund, "Size-Dependent Optical Properties of VO_2 Nanoparticle Arrays," *Physical Review Letters* **93**, 177403+ (2004)

[116] A. Cavalleri, M. Rini and R. W. Schoenlein, "Ultra-Broadband Femtosecond Measurements of the Photo-Induced Phase Transition in VO_2: From the Mid-IR to the Hard X-rays," *Journal of the Physical Society of Japan* **75**, 011004 (2006)

[117] W. R. Roach, "Holographic Storage in VO_2," *Applied Physics Letters* **19**, 453–455 (1971)

[118] A. W. Smith, "Optical storage in VO_2 films," *Applied Physics Letters* **23**, 437–438 (1973)

[119] K. Appavoo, Dang Y. Lei, Y. Sonnefraud, B. Wang, S. T. Pantelides, S. A. Maier and R. F. Haglund Jr., "Role of Defects in the Phase Transition of VO_2 Nanoparticles Probed by Plasmon Resonance Spectroscopy," *Nano Letters* **12**, 780–786 (2012)

[120] E. U. Donev, R. Lopez, L. C. Feldman and R. F. Haglund, "Confocal Raman Microscopy across the Metal–Insulator Transition of Single Vanadium Dioxide Nanoparticles," *Nano Letters* **9**, 702–706 (2009)

[121] H. Zhang, Z. Wu, X. Wu, W. Yang and Y.Jiang, "Transversal grain size effect on the phase-transition hysteresis width of vanadium dioxide films comprising spheroidal nanoparticles," *Vacuum* **104**, 47 –50 (2014)

[122] J. Y. Suh, R. Lopez, L. C. Feldman and R. F. Haglund, "Semiconductor to metal phase transition in the nucleation and growth of VO_2 nanoparticles and thin films," *Journal of Applied Physics* **96**, 1209–1213 (2004)

[123] J. Wei, Z. Wang, W. Chen and D. H. Cobden, "New aspects of the metal-insulator transition in single-domain vanadium dioxide nanobeams," *Nature Nanotechnology* **4**, 420–424 (2009)

[124] J. Cao, Y. Gu, W. Fan, L. Q. Chen, D. F. Ogletree, K. Chen, N. Tamura, M. Kunz, C. Barrett, J. Seidel and J. Wu, "Extended Mapping and Exploration of the Vanadium Dioxide Stress-Temperature Phase Diagram," *Nano Letters* **10**, 2667–2673 (2010)

[125] Y. Muraoka, Y. Ueda and Z. Hiroi, “Large modification of the metal–insulator transition temperature in strained VO_2 films grown on TiO_2 substrates,” *Journal of Physics and Chemistry of Solids* **63**, 965–967 (2002)

[126] J. Sakai, M. Zaghrioui, M. Matsushima, H. Funakubo and K. Okimura, “Impact of thermal expansion of substrates on phase transition temperature of VO_2 films,” *Journal of Applied Physics* **116**, 123510 (2014)

[127] F. C. Case, “Modifications in the phase transition properties of predeposited VO_2 films,” *Journal of Vacuum Science & Technology A* **2**, 1509–1512 (1984)

[128] H. Karl, J. Dreher and B. Stritzker, “Semiconductor-Metal Phase Transition in Doped Ion Beam Synthesized VO_2 Nanoclusters,” *MRS Proceedings*, 1174–V06–35 (7 pages) (2009)

[129] A. Leone, A. M. Trione and F. Junga, “Alteration in electrical and infrared switching properties of vanadium oxides due to proton irradiation,” *IEEE Transactions on Nuclear Science* **37**, 1739–1743 (1990)

[130] J. Rensberg, S. Zhang, Y. Zhou, A. S. McLeod, C. Schwarz, M. Goldflam, M. Liu, J. Kerbusch, R. Nawrodt, S. Ramanathan, D. N. Basov, F. Capasso, C. Ronning and M. A. Kats, “Active Optical Metasurfaces Based on Defect-Engineered Phase-Transition Materials,” *Nano Letters* **16**, 1050–1055 (2016)

[131] K. D. Ufert and E. I. Terukov, “On the Problem of the Phase Transition in Disordered VO_2 Thin Films,” *physica status solidi (a)* **40**, K157–K159 (1977)

[132] A.-K. Jambreck, “Herstellung und Charakterisierung vergrabener VO_2-Nanocluster mittels Ionenimplantation,” Diplomathesis, Institut für Physik der Universität Augsburg (2008)

[133] S. Raoux, “Phase Change Materials,” *Annual Review of Materials Research* **39**, 25–48 (2009)

[134] T. V. Son, C. O. F. Ba, R. Vallée and A. Haché, “Nanometer-thick flat lens with adjustable focus,” *Applied Physics Letters* **105**, 231120 (2014)

[135] X.-Y. Peng, B. Wang, J. Teng, J. B. Kana Kana and X. Zhang, “Active near infrared linear polarizer based on VO_2 phase transition,” *Journal of Applied Physics* **114**, (2013)

[136] D. Wang, L. Zhang, Y. Gu, M. Q. Mehmood, Y. Gong, A. Srivastava, L. Jian, T. Venkatesan, C.-W. Qiu and M. Hong, “Switchable Ultrathin Quarter-wave Plate in Terahertz Using Active Phase-change Metasurface,” *Scientific Reports* **5**, 15020 (2015)

[137] R. M. Briggs, I. M. Pryce and H. A. Atwater, “Compact silicon photonic waveguide modulator based on the vanadium dioxide metal-insulator phase transition,” *Optics Express* **18**, 11192–11201 (2010)

[138] S. B. Choi, J. S. Kyoung, H. S. Kim, H. R. Park, D. J. Park, Bong-Jun Kim, Y. H. Ahn, F. Rotermund, H.-T. Kim, K. J. Ahn and D. S. Kim, “Nanopattern enabled terahertz all-optical switching on vanadium dioxide thin film,” *Applied Physics Letters* **98**, 071105+ (2011)

[139] J. D. Ryckman, K. A. Hallman, R. E. Marvel, R. F. Haglund Jr. and S. M. Weiss, “Ultra-compact silicon photonic devices reconfigured by an optically induced semiconductor-to-metal transition,” *Optics Express* **21**, 10753–10763 (2013)

[140] K. Appavoo and R. F. Haglund Jr., “Polarization selective phase-change nanomodulator,” *Scientific Reports* **4**, 6771 (2014)

[141] J.C. Rakotoniaina, R. Mokrani-Tamellin, J.R. Gavarri, G. Vacquier, A. Casalot and G. Calvarin, “The Thermochromic Vanadium Dioxide,” *Journal of Solid State Chemistry* **103**, 81–94 (1993)

[142] Lawrence Berkeley National Laboratory Center for X-Ray Optics, *X-ray data booklet*, 2009, URL: `http://xdb.lbl.gov/xdb-new.pdf`

[143] The Center for X-ray optics, Lawrence Berkeley National Laboratory, *Fresnel zone plate theory, generation, tolerancing, fabrication, and applications.* last accessed 5 May 2016, URL: `http://zoneplate.lbl.gov/`

[144] D. R. Reid, “A full electromagnetic analysis of fresnel zone plate antennas and the application to a free-space focused-beammeasurement system,” Dissertation, Georgia Institute of Technology, 2008, URL: `http://hdl.handle.net/1853/26620`

[145] W. L. Barnes, A. Dereux and T. W. Ebbesen, “Surface plasmon subwavelength optics,” *Nature* **424**, 824–830 (2003)

[146] A. G. Brolo, “Plasmonics for future biosensors,” *Nature Photonics* **6**, 709–713 (2012)

[147] H. H. Nguyen, J. Park, S. Kang and M. Kim, “Surface Plasmon Resonance: A Versatile Technique for Biosensor Applications,” *Sensors* **15**, 10481 (2015)

[148] K. Kneipp, Y. Wang, H. Kneipp, L. T. Perelman, I. Itzkan, Ramachandra R. D. and M. S. Feld, “Single Molecule Detection Using Surface-Enhanced Raman Scattering (SERS),” *Physical Review Letters* **78**, 1667–1670 (1997)

[149] K. Kneipp, “Surface-enhanced Raman scattering,” *Physics Today*, page 40 (November 2007)

[150] J. Butet, P.-F. Brevet and O. J. F. Martin, “Optical Second Harmonic Generation in Plasmonic Nanostructures: From Fundamental Principles to Advanced Applications,” *ACS Nano* **9**, 10545–10562 (2015)

[151] M. Sivis, M. Duwe, B. Abel and C. Ropers, “Extreme-ultraviolet light generation in plasmonic nanostructures,” *Nature Physics* **9**, 304–309 (2013)

[152] M. Kauranen and A. V. Zayats, “Nonlinear Plasmonics,” *Nature Photonics* **6**, 737–748 (2012)

[153] H. A. Atwater and A. Polman, “Plasmonics for improved photovoltaic devices,” *Nature Materials* **9**, 205–2013 (2010)

[154] Q. Zhang, E. Uchaker, S. L. Candelaria and G. Cao, “Nanomaterials for energy conversion and storage,” *Chemical Society Reviews* **42**, 3127–3171 (2013)

[155] E. Stratakis and E. Kymakis, "Nanoparticle-based plasmonic organic photovoltaic devices," *Materials Today* **16**, 133–146 (2013)

[156] E. Ozbay, "Plasmonics: Merging Photonics and Electronics at Nanoscale Dimensions," *Science* **311**, 189–193 (2006)

[157] Y. Fang and M. Sun, "Nanoplasmonic waveguides: towards applications in integrated nanophotonic circuits," *Light: Science and Applications* **4**, (2015)

[158] J. D. Cox and F. Javier García de Abajo, "Electrically tunable nonlinear plasmonics in graphene nanoislands," *Nature Communications* **5**, (2014)

[159] C. Ruppert, F. Föster, A. Zrenner, J. B. Kinzel, A. Wixforth, Hu. J. Krenner and M. Betz, "Radio Frequency Electromechanical Control over a Surface Plasmon Polariton Coupler," *ACS Photonics* **1**, 91–95 (2014)

[160] J. Schiefele, J. Pedrós, F. Sols, F. Calle and F. Guinea, "Coupling Light into Graphene Plasmons through Surface Acoustic Waves," *Physical Review Letters* **111**, 237405 (2013)

[161] N. Rotenberg, M. Betz and H. M. van Driel, "Ultrafast control of grating-assisted light coupling to surface plasmons," *Optics Letters* **33**, 2137–2139 (2008)

[162] K. F. MacDonald, Z. L. Samson, M. I. Stockman and N. I. Zheludev, "Ultrafast active plasmonics," *Nature Photonics* **3**, 55–58 (2009)

[163] J. Y. Suh, E. U. Donev, R. Lopez, L. C. Feldman and Richard F. Haglund Jr., "Modulated optical transmission of subwavelength hole arrays in metal-VO_2 films," *Applied Physics Letters* **88**, 133115+ (2006)

[164] L. A. Sweatlock and K. Diest, "Vanadium dioxide based plasmonic modulators," *Optics Express* **20**, 8700–8709 (2012)

[165] Y. Sharma, V. A. Tiruveedhula, J. F. Muth and A. Dhawan, "VO_2 based waveguide-mode plasmonic nano-gratings for optical switching," *Optics Express* **23**, 5822–5849 (2015)

[166] J. Jeong, A. Joushaghani, S. Paradis, D. Alain and J. K. S. Poon, "Electrically controllable extraordinary optical transmission in gold gratings on vanadium dioxide," *Optics Letters* **40**, 4408–4411 (2015)

[167] P. Markov, K. Appavoo, R. F. Haglund Jr. and S. M. Weiss, "Hybrid Si-VO_2-Au optical modulator based on near-field plasmonic coupling," *Optics Express* **23**, 6878–6887 (2015)

[168] B. A. Kruger, A. Joushaghani and J. K. S. Poon, "Design of electrically driven hybrid vanadium dioxide (VO_2) plasmonic switches," *Optics Express* **20**, 23598–23609 (2012)

[169] M. Beebe, L. Wang, S. E. Madaras, J. M. Klopf, Z. Li, D. Brantley, M. Heimburger, R. A. Wincheski, S. Kittiwatanakul, J. Lu, S. A. Wolf and R. A. Lukaszew, "Surface plasmon resonance modulation in nanopatterned Au gratings by the insulator-metal transition in vanadium dioxide films," *Optics Express* **23**, 13222–13229 (2015)

[170] M. Yi, C. Lu, Y. Gong, Z. Qi and Y. Cui, "Dual-functional sensor based on switchable plasmonic structure of VO_2 nano-crystal films and Ag nanoparticles," *Optics Express* **22**, 29627–29635 (2014)

[171] S. K. Earl, T. D. James, T. J. Davis, J. C. McCallum, R. E. Marvel, R. F. Haglund and A. Roberts, "Tunable optical antennas enabled by the phase transition in vanadium dioxide," *Optics Express* **21**, 27503–27508 (2013)

[172] M. A. Kats, R. Blanchard, P. Genevet, Z. Yang, M. M. Qazilbash, D. N. Basov, S. Ramanathan and F. Capasso, "Thermal tuning of mid-infrared plasmonic antenna arrays using a phase change material," *Optics Letters* **38**, 368–370 (2013)

[173] J. He, Z. Xie, W. Sun, X. Wang, Y. Ji, S. Wang, Y. Lin and Y. Zhang, "Terahertz Tunable Metasurface Lens Based on Vanadium Dioxide Phase Transition," *Plasmonics*, 1–6 (2016)

[174] Z. L. Sámson, K. F. MacDonald, F. De Angelis, B. Gholipour, K. Knight, C. C. Huang, E. Di Fabrizio, D. W. Hewak and N. I. Zheludev, "Metamaterial electro-optic switch of nanoscale thickness," *Applied Physics Letters* **96**, (2010)

[175] A.-K. U. Michel, D. N. Chigrin, T. W. W. Maß, K. Schönauer, M. Salinga, M. Wuttig and T. Taubner, "Using Low-Loss Phase-Change Materials for Mid-Infrared Antenna Resonance Tuning," *Nano Letters* **13**, 3470–3475 (2013)

[176] A.-K. U. Michel, P. Zalden, D. N. Chigrin, M. Wuttig, A. M. Lindenberg and T. Taubner, "Reversible Optical Switching of Infrared Antenna Resonances with Ultrathin Phase-Change Layers Using Femtosecond Laser Pulses," *ACS Photonics* **1**, 833–839 (2014)

[177] T. Hira, T. Homma, T. Uchiyama, K. Kuwamura and T. Saiki, "Switching of localized surface plasmon resonance of gold nanoparticles on a GeSbTe film mediated by nanoscale phase change and modification of surface morphology," *Applied Physics Letters* **103**, (2013)

[178] T. Cao, C. Wei, R. E. Simpson, L. Zhang and M. J. Cryan, "Fast Tuning of Double Fano Resonance Using A Phase-Change Metamaterial Under Low Power Intensity," *Scientific Reports* **4**, 4463 (2014)

[179] M. Rudé, R. E. Simpson, R. Quidant, V. Pruneri and J. Renger, "Active Control of Surface Plasmon Waveguides with a Phase Change Material," *ACS Photonics* **2**, 669–674 (2015)

[180] H. Raether, *Surface Plasmons on Smooth and Rough Surfaces and on Gratings*, 1st ed. (Springer, Berlin, 1988)

[181] S. A. Maier, *Plasmonics: Fundamentals and Applications*, 1st ed. (Springer US, Boston, 2007)

[182] P. E. Ciddor, "Refractive index of air: new equations for the visible and near infrared," *Applied Optics* **35**, 1566–1573 (1996)

[183] P. B. Johnson and R. W. Christy, "Optical Constants of the Noble Metals," *Physical Review B* **6**, 4370–4379 (1972)

[184] Toptica Photonics AG, *FemtoFiber pro IR*, last accessed 27 July 2016, URL: `http://www.toptica.com/products/ultrafast_fiber_lasers/femtofiber_pro/femtofiber_pro_ir.html`

[185] C. Ruppert and M. Betz, "Generation of 30 femtosecond, 900-970 nm pulses from a Ti:sapphire laser far off the gain peak," *Optics Express* **16**, 5572–5576 (2008)

[186] Y.-Y. Teng and E. A. Stern, "Plasma Radiation from Metal Grating Surfaces," *Physical Review Letters* **19**, 511–514 (1967)

[187] R. H. Ritchie, E. T. Arakawa, J. J. Cowan and R. N. Hamm, "Surface-Plasmon Resonance Effect in Grating Diffraction," *Physical Review Letters* **21**, 1530–1533 (1968)

[188] R.H. Ritchie, "Surface plasmons in solids," *Surface Science* **34**, 1–19 (1973)

[189] N. Rotenberg, J. N. Caspers and H. M. van Driel, "Tunable ultrafast control of plasmonic coupling to gold films," *Physical Review B* **80**, 245420 (2009)

[190] E. Kretschmann and H. Raether, "Radiative Decay of Non Radiative Surface Plasmons Excited by Light," *Zeitschrift für Naturforschung* **23 a**, 2135–2136 (1968)

[191] I. H. Malitson, "Interspecimen Comparison of the Refractive Index of Fused Silica," *Journal of the Optical Society of America* **55**, 1205–1209 (1965)

[192] U. Fano, "Effects of Configuration Interaction on Intensities and Phase Shifts," *Physical Review* **124**, 1866–1878 (1961)

[193] B. Luk'yanchuk, N. I. Zheludev, S. A. Maier, N.J. Halas, P. Nordlander, H. Giessen and C. T. Chong, "The Fano resonance in plasmonic nanostructures and metamaterials," *Nature Materials* **9**, 707–715 (2010)

[194] A. Lovera, B. Gallinet, P. Nordlander and O. J. F. Martin, "Mechanisms of Fano Resonances in Coupled Plasmonic Systems," *ACS Nano* **7**, 4527–4536 (2013)

[195] R. Nicolas, G. Lévêque, Jo. Marae-Djouda, G. Montay, J. Madi Y.and Plain, Z. Herro, M. Kazan, P.-M. Adam and T. Maurer, "Plasmonic mode interferences and Fano resonances in Metal-Insulator-Metal nanostructured interface," *Scientific Reports* **5**, 14419 (2015)

[196] A. Otto, "Excitation of nonradiative surface plasma waves in silver by the method of frustrated total reflection," *Zeitschrift für Physik* **216**, 398–410 (1968)

[197] E. Kretschmann, "Die Bestimmung optischer Konstanten von Metallen durch Anregung von Oberflächenplasmaschwingungen," *Zeitschrift für Physik* **241**, 313–324 (1971)

[198] A. S. Barker, "Direct Optical Coupling to Surface Excitations," *Physical Review Letters* **28**, 892–895 (1972)

[199] R. B. M. Schasfoort and A. J. Tudos, *Handbook of Surface Plasmon Resonance* (The Royal Society of Chemistry, 2008)

[200] H. S. Lee, C. Awada, S. Boutami, F. Charra, L. Douillard and R. Espiau de Lamaestre, "Loss mechanisms of surface plasmon polaritons propagating on a smooth polycrystalline Cu surface," *Optics Express* **20**, 8974–8981 (2012)

[201] J. T. van Wijngaarden, E. Verhagen, A. Polman, C. E. Ross, H. J. Lezec and H. A. Atwater, "Direct imaging of propagation and damping of near-resonance surface plasmon polaritons using cathodoluminescence spectroscopy," *Applied Physics Letters* **88**, 221111 (2006)

[202] H.-T. Zhang, L. Guo, G. Stone, L. Zhang, Y.-X. Zheng, E. Freeman, D. W. Keefer, S. Chaudhuri, H. Paik, J. A. Moyer, M. Barth, D. G. Schlom, J. V. Badding, S. Datta, V. Gopalan and R. Engel-Herbert, "Imprinting of Local Metallic States into VO_2 with Ultraviolet Light," *Advanced Functional Materials*, Early View Online (2016)

Publications and Conference Contributions

List of Publications

T. Jostmeier, M. Mangold, J. Zimmer, H. Karl, H.J. Krenner, C. Ruppert and M. Betz, “Thermochromic modulation of surface plasmon polaritons in vanadium dioxide nanocomposites”, *Optics Express* **24**, 265054 (2016)

E. Sternemann, **T. Jostmeier**, C. Ruppert, S. Thunich, H.T. Duc, R. Podzimski, T. Meier and M. Betz, “Quantum interference control of electrical currents in GaAs microstructures: physics and spectroscopic applications”, *Applied Physics B* **122**:44 (2016)

T. Jostmeier, T. Wecker, D. Reuter, D.J. As and M. Betz, “Ultrafast carrier dynamics and resonant inter-miniband nonlinearity of a cubic GaN/AlN superlattice”, *Applied Physics Letters* **107**, 211101 (2015)

T. Jostmeier, J. Zimmer, H. Karl, H.J. Krenner and M. Betz, “Optically imprinted reconfigurable photonic elements in a VO_2 nanocomposite”, *Applied Physics Letters* **105**, 071107 (2014)

T. Jostmeier, J. Zimmer, H. Karl, H.J. Krenner and M. Betz, “Optical Preparation of Stable Supercooled VO_2 Nanocrystals: A Route Towards Reconfigurable Photonic Devices for Telecom Wavelengths”, *CLEO: 2014 (Conference on Lasers and Electro-Optics)*, Optical Society of America, paper **STu2H.1** (2014)

E. Sternemann, **T. Jostmeier**, C. Ruppert, H.T. Duc, T. Meier and M. Betz, “Femtosecond quantum interference control of electrical currents in GaAs: Signatures beyond the perturbative $\chi^{(3)}$ limit”, *Physical Review B* **88**, 165204 (2013)

Conference Contributions

March 2016, Poster presentation, “Thermochromic nano-plasmonic devices based on a VO_2 nanocomposite”, PLMCN17 (17th International Conference on Physics of Light-Matter Coupling in Nanostructures), Nara, Japan

November 2015, Member of the Organizing Committee and regular talk, “Inter-miniband absorption and ultrafast carrier dynamics of a cubic GaN/AlN superlattice”, 3rd Internal Workshop of the SFB/TRR142, Dortmund, Germany

May 2015, Poster presentations, “Cubic GaN/AlN heterostructures: Nonequilibrium carrier dynamics” and “Cubic GaN/AlN heterostructures: Structural characterisation and ultrafast acoustics”, 2nd Internal Workshop of the SFB/TRR142, Bad Sassendorf, Germany

July 2014, Regular talk, “Optical Preparation of Stable Supercooled VO_2 Nanocrystals: A Route Towards Reconfigurable Photonic Devices for Telecom Wavelengths”, CLEO: 2014 (Conference on Lasers and Electro-Optics), San Jose, USA

May 2014, Regular talk, “Optically induced switching and bistability in VO_2 nanocrystals”, DPG Spring Meeting of the Condensed Matter Section, Dresden, Germany

December 2013, Regular talk, “Optically induced switching and bistability of the insulator-metal phase transition in vanadium dioxide nanoclusters”, GRK1464 & Guests: Convention, Paderborn, Germany

October 2012, Regular talk, “Quantum Interference Control of Electrical Eurrents in GaAs: Signatures Beyond the Pertubative $\chi^{(3)}$-Limit”, 2nd Student Seminar of the DFG Priority Programm SPP142 Ultrafast Nanooptics, Lauterbad, Germany

Acknowledgements

Finally, I would like to thank the people who contributed to this thesis, supported me or made the time at this department pleasant and productive. Special thanks go to ...

... my advisor Prof. Dr. Markus Betz for the introduction to photonics & laser optics, his repertoire of numerous experimental tricks, his willingness to discuss physics and experimental issues and quick lectures during coffee breaks.

... Prof. Dr. Donat As and Tobias Wecker from the University of Paderborn for the fruitful collaboration during the study of the GaN/AlN-based heterostructures.

... Prof. Dr. Hubert J. Krenner, Prof. Dr. Helmut Karl and their group members from the University of Augsburg for the fruitful collaboration during the VO_2-related studies.

... Dr. Claudia Ruppert for helping me with the transfer-matrix simulations and for numerous discussions and handy tips, especially in the early years of my studies.

... all current and former members of E2b for an enjoyable atmosphere in the labs and offices, helpful physical discussions and fun outside-of-work group activities.

... Prof. Dr. Manfred Bayer for the opportunity to work at E2, and all members of E2 for a pleasant overall atmosphere.

... Gisela Pike and Dirk Schemionek for the high-quality and quick sample preparation.

... Lars Wieschollek, Klaus Wiegers, Thomas Stöhr and the members of the mechanical and electrical workshop for technical assistance.

... Michaela Wäscher and Nina Collette for patient and effective administrative support.

... Thomas Czerniuk for proofreading, and Dr. Elmar Sternemann for proofreading, a fun time during the final year of my masters degree and for being an excellent office mate.

... Jan Lohrenz, Thomas Czerniuk and Johannes Hackmann for the years we spend together in Dortmund during our studies, work and, most importantly, in our free time.

... my whole family for entertaining traditions, distractions and all kinds of assistance.

... Simone for her unconditional, heartening support.